Moving Target Indication for Multi-channel Airborne Radar Systems

Moving Target Indication for Multi-channel Airborne Radar Systems

Proefschrift

ter verkrijging van de graad van doctor
aan de Technische Universiteit Delft,
op gezag van de Rector Magnificus prof.ir. K.Ch.A.M. Luyben,
voorzitter van het College voor Promoties,
in het openbaar te verdedigen
op maandag 11 oktober 2010 om 12:30 uur
door Ludvík LIDICKÝ
elektrotechnisch ingenieur
geboren te Sokolov, Tsjechoslowakije.

Dit proefschrift is goedgekeurd door de promotoren:

Prof.ir. P. Hoogeboom
Prof.dr.ir. L.P. Ligthart

Samenstelling promotiecommissie:

Rector Magnificus,	voorzitter
Prof.ir. P. Hoogeboom,	Technische Universiteit Delft, promotor
Prof.dr.ir. L.P. Ligthart,	Technische Universiteit Delft, promotor
Prof.dr.ir. R.F. Hanssen,	Technische Universiteit Delft
Prof.dr. F. Le Chevalier,	Technische Universiteit Delft
Prof.Dr.-Ing. J. Ender,	Fraunhofer-Institut für Hochfrequenzphysik und Radartechnik FHR
Dr. A. Meta,	Metasensing
Dr.ir. J.J.M. de Wit,	TNO Defensie en Veiligheid

This research was supported by TNO Defence, Security and Safety.

Set in Hoefler Text by the author using XeLaTeX.

ISBN/EAN: 978-94-6113-014-3

Contents

Summary

Moving target indication (MTI) using radar is of great interest in civil and military applications. Its uses include airborne or space-borne surveillance of ground moving vehicles (cars, trains) or ships at sea, for instance. Airborne (space-borne) radar offers several advantages when compared to optical imaging, they include: day-and-night, all-weather capability and a possibly greater potential in resolving moving objects in a stationary scene. Recent systems utilise single-channel radars to produce fine-resolution images of stationary scenes by means of the synthetic aperture radar (SAR) and multi-channel arrays to achieve the best possible separation of moving objects from the stationary ones. This technology is currently employed in airborne military and experimental systems such as SOSTAR-X (European), PAMIR (Germany) and MCARM (USA). Also, the Canadian satellite RADARSAT-2 has a special multi-channel mode for radar MTI.

The concept of multi-channel MTI alleviates the necessity for high-contrast in the detection of moving objects in the scene and it is very sensitive to low velocities. Its implementation is called *space-time adaptive processing* or STAP. STAP is capable of detection of moving targets but it offers limited options for their imaging.

This thesis is a result of research jointly performed at the International Research Centre for Telecommunications and Radar associated with Delft University of Technology (IRCTR) and the TNO Defense, Security and Safety in the Hague, the Netherlands. The goal was to develop models suitable for general scenarios and to study optimal, yet fast and efficient algorithms capable of processing data created by these models. Theoretical results were to be verified experimentally. The research was to answer several questions:

Are there any benefits in combining SAR and STAP? If the task at hand is to perform imaging of moving targets with resolution equal to the resolution of images of stationary targets using SAR, a signal model fully general for the given geometry is required. Inversions of such a model have been found, albeit for some cases only. The approach is mainly suitable for generation of synthetic datasets for numerical evaluation of SAR/MTI processing techniques, but also for the study of new, potentially interesting applications such as MTI with ultra-wideband ground penetrating radar.

Is it possible to find a fast yet optimal or near-optimal MTI algorithm? It is suggested that if the channel calibration is done properly, averaging of signals from multiple channels can be used to extract moving targets. Being a relatively inexpensive operation, averaging will yield considerable savings in the computational power necessary to perform MTI. Although the real-time implementation of such an algorithm by means of a high-pass filter was already proposed by other authors, it was not validated using real data.
How would such an algorithm perform when applied to measured data? A known STAP algorithm and averaging were applied to two airborne datasets: one based on the MCARM data, the other based on the SOSTAR-X data. It was concluded that a simple channel mismatch model could be assumed. Contrary to the MCARM data, the SOSTAR-X data contained severe channel mismatch. Nevertheless, at least one MTI algorithm worked satisfactorily in both cases.
How can we use STAP in a new fashion? A way to detect victims buried in debris during natural disasters or terrorist attacks is proposed. Several experiments with ultra-wideband ground penetrating radar were carried out at the IRCTR. The results were in good agreement with predictions.

The main results obtained in this thesis can be summarised as follows:
Extended models for multi-channel SAR (MSAR) MTI. The thesis complements the TNO's expertise in single-channel SAR MTI algorithms. It builds on ideas put forth in open literature and provides more general closed-form expressions for the MSAR transfer function.
Heuristic investigations into error sources in real data. A simple model for airborne MTI where so-called internal clutter motion and flight path deviations are neglected, and the mismatch between channels is constant with time is tested on real data from MCARM and SOSTAR-X projects. Although deterministic the STAP techniques used in this thesis have already been applied to the MCARM data, no easy comparison to other published attempts was found. A detailed comparison is provided here. This heuristic validation provided insights into interpretation of SOSTAR-X data.
Novel application of STAP to detection of buried victims. A new idea to use STAP for detection of moving objects buried underground or in debris is described. The idea is based on the possibility of detecting a slight motion of the victims produced by breathing. MSAR MTI processing provides fine spatial resolution due to the synthetic aperture concept and slow motion detection capability due to STAP. An alternative side-looking antenna configuration instead of the more traditional down-looking configuration is used. First results with measured data are presented.

Samenvatting

Detectie van bewegende doelen (MTI) met behulp van radar is van groot belang voor civiele en militaire toepassingen. Een belangrijke toepassing is het monitoren van auto's, treinen of schepen vanaf vliegtuigen of satellieten. Radar heeft belangrijke voordelen ten opzichte van optische sensoren: radar is dag en nacht inzetbaar, radar is ook in slecht weer bruikbaar en radar is beter in het detecteren van bewegende doelen tegen een statische achtergrond. Huidige radarsystemen maken gebruik van enkel-kanaals synthetische apertuur radar (SAR) technieken om hoge-resolutie beelden van de achtergrond te verkrijgen en antennesystemen met meerdere ontvangstkanalen om bewegende doelen te kunnen detecteren. Deze technieken worden toegepast in militaire en experimentele radarsystemen zoals het Europese SOSTAR-X systeem, het Duitse PAMIR systeem, het Amerikaanse MCARM systeem en het Canadese RADARSAT-2 satelliet radar systeem.
Meer-kanaals MTI technieken maken het mogelijk om langzaam bewegende doelen te detecteren tegen een statische achtergrond. Deze technieken worden meestal aangeduid als *space-time adaptive processing* technieken of kortweg STAP. STAP vergemakkelijkt het detecteren van bewegende doelen, maar het biedt slechts beperkte mogelijkheden om deze doelen ook af te beelden.
Dit proefschrift is het resultaat van onderzoek gedaan bij het International Research Centre for Telecommunications and Radar (IRCTR) van de Technische Universiteit in Delft in samenwerking met TNO Defensie en Veiligheid in Den Haag. Het doel was algemeen geldige signaalmodellen en optimale, maar toch snelle en efficiënte algoritmes te ontwikkelen die SAR en STAP technieken combineren. De theoretische resultaten zijn geverifieerd met behulp van gemeten radardata. Het onderzoek beantwoordt de volgende vragen:
Heeft een combinatie van SAR en STAP technieken voordelen? Als het nodig is bewegende doelen met hoge (SAR) resolutie af te beelden, dan moet er een algemeen geldig signaalmodel ontwikkeld worden voor de gegeven meetgeometrie. In de open literatuur zijn inversiemethoden voor zulke modellen gevonden, maar slechts voor enkele specifieke gevallen. Deze aanpak is met name bruikbaar om synthetische radardata te genereren voor het analyseren van SAR/MTI technieken of voor het onderzoeken van nieuwe, mogelijk interessante toepassingen zoals MTI met *ultra-*

wideband grondradar.
Is het mogelijk om een snel maar optimaal of bijna optimaal MTI algoritme te vinden? Als de ontvangstkanalen goed gekalibreerd zijn, kunnen bewegende doelen gedetecteerd worden door de signalen van alle kanalen te middelen. Deze techniek levert een zeer efficiënt MTI algoritme op, omdat het kanaalgemiddelde snel te berekenen is. Een dergelijk zeer snel algoritme bestaat dan ook al, maar het is nog niet experimenteel geverifieerd.
Hoe presteert een dergelijk algoritme als het op experimentele data wordt toegepast? Een bekend STAP algoritme en het algoritme gebaseerd op het kanaalgemiddelde zijn toegepast op twee experimentele datasets: MCARM data en SOSTAR-X data. De resultaten tonen aan dat de afwijkingen tussen de ontvangstkanalen met een simpel model beschreven kunnen worden, ondanks dat de kanaalafwijkingen in de SOSTAR-X data erg groot zijn, in tegenstelling tot de MCARM data. De prestaties van de MTI algoritmen zijn bevredigend voor beide datasets.
Wat zijn nieuwe, interessante toepassingen voor STAP? Een nieuwe toepassing voor STAP technieken is het detecteren van slachtoffers die bedolven zijn na bijvoorbeeld een natuurramp of een terroristische aanval. Bij IRCTR zijn verschillende experimenten uitgevoerd met *ultrawideband* grondradar om de mogelijkheden van STAP voor deze nieuwe toepassing te onderzoeken. De experimentele resultaten komen goed overeen met de theoretische modellen.

De belangrijkste resultaten van het onderzoek zijn:
Uitgebreide signaalmodellen voor meer-kanaals SAR (MSAR) MTI. Het proefschrift vult TNO's kennis inzake enkel-kanaals SAR MTI algoritmes aan. Het bouwt voort op idee□n uit de open literatuur en beschrijft een algemene uitdrukking voor de MSAR overdrachtsfunctie.
Heuristisch onderzoek van de foutbronnen in meetdata. Een simpel model voor MTI vanuit de lucht is getest met behulp van MCARM en SOSTAR-X meetdata. Het model verwaarloost beweging van de achtergrond en eventuele afwijkingen van een recht vliegpad en er is aangenomen dat de kanaalafwijkingen tijdsonafhankelijk zijn. In de open literatuur zijn geen resultaten van STAP algoritmen gevonden die gemakkelijk vergeleken kunnen worden met dit model. Een diepgaande vergelijking wordt daarom in dit proefschrift uitgewerkt. Dit heuristische onderzoek heeft waardevolle inzichten opgeleverd wat betreft de interpretatie van SOSTAR-X data.
Een nieuwe toepassing voor STAP: detectie van bedolven slachtoffers. Het detecteren van mensen die bedolven zijn, na bijvoorbeeld een aardbeving, is een nieuwe toepassing voor STAP technieken. In dit geval is de detectie gebaseerd op de zeer kleine ademhalingsbewegingen van een persoon. MSAR MTI is zeer bruikbaar voor deze toepassing omdat het een hoge resolutie combineert met de mogelijkheid om minieme bewegingen te detecteren. Voor deze toepassing wordt een zijwaarts gerichte an-

tenne gebruikt in plaats van een naar beneden gerichte antenne zoals gebruikelijk is bij grondradar. In het proefschrift worden de eerste resultaten verkregen met experimentele data gepresenteerd.

Nomenclature

α	Relative speed of target in SAR scene with respect to radar
α_c	Quadratic coefficient of chirp signal phase
β	Slope of the clutter ridge
$\Delta\tau$	Slow time interval
Δd	Distance between two adjacent elements of antenna array
$\Delta d'$	Sampling interval in domain d'
Δu	Slow time domain interval
γ	Reciprocal value of the constant β: $\gamma = 1/\beta$
κ, ζ	Dummy variables
λ	Wavelength
λ_k	Singular value
λ_{reg}	Regularisation parameter
Ω	Spectral support limit
ω	Angular frequency
ω_c	Carrier angular frequency
ω_i	Normalised Doppler frequency of the i^{th} target
ϕ	Squint angle
$\psi(x)$	Phase function
ρ^2	Variance

σ	Radar target cross section
$\mathbf{\Sigma}$	Diagonal matrix of singular values
τ	Slow time
θ	Depression (elevation/grazing) angle
θ_i	Normalised spatial frequency of the i^{th} target
θ_R	Angle in radians
A,B,C,D,	
E,A',B',C'	Points in (x, z) plane
$\boldsymbol{A}$	Complex matrix
a, b	Target's relative azimuth and velocity, respectively
A_e	Antenna effective aperture
A_k	Amplitude of the k^{th} stationary target
B_l	Amplitude of the l^{th} moving target
c	Wave propagation speed
$\mathbb{C}$	Set of complex numbers
D	Antenna array aperture size
d	Antenna array (sensor) domain
$\boldsymbol{d}$	Row vector composed of samples in d domain
D'	Constant denoting the support of resampled domain d
d'	Resampled antenna array domain d
D_g	Distance in slant plane
d_n	Sampled antenna array domain
D_s	Distance in ground plane
$\boldsymbol{E}_k$	Rank-1 matrix

$e(d)$	Complex gain function
$E(k_d)$	Fourier transform of complex gain function $e(d)$
F	Fresnel number
$\boldsymbol{f}, \boldsymbol{h}$	Vectors decomposing matrix $\boldsymbol{S}$
$\mathcal{F}$	Forward Fourier transform operator
$\mathcal{F}^{-1}$	Inverse Fourier transform operator
$f(u), h(d)$	Orthogonal functions decomposing stationary target's signal shifted by s_s
$f(x, y)$	Target function in spatial domain
$F_0(k_x)$	Spectrum of the reflectivity function
$f_0(x)$	Reflectivity function
$G(k_x, k_y, k_{v_x})$	Spectrum of the target domain $g(x, y, v_x)$
$g(x, y, v_x)$	Target domain composed of stationary and moving targets
G_a	Antenna gain
$I(k)$	Oscillatory integral
K	Number of stationary targets
k	Wavenumber: $k = \omega/c$
k_d	Spatial frequency or wavenumber domain for angular real aperture d; angular (frequency) domain
k_u	Spatial frequency or wavenumber domain for azimuthal synthetic aperture u; slow time Doppler (frequency) domain
k_x, k_y	Spatial frequency coordinates
$k_{d,0}$	Location of stationary targets shifted by function s_s in k_d domain
$k_{d,l}$	Location of the l^{th} moving target shifted by function s_s in k_d domain
$k_{u,k}$	Location of the k^{th} stationary target shifted by function s_s in k_u domain

$k_{u,l}$	Location of the l^{th} moving target shifted by function s_s in k_u domain
k_{v_x}	Spectral domain corresponding to radial velocity
L	Half-size of synthetic aperture
M	Number of azimuth samples
M_i	Number of point reflectors
N	Number of sensors in an antenna array
$\mathbb{N}$	Set of integers
$\mathcal{N}$	Random Gaussian complex number
$N(\omega)$	Spectrum of Gaussian noise
O	Number of moving targets
P	Number of range samples
$P(\omega)$	Spectrum of the radar pulse
$p(t)$	Radar base band pulse
P_t	Transmitted power
P_r	Received power
q, q'	Auxiliary power coefficients
R	Distance from the centre of the imaged area
$\mathbb{R}$	Set of real numbers
$r(x, y, u, d)$	Round trip distance
R_1	Radius of an imaged area
$\boldsymbol{S}$	Matrix composed of stationary targets' data in (u, d) domain
$\hat{S}(\omega)$	Estimated signal spectrum
$S(\omega)$	Signal spectrum
$S(k_u, \omega, k_d)$	Spectrum of the received radar signal $s(u, t, d)$

$s(t)$	Signal in time
$s(u,t,d)$	Echoed radar signal from target area
$s_0(k,u,d)$	Reference function
$s_a(u,d)$	Echoed signal from stationary targets
$s_b(u,d)$	Echoed signal form moving targets
$s_c(k,u,d)$	Digitally focused (compressed) echoed radar signal
$\boldsymbol{S_m}$	Matrix composed of moving targets' data in (u,d) domain
$s_s(k_u,d)$	Shifting function
t	Fast time
T_p	Pulse repetition interval
t_{R_2}	Time delay corresponding to distance R_2
u	Synthetic aperture or slow time domain
$\boldsymbol{U}$	Matrix of left singular vectors
$\boldsymbol{u}$	Column vector composed of samples in u domain
$\boldsymbol{u}_k$	Left singular vector
$u(n,l)$	Normalised signal returned by a target
u_m	Synthetic aperture sampled points
$\boldsymbol{V}$	Matrix of right singular vectors
$\boldsymbol{v}_k$	Right singular vector
v_a, v_b	Relative target velocities in x and y directions, respectively
v_r	Radar platform velocity
v_x, v_y	Target's velocity components in (x,y) plane
v_{ai}	Moving target's relative radial velocity: $v_{ai} = v_{xi}/v_r$
v_{xi}, v_{yi}	Velocity coordinates of the i^{th} target

v_{xmax}	Maximum expected target velocity v_x
$W(\omega)$	Window function
$w(x)$	Test function
w_1, w_2	Auxiliary variables corresponding to domains u and d, respectively
x', y'	Auxiliary transformed spatial coordinates
X, Y	Motion transformed spatial domain coordinates
x, y, z	Spatial coordinates
X_1, Y_1	Centre of the imaged area
x_i, y_i	Spatial coordinates of the i^{th} target
$\boldsymbol{Z}$	Matrix composed of targets' data in (u, d) domain
FFT	Fast Fourier transform
GPR	Ground penetrating radar
ICA	Independent component analysis
IRCTR	International Research Centre for Telecommunications and Radar
MCARM	Multi-channel airborne radar measurement
MSAR	multi-channel SAR
MTD	Moving target detection
MTI	Moving target indication
PCA	Principal components analysis
PSF	Point spread function
Radar	Radio detection and ranging
SAR	Synthetic aperture radar
SOSTAR	Stand-off surveillance & target acquisition radar
STAP	Space-time adaptive processing

SVD	Singular value decomposition
TNO	Nederlandse Organisatie voor Toegepast Natuurwetenschappelijk Onderzoek
UWB	Ultra-wide band

The art of using troops is this: When ten to the enemy's one, surround him; When five times his strength, attack him; If double his strength, divide him.

Sun Tzu: *The Art of War*

At least, he consoled himself, by the look of the antenna arrays it was only old-fashioned meter-wave-length stuff, so it couldn't be very interesting.

Arthur C. Clarke, *Glide Path*

Chapter 1

Introduction

Radar (RAdio Detection And Ranging) has been used since its invention in 1904 in numerous applications involving measurements of position and speed [41]. Its main advantages are the capability to perform these measurements over long distances even in darkness, or during adverse weather conditions such as fog. These capabilities have been recently extended to ground penetrating [32] and through-the-wall sensing radar [21].

Moving Target Indication (MTI) radar is defined as a device capable of detecting moving targets in presence of an interfering background (usually called *clutter*) [24]. The difference between target and clutter velocities is exploited for target detection. Radar MTI is of great interest in civil and military applications; for instance, its uses include airborne or space-borne surveillance of ground moving vehicles (cars, trains) or ships at sea. Recent systems utilize multi-channel radars to achieve the best possible separation of moving objects from the stationary ones. The implementation of multi-channel MTI in radar is called *space-time adaptive processing*, or STAP.

STAP is a field of study in signal processing concerned with the use of spatial as well as temporal data in phased array antennas. Since phased array antennas are structures of sensors arranged in space, each sensor recording data in time, the term space-time processing is often used. The word "adaptive" refers to the case when array processing is based on parameters estimated from measured data. It is mostly formulated as an optimisation problem [19].

Angular or 'spatial' resolution of any image-forming device has an empirical limit called the *Rayleigh criterion*

$$\theta_R \approx \frac{\lambda}{D}, \tag{1.1}$$

where θ_R is an angle in radians, λ is the wavelength of the observed radiation and D is the size of the aperture. If two point-like sources are separated by a smaller angle than θ_R, they cannot be resolved. This relation suggests that to improve the resolution by making θ_R smaller, the wavelength needs to decrease or the radar an-

tenna aperture needs to increase. *A synthetic aperture radar* (SAR) can circumvent the problem by utilising the relative motion between an observed object and the image-forming device [40].

1.1 Key questions

This thesis is a result of research jointly performed at the International Research Centre for Telecommunications and Radar (IRCTR) associated with Delft University of Technology and the TNO Defence, Security and Safety in the Hague, the Netherlands. The research was motivated by the following, not yet answered questions:

Are there any benefits in combining SAR and STAP models? TNO has a long track record in the design of radar systems with SAR and MTI capability. Due to design constraints, the SAR and MTI modes are typically implemented separately in airborne radar. Would it be advantageous to develop a *model* of a single system that includes both modes?

Is it possible to find a fast yet optimal or near-optimal MTI algorithm? Optimal STAP algorithms are reported to be very costly to implement [24, Chapter 4]. What trade-offs are necessary to arrive at an optimal or near-optimal yet practical MTI algorithm?

How would such an algorithm perform when applied to measured data? Speed and efficiency come at the cost of simplified assumptions during modeling. Which effects play a major role in the data acquisition and which can be neglected?

How can we use STAP in a new fashion? STAP already has many applications in various radar systems (see [24] for instance). Can a new application based on the ongoing research at TNO or IRCTR be suggested?

1.2 Novelties in this thesis

Extended models for multi-channel SAR (MSAR) MTI :
This thesis complements TNO's expertise in single-channel SAR MTI algorithms. Chapter 3 builds on ideas in [12] *and provides more general closed-form expressions for the MSAR transfer function.* Ender has shown in [11] that generalised models could indeed bring improvements in terms of clutter suppression to the multi-channel MTI. He suggests using radar in a SAR mode for each channel. His subsequent work [12] provides a description of the MSAR signals and shows some ways to implement an optimal or near-optimal MTI algorithm.

Heuristic investigations into error sources in real data:
Applications of MTI algorithms from Chapter 4 *to Multi-Channel Airborne Radar Measurement (MCARM) [20] and Stand-Off Surveillance & Target Acquisition Radar (SOSTAR) [2] data are shown. Results with MCARM data* presented in Chapter 5 *allow for detailed comparisons with an alternative approach* published in [20]. Although deterministic techniques based on the singular value decomposition have already been applied to the MCARM data in [15], no easy comparison to other published attempts was found. The heuristic validation presented in this thesis provided insights in the interpretation of MCARM and SOSTAR data.

Novel application of STAP to detection of buried victims:
Section 5.1 describes *a new idea to use STAP for detection of moving objects buried underground or in debris*, during natural disasters, for example. The idea is based on the possibility of detecting a slight motion of the victims produced by breathing. MSAR MTI processing provides high spatial resolution due to the synthetic aperture concept and slow motion detection capability due to STAP. An alternative side-looking antenna configuration instead of the more traditional down-looking configuration is used. First results with measured data are presented.

1.3 Organisation of this thesis

Several basic concepts and models are summarised in **Chapter 2**. The chapter restricts the scope of this thesis.

Current models will cease to be valid when the ratio of the length of an antenna array to the distance from the imaged area is larger than a certain limit. For this case, extended models need to be considered. **Chapter 3** considers several such models and provides closed-form formulas for their inversion.

In **Chapter 4**, a unified look at the STAP processing from the deterministic point of view is provided and an access to optimal, real-time-implementable solutions for simplified cases is given. As already recognised by Ender in [12] using a statistical approach, it is shown in the deterministic fashion that clutter can be described by a rank one matrix.

Two datasets, one from MCARM and one from SOSTAR project, are used in **Chapter 5** to experimentally test the findings from Chapter 4. Since no airborne data was available to test the general SAR-MTI model, a laboratory experiment with a ground penetrating radar (GPR) was set up to produce a third dataset. This experiment showed a new potential application of SAR-MTI processing in the detection of human victims buried under rubble or earth during natural disasters.

Chapter 6 concludes this work with answers to the key questions. Recommendations for future work are given.

Chapter 2

Basic concepts

Traditionally, SAR and STAP encompass diverse approaches to modelling of the problems at hand. The ideas fundamental to the rest of this thesis are summarised in this section. Crucial terms are described here. First, one-dimensional echo imaging will be introduced as a basic concept used here to model imaging radars. *Imaging* is understood in this context as the ability to focus *moving or stationary objects* with equal resolution. Next, the stationary phase approximation will be briefly described as a mathematical tool to obtain a transfer function of a single or multi-channel SAR. Subsection on range-velocity echo imaging restricts the problem treated in this thesis. Finally, the mathematical technique of rank approximation of a matrix by means of singular value decomposition is reviewed for the use in MTI.

2.1 One-dimensional echo imaging

The basic ranging principle can be formulated as *one-dimensional echo imaging* [35]. Suppose that M_i point targets are situated in the field of view of the radar. The situation is shown in figure 2.1. The number M_i can be finite or infinite.

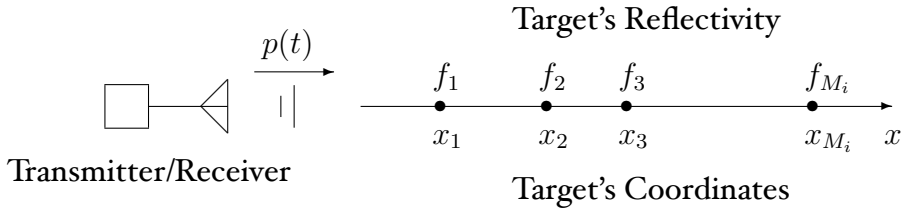

Figure 2.1: System geometry for one-dimensional echo imaging

Transmitter located at $x = 0$ illuminates the targets by sending a time-dependent signal $p(t)$. In our case, the transmitted signal has a finite time duration, thus it will

be called a *pulsed* signal. The receiver records echos from all targets in the field of view. The recorded signal can be represented as a sum of all waves reflected from the targets

$$s(t) \equiv \sum_{i=1}^{M_i} f_i p(t - 2t_i), \tag{2.1}$$

where $t_i \equiv \frac{x_i}{c}$ and c is the speed of light. We would like to identify the targets from the measurements of the signal $s(t)$. The expression for signal $s(t)$ can be rewritten via the following time-domain convolution (linear model)

$$s(t) = p(t) * f_0(x), \tag{2.2}$$

with

$$x \equiv \frac{ct}{2}, \tag{2.3}$$

where

$$f_0(x) \equiv \sum_{i=1}^{M_i} f_i \delta(x - x_i), \tag{2.4}$$

is a spatial domain signal composed of delta (Dirac) functions at the coordinates of the targets in the imaging scene. The amplitude of $f_0(x)$ at $x = x_i$ is equal to target's reflectivity at that point.

The imaging problem is solved if we could retrieve $f_0(x)$ from $s(t)$. For this process, one has to *reverse* the system model convolution in (2.2) to recover $f_0(x)$ from the observed signal. This operation is called *source deconvolution* [35].

The inversion or deconvolution in one-dimensional echo imaging can be formulated via taking the temporal Fourier transform of both sides of (2.2) that yields

$$S(\omega) = P(\omega)F_0(k_x), \tag{2.5}$$

where k_x is a linear function of ω

$$k_x \equiv \frac{2\omega}{c}. \tag{2.6}$$

Equation(2.5) is one of the corner stones of this thesis. To quote Soumekh in [35]: *[Equation (2.5) restricts] imaging problems examined [here] to linear system models, similar to a multidimensional convolution, relating the target information to the observed signal.*

The inverse or imaging problem is to seek a computationally manageable multidimensional signal processing method to perform the source deconvolution. (end quote)

Indeed, one can write

$$F_0(k_x) = \frac{S(\omega)}{P(\omega)}, \tag{2.7}$$

provided that $P(\omega) \neq 0$ for all ω. However, the condition necessary to perform the division is not satisfied in our case due to the pulsed nature of $p(t)$. In that case, a procedure called *Wiener filtering* [22] is applicable. It can be shown that the Wiener filter represents a least-square solution of an optimisation problem, where the objective is to obtain an estimate of an original signal from its filtered version corrupted by Gaussian noise, subject to a minimum error when compared to the original [42]. Thus, one can assume a more complicated model

$$\hat{S}(\omega) = P(\omega)F_0(k_x) + N(\omega), \tag{2.8}$$

where $N(\omega)$ is a spectrum of a Gaussian noise signal. Equation (2.7) then becomes [42, p. 547-549]

$$F_0(k_x) \approx \frac{\hat{S}(\omega)P^*(\omega)}{|P(\omega)|^2 + \lambda_{reg}}, \tag{2.9}$$

where λ_{reg} is a properly chosen regularisation parameter and * denotes complex conjugation. Note that if $\lambda_{reg} \to 0$, then equation 2.9 converges to equation 2.7. If $\lambda_{reg} \to \infty$, then equation 2.7 converges to a so-called *matched filter*:

$$F_0(k_x) \approx \hat{S}(\omega)P^*(\omega) \tag{2.10}$$

Formula 2.9 is fully applicable to the model (2.5) even without noise involved. Parameter λ_{reg} can be seen as a regularisation parameter that assures validity of the condition $P(\omega) \neq 0$ for all ω at the expense of accuracy of the solution. Its value shifts the solution between two extremes: Wiener filter and matched filter.

If the spectrum of $S(\omega)$ occupies a narrow frequency band, it needs to to be modulated by a harmonic signal $\exp(\jmath\omega_c t)$ having a certain *carrier angular frequency* ω_c in order to be successfully radiated by an antenna. Prior to digital processing, the received signal $s(t)$ is converted back to baseband to reduce the necessary sampling rate. In the case of ultra-wide band (UWB) radars, $S(\omega)$ occupies an extremely wide frequency band centred around $\omega_c = 0$ and can be transmitted without any modulation.

Figure 2.2 shows an example of a target function $f_0(x) = \mathcal{F}^{-1}\{F_0(k_x)\}$ produced by one target and estimated by Wiener filtering (sharp spike) and matched filtering ($|\sin(x)/x|$ shape). Even though this particular case was generated for a rectangular

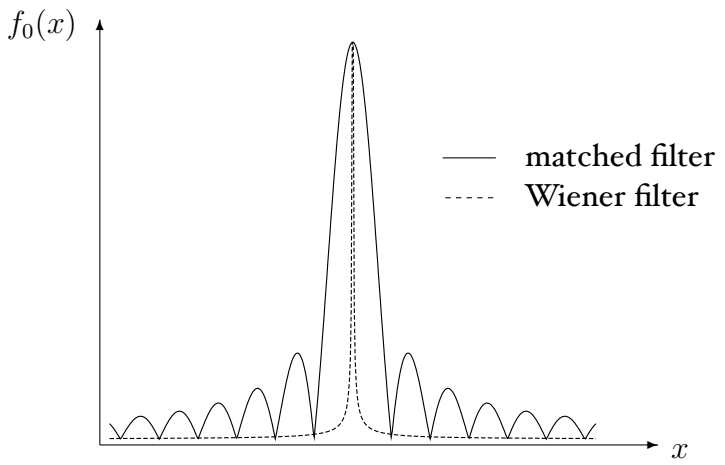

Figure 2.2: Impulse response of Wiener filter (dashed line) and matched filter (solid line).

pulse shape, we note that the matched filter response will always exhibit side lobes if $P(\omega)$ is band limited. The model assumed is the noiseless case as in (2.5).

The mapping of k_x to ω is linear in (2.5). Generally, such mapping can be non-linear. An interpolation is then used to map one domain into another. This enables us to convert time domain shift variant systems into frequency domain shift invariant systems. Such conversion allows the use of fast algorithms that exploit shift invariance, for instance FFT. Furthermore, interpolation allows us to scale the deconvolved output data: Often, the imaged area $x \in [x - R_1, x + R_1]$ is larger than the corresponding time interval $t \in [t - t_{R_2}, t + t_{R_2}]$ on which $s(t)$ is measured and vice versa (R_1 and t_{R_2} are arbitrary constants). In such cases, the resolution of the measured signal is different from the resolution of the imaged area. Since we know the mapping from k_x to ω, we can calculate $S(\omega)$ from the measured signal and interpolate it to required frequencies based on the area we expect to be imaged. The pulse spectral response $P(\omega)$ is known and can be calculated at any frequency ω. Artefacts due to insufficient sampling or due to interpolation may appear in the resulting spectrum. A low-pass filter is used before the final Fourier transform to regularise the solutions. In the spectral domain, the low-pass filter simply takes a form of a fixed window function $W(\omega)$ that multiplies signal $S(\omega)$:

$$W(\omega) = \begin{cases} 1, & \text{if} \quad -\Omega < \omega \leq \Omega \\ 0, & \text{elsewhere} \end{cases} \tag{2.11}$$

Thus, most of the algorithms used in this thesis for image reconstruction will follow the scheme shown in figure 2.3, which is a variant of algorithms described in [37, Section 5.6].

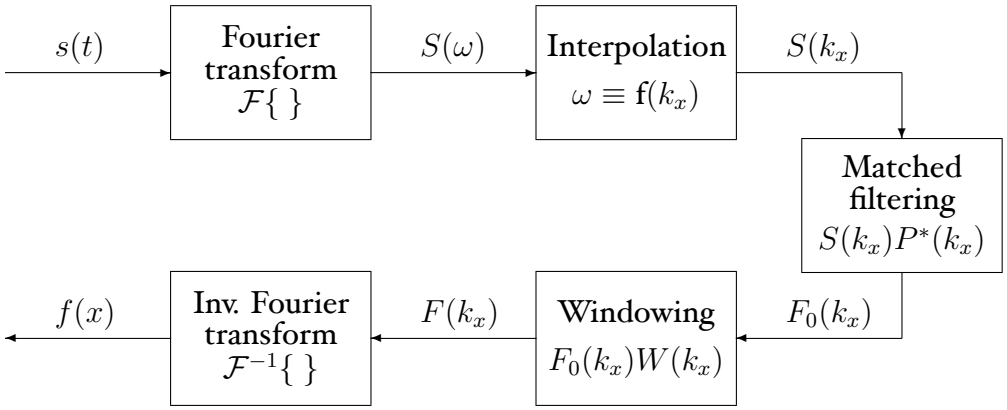

Figure 2.3: One-dimensional echo imaging via matched filtering.

A radar echo will be attenuated depending on the distance it travels. This attenuation (free space loss) is expressed by the so-called *radar equation* [34]

$$P_r = \frac{P_t G_a A_e \sigma}{(4\pi)^2 R_{max}^4}, \tag{2.12}$$

where P_t = transmitted power, Watts
G_a = antenna gain
A_e = antenna effective aperture, m^2
σ = radar target cross section, m^2
P_r = received power, Watts

The radar equation states, that the further the target, the weaker the echo due to the distance. Since methods and algorithms described in this thesis extract information from the phase of a signal rather than its amplitude, *the attenuation due to distance will be ignored in this thesis.*

2.2 Stationary phase approximation

Making use of relationships such as (2.5) requires knowledge of the spectral response of the filter, $P(\omega)$ in our case. Sometimes, an exact formula cannot be found and an approximate solution needs to be applied. *The method of stationary phase* is particularly suitable for waveforms encountered in radar. An excellent textbook [31] by Papoulis includes an introduction to the method from the system engineering point of view for one-dimensional problems. Derivations presented in this thesis

were inspired by a solution to a two-dimensional problem given by Dingle in [9]. Borovikov [7] describes the method in a highly advanced, mathematically rigorous fashion.

In mathematics, the stationary phase approximation is a basic principle of asymptotic analysis, applying to oscillatory integrals

$$I(k) = \int w(x) e^{\jmath k \psi(x)} \mathrm{d}x \tag{2.13}$$

taken over n-dimensional space $\mathbb{R}^n$ where the $\jmath = \sqrt{-1}$. Here ψ and w are real-valued smooth functions. The role of w is to ensure convergence; that is, w is a test function. The large real parameter k is considered in the limit as $k \to \infty$.

The idea is that the argument of the integral in equation (2.13) is a rapidly oscillating function for large k. Integrals of such functions tend to vanish outside of so-called *stationary points*. Thus, it makes sense to evaluate the argument of the integral at the stationary points only. These points are found as maxima, minima or saddle points of a phase function ψ which is composed of arguments of the exponential function in equation (2.13).

In order to illustrate the use of this method in this thesis, consider the following example. Suppose a baseband chirp radar pulse

$$p(t) = \begin{cases} \exp(j\alpha_c t^2), & \text{if} \quad 0 < t \leq t_2 \\ 0, & \text{elsewhere} \end{cases} \tag{2.14}$$

α_c is the chirp rate. An exact spectral representation of this signal can be found. Recall that the Fourier transform of a Gaussian function is also a Gaussian function. This means that

$$\mathcal{F}_{(t)} \left[\exp\left(-\frac{1}{2\rho^2} t^2 \right) \right] = \exp\left(-\frac{\rho^2}{2} \omega^2 \right) \tag{2.15}$$

scaled by a constant. Using the Gaussian Fourier pair with

$$-\frac{1}{2\rho^2} \equiv \jmath\alpha_c \tag{2.16}$$

will yield [35]

$$P(\omega) \approx \begin{cases} \exp\left(-\frac{\jmath}{4\alpha_c} \omega^2 \right), & \text{if} \quad \omega \in [-\Omega, \Omega]; \\ 0, & \text{otherwise.} \end{cases} \tag{2.17}$$

This is the formula for the phase of the chirp spectrum. For the sake of brevity, the amplitude term is left out and the spectrum is simply truncated according to Carson's bandwidth rule. Now, we shall apply the stationary phase approximation.

We wish to find an approximate solution to the integral that represents the Fourier transform of the chirp

$$P(\omega) = \int_{-\infty}^{\infty} \exp(\jmath\alpha_c t^2) \exp(-\jmath\omega t) \mathrm{d}t \tag{2.18}$$

The phase of the integrand will have one extremum which can be found by equating its first derivative to zero

$$\frac{\mathrm{d}}{\mathrm{d}t}\alpha_c t^2 - \omega t = 0 \tag{2.19}$$

We find that

$$t = \frac{\omega}{2\alpha_c} \tag{2.20}$$

at the stationary point. According to the stationary phase method, we can now evaluate the integrand at this point only, that is, magnitude terms neglected,

$$P(\omega) = \exp(\jmath\alpha_c \frac{\omega^2}{4\alpha_c^2}) \exp(-\jmath\frac{\omega^2}{2\alpha_c}), \tag{2.21}$$

and so

$$P(\omega) = \exp(-\jmath\frac{\omega^2}{4\alpha_c}) \tag{2.22}$$

Clearly, the asymptotic solution converges to the exact solution – as expected. This method has been an important tool in various fields of physics such as geometrical optics [38] and it is also well established in radar systems analysis, particularly in SAR [8].

2.3 Range-velocity echo imaging

We are going to define the *multi-channel airborne radar system* capable of range-velocity imaging as a device for multi-dimensional imaging by means of electromagnetic waves. This device will be in our case composed of an array of antennas that transmit and receive radio pulses. Antennas are arranged on a line in space to form a linear array. This array, placed on an aircraft, is aligned with axis u as shown in figure 2.4 and moves on a straight line along the same axis. Axes u and y are parallel.

As shown in figure 2.4, the original space where the problem exists is five-dimensional, that is three spatial and two velocity dimensions. However, we are going to restrict the number of dimensions to be reckoned with. A radar phased array cannot measure height in a configuration where its sensors are aligned with the direction of its motion. Hence, only two spatial dimensions will be taken into account. Namely, it will be assumed that $z = 0$. In real radar measurements where $z \neq 0$, targets'

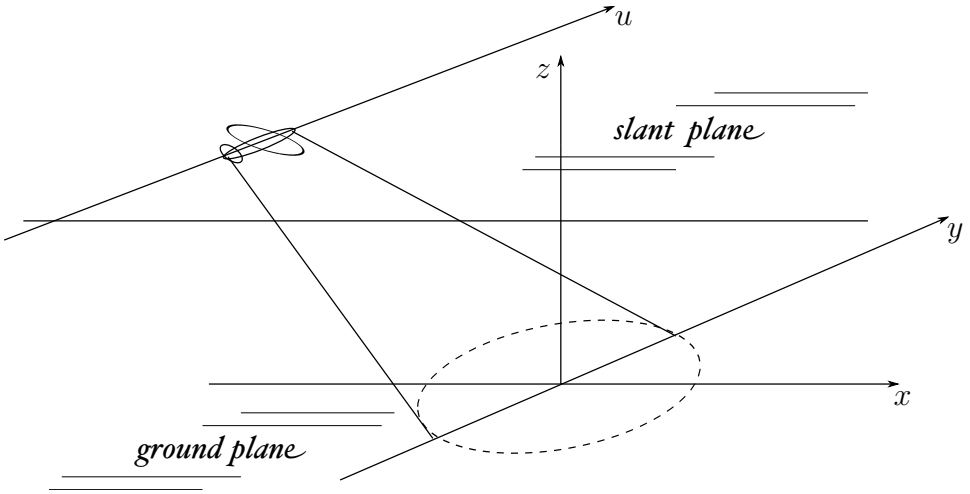

Figure 2.4: Range-velocity echo imaging, complete problem geometry.

positions are projected into a so-called *slant range*. This projection is illustrated by figure 2.5: suppose two objects A and B, separated by a distance D_g on the ground. Because viewed from an angle, the two points will appear to be at a distance D_s – closer together than they actually are. Since the angle AEB is approximately 90 degrees, one can say that D_g in a slant range representation is

$$D_s \approx D_g \cos\theta \tag{2.23}$$

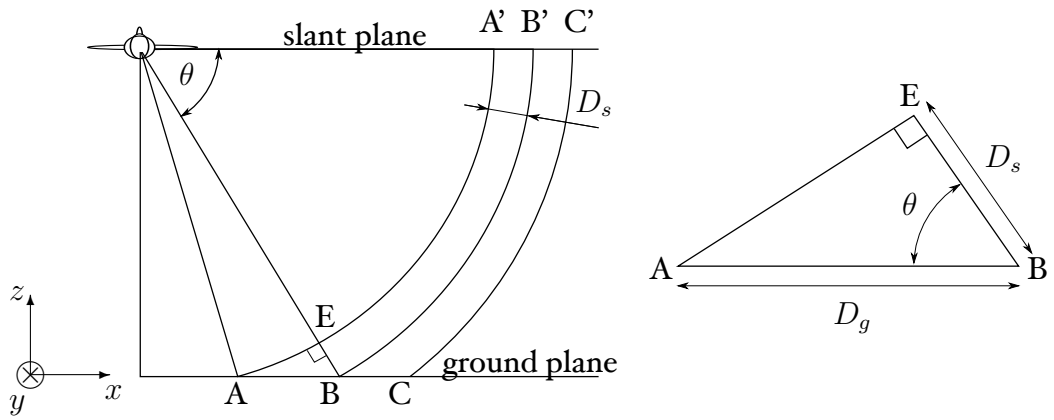

Figure 2.5: Slant range projection.

Thus, the distance in slant range representation is always less or equal the distance in the corresponding ground range projection. As the depression angle θ gets larger, D_s gets smaller for a given distance D_g. Thus the slant range representation

compresses the terrain features at near range more than at far range. However, one could note that from the image formation point of view, it does not matter which domain is chosen; one can form a focused image mapped into the slant range and convert it into the true ground range later.

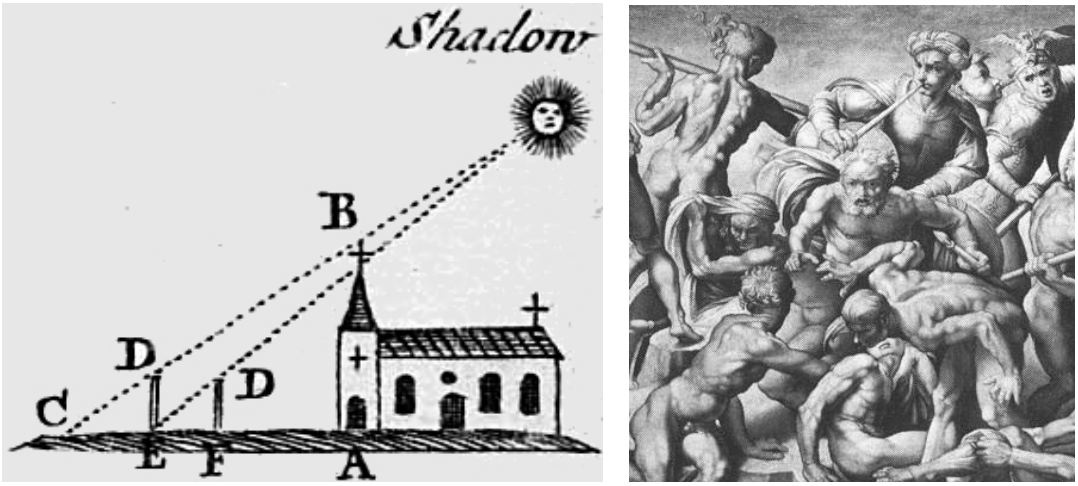

Figure 2.6: Left: Table of Opticks, Cyclopaedia, detail, taken from [44]. Right: Michelangelo Buonarroti: Battle of Cascina, detail of middle section, taken from [43].

There are additional effects that occur due to the fact that the imaged terrain is not flat (e.g. $z \neq 0$). The two most important ones are *shadowing* and *foreshortening*. Shadowing occurs when another object blocks the line-of-sight to an object to be imaged. Such object then will not be illuminated and therefore lie in a shadow. In figure 2.6, left, a single active source of radiation is represented by the sun. All objects located between the points E and A having a smaller height than the one marked by the line between the point E and the sun, will be shadowed by the largest object in the scene (the church). Foreshortening occurs when an object of a certain height is angled toward the viewer. One can then observe that an object appears shorter than it actually is. The warrior in the centre of the right picture in figure 2.6 appears to be much shorter than the others due to the foreshortening. Neither of these two effects can be mitigated in our geometry: in the first case, the object is simply invisible to radar. In the second case, if information about height is missing, the dimensions cannot be corrected for.

For the reasons mentioned in this subsection, only a two-dimensional problem will be considered. It will be assumed that all targets, moving or stationary, lie in a two-dimensional slant range plane (x, y), and that the radar array moves in the direction of the y-axis.

If a target moves on a two-dimensional plane (x, y), its velocity vector will also

have two components, (v_x, v_y). Thus the final solution space should span two spatial and two velocity dimensions. However, there is one more restriction used in this thesis. Only a three-dimensional domain (x, y, v_x) will be reconstructed. It has been shown many times [3, 25, 34] that the velocity vector component which is the easiest to measure by imaging radar (such as SAR) is in the direction to or from the radar sensor. In fact, it can be shown that imaging radar is much more sensitive to the v_x component than to the v_y component [45]. v_x is called *radial* or *cross-track* velocity vector component. As a consequence, if a target's velocity has a nonzero component v_y, it will be slightly smeared (de-focused) in the (x, y, v_x) domain. We can observe this smearing in examples from Chapter 3.

2.4 Multi-channel airborne MTI and the singular value decomposition (SVD)

The singular value decomposition is a relatively new mathematical technique. Although the concept has been known for some time, according to [29] as early as 1910, the first practical algorithm to actually compute it in an efficient way was published by G. Golub and W. Kahan in 1965. Together with the Fast Fourier Transform (FFT), the SVD is perhaps the most powerful and widely used tool in modern matrix computation. Therefore, it should not be surprising that it found its way into the field of airborne MTI as well. The SVD shall be briefly discussed in this section. The purpose is to quantitatively show how it can be used in analysis of airborne MTI radar data. For an exhaustive treatment of SVD, see reference [16].

Any real or complex matrix $\boldsymbol{A}$, even a non square one, can be written as the product of three matrices:

$$\boldsymbol{A} = \boldsymbol{U}\boldsymbol{\Sigma}\boldsymbol{V}^{\mathrm{T}} \tag{2.24}$$

The matrix $\boldsymbol{U}$ is orthogonal and has as many rows as $\boldsymbol{A}$. The matrix $\boldsymbol{V}$ is orthogonal and has as many columns as $\boldsymbol{A}$. The matrix $\boldsymbol{\Sigma}$ is the same size as $\boldsymbol{A}$, but its only nonzero elements are on the main diagonal (note that even a nonsquare matrix has a main diagonal). The diagonal elements of $\boldsymbol{\Sigma}$ are the singular values λ_n, and the columns of $\boldsymbol{U}$ and $\boldsymbol{V}$ are the left and right singular vectors $\boldsymbol{u}_k$ and $\boldsymbol{v}_k$, respectively.

The *rank* of a matrix is the number of linearly independent rows, which is the same as the number of linearly independent columns. The rank of a diagonal matrix is clearly the number of nonzero diagonal elements. Orthogonal transforms by matrices $\boldsymbol{U}$ and $\boldsymbol{V}$ preserve linear independence. Thus, the rank of any matrix is the number of nonzero singular values.

Let $\boldsymbol{E}_k$ denote the outer product of the k-th left and right singular vectors, that is

$$\boldsymbol{E}_k = \boldsymbol{u}_k \boldsymbol{v}_k^{\mathrm{T}} \tag{2.25}$$

Then, $\boldsymbol{A}$ can be expressed as a sum of rank-1 matrices,

$$\boldsymbol{A} = \sum_{k=1}^{n} \lambda_k \boldsymbol{E}_k \tag{2.26}$$

If we order the singular values in descending order, $\lambda_1 > \lambda_2 > \cdots > \lambda_n$, and truncate the sum after r terms, the result is a *rank-r approximation* to the original matrix. If this operation is done on a *centred* data matrix, that is, on a matrix with a mean of each column subtracted from the entire column, it is known as *principal components analysis* (PCA). PCA is usually described in terms of the eigenvalues and eigenvectors of the covariance matrix, $\boldsymbol{A}\boldsymbol{A}^{\mathrm{T}}$, but the SVD approach sometimes has better numerical properties [29].

Figure 2.7: Low-rank approximation of an MCARM data matrix: Left: full rank; Middle: rank 1; Right: full rank with $\lambda_1 = 0$.

To demonstrate the use of the SVD in this thesis, we analyse an example of a data matrix from the MCARM database treated in detail in Section 5.2. The original data matrix has a size 128-by-11. First, one SVD computation is performed. After computing a low-rank approximation using formula (2.26), the resulting data matrix is padded with zeros to the size 256-by-256 and the magnitude of its two-dimensional spectrum is computed. Figure 2.7 shows the spectra for the case for full rank, rank 1 and full rank when λ_1 is set to zero. What can be shown about this approach is that, under certain conditions, rank 1 approximation of such data matrix will actually correspond to all stationary targets' echos present in the data. Subtracting rank 1 approximation from the full rank matrix will filter the stationary targets out leaving only moving targets and noise in the data. It is easy to see from equation (2.26) that this operation is equal to setting $\lambda_1 = 0$ and computing (2.26).

By this time most of the people had drifted off. They didn't have the patience to watch me do this, but the only way to solve such a thing is patience!

Richard P. Feynman, *Surely, you're joking Mr. Feynman!*

Chapter 3

General Approach to Multi-Channel MTI

This chapter outlines a solution to the multi-channel moving target *imaging*, indication and detection (MTI/MTD) by means of inverse systems approach. First, the problem is presented in Section 3.1. Then, a general solution is given in Section 3.2 for the case of stationary targets. The separation scheme proposed in this section is the most general one derived in the thesis. However, it is not the most practical one, due to its computational cost. Section 3.3 attempts to find a spectral response of moving targets in a fashion similar to the stationary case. The main idea to be conveyed by this chapter is that the separation of moving targets from the stationary ones can be tackled by applying the solution derived for stationary targets on a moving targets' model – as illustrated in Section 3.4. This is achieved here by a perfect knowledge of the problem geometry and parameters related to the radar itself, such as the radar platform velocity and altitude, the radar carrier frequency and the radar pulse repetition frequency. Spatial distributions of stationary or moving targets do not play a role in the problem formulation nor in its solution. This alleviates the need for estimation of any statistical properties of the targets. Section 3.5 introduces an approximated, yet accurate and practical algorithm based on SAR processing. Finally, some numerical experiments are put forth by Section 3.6.

3.1 Problem formulation

Even though there is ongoing research to improve resolution of spectral estimators for STAP, e.g. the Wiener filter described by equation (2.9), this improvement cannot cross a certain limit, given by the level of noise present in the signal. When that level is reached (even if only theoretically), increasing the antenna array size is a way to improve the resolution further. Current STAP models consider so-called *far-field*

diffraction. Namely, in these models, the following inequality holds

$$\frac{D^2}{R\lambda} \ll 1, \tag{3.1}$$

where D is the antenna array length, $R = \sqrt{X_1^2 + Y_1^2}$ is the distance of the array from the centre of the imaged area and λ is the wavelength of the transmitted signal. In this chapter, close ranges where the phase of the wave impinging on an antenna array is nonlinear are considered. At longer ranges, our approach is possible but it offers little benefit. The *near-field diffraction* occurs when

$$\frac{D^2}{R\lambda} \geq 1 \tag{3.2}$$

Examples in this chapter consider the Fresnel number $F = D^2/(R\lambda)$ in orders of 0.1 to 50. That means both cases of far-field and near-field diffraction are taken into account.

The problem scenario is depicted in figure 3.1. A side-looking phased array of a length D with its sensors aligned along the coordinate u is placed on an aircraft. The aircraft is moving along the coordinate u, on a straight line, on an interval $[-L, L]$ which is centred at coordinates $(x, y) = (X_1, Y_1)$. The radar footprint is binding a region to be imaged. The centre of this region is located at coordinates $(x, y) = (0, 0)$. Targets are located in the x, y plane, y coordinate is parallel to the u coordinate. If some targets are moving, their velocity vector will be (v_x, v_y). It is assumed that because radar impulses travel at the speed of light, a radar platform will move only slightly during the acquisition of all the echos coming back as a response to each pulse transmitted. As a result, this movement can be neglected and a so-called *stop-and-go approximation* can be used; this approximation assumes the radar platform to stop at a position u_m, to make a measurement, then to stop at a position u_{m+1}, make another measurement and so forth.

Suppose the phased array measures a signal $s(u, t, d)$, where t is time and u, d are spatial coordinates. Further, suppose we wish to form a function $g(x, y, v_x)$ from the measured signal s, where g contains points in coordinate system (x, y, v_x). In order to solve the problem by means of the Fourier transform, we need to find the following inversion:

$$G(k_x, k_y, k_{v_x}) = \exp\left[-\jmath(k_x X_1 + k_y Y_1)\right] S(k_u, \omega, k_d), \tag{3.3}$$

where function $S(k_u, \omega, k_d)$ is the three-dimensional Fourier transform of a received signal, $G(k_x, k_y, k_{v_x})$ is the three-dimensional Fourier transform of the target domain $g(x, y, v_x)$ of points focused at coordinates (x_i, y_i, v_{xi}). k_x, k_y, k_{v_x} are frequencies corresponding to coordinates (x, y, v_x), respectively. $\omega = 2\pi f$ is the angular frequency, corresponding to time t, k_u and k_d are spatial frequencies corresponding to

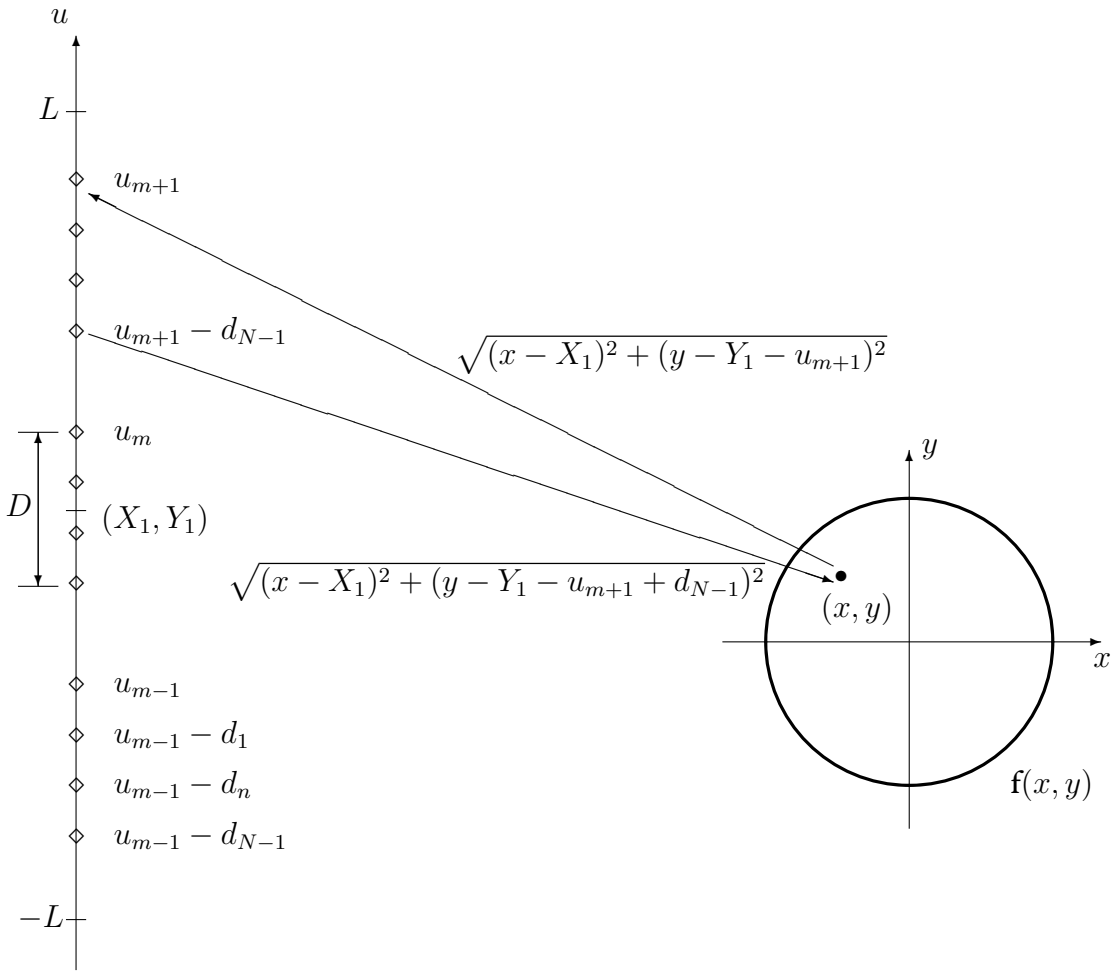

Figure 3.1: Imaging system geometry for airborne multi-channel MTI.

spatial coordinates u and d. The exponential function shifts the imaged domain in space; it is a form of a base-band conversion.

The reason why we are trying to obtain the result in this particular form is simple: We want to take advantage of fast implementations of a convolution in the spectral domain. To give an example, we consider a two-dimensional sampled (u, d) domain of a size $M \times N$. Algorithms to numerically compute the two-dimensional Fourier transform of this domain, such as an FFT, and its inverse have computational complexity typically $O(2NM[\ln(N) + \ln(M)])$. The STAP algorithm used in this thesis is based on singular value decomposition which requires $O(MN^2)$ multiplications, where $M \geq N$. A simple comparison is shown in table 3.1. The computational complexity of SVD is compared to the one of two-dimensional FFT for values of M and N written as powers of 2. When $M \approx N$, the FFT needs less multiplications than SVD for values above approximately 16. Even though the SVD is actually less complex for some values of M and N, it should be noted that the SVD-based STAP algorithms will only remove stationary targets. They will not provide focusing of the moving targets.

Table 3.1: Computational complexity comparison. o – 2D-FFT less complex than SVD, x – SVD less complex than 2D-FFT. $M = 2^q$, $N = 2^{q'}$

q/q'	1	2	3	4	5	6	7	8	9
1	x	x	x	x	x	x	x	x	x
2	x	x	x	x	x	x	x	x	x
3	x	x	x	x	x	x	x	x	x
4	x	x	x	o	o	o	o	x	x
5	x	x	x	o	o	o	o	o	o
6	x	x	x	o	o	o	o	o	o
7	x	x	x	o	o	o	o	o	o
8	x	x	x	x	o	o	o	o	o
9	x	x	x	x	o	o	o	o	o

In order to arrive at the relation given by equation (3.3), we need to obtain the solution as a product of the spectrum of the signal at the input and a linear function of space and velocity. In that case, the inverse Fourier transform of this product will yield directly the data in the space and velocity coordinates at the output. A mapping between (k_x, k_y, k_{v_x}) and (k_u, ω, k_d) needs to be defined in a form of some coordinate transformation. This is a crucial step in a Fourier based inverse problem formulation. Several of such transformations will be given in the following sections. Due to high computational costs, it is desirable that the transformation be as simple as possible with as low dimensionality as possible.

3.2 Inverse problem solution for stationary targets

The model used is an extended version of the bi-static SAR model derived in [37, Chapter 8]. The difference is in the treatment of the parameter d. In a bi-static model, it is a constant, since the radar array is composed of two sensors only. In our case, d is a variable. This variable is discrete due to a discrete number of sensors in the array (and thus their discrete positions d_n). Also the variable u should be discrete due to the stop-and-go approximation. However, the only difference in the spectral analysis is the periodicity of a discrete signal's spectrum. As long as aliasing is avoided a ***continuous*** model can be used.

Another simplification involves infinite aperture lengths L and D. That is, we are going to suppose that the aircraft is carrying a phased array of an infinite length and it travels from $-\infty$ to ∞. Also all amplitude functions with the exception of target reflectivity functions are suppressed, as they do not play a role in the image formation. This approach greatly simplifies the mathematics of the problem with the results still applicable to a discrete case. Naturally, finite dimensions L and D are used in numerical simulations. These prerequisites are consistent with the previous work done in this field (e.g. reference [35]).

As a consequence, the spectra obtained for continuous phased arrays of infinite dimensions will then become periodic and convolved with the Fourier transform of the aperture functions. This influences the resolution of the solution, not its ability to provide a correct inverse. Reference [35] provides a discussion of sampling and finite aperture effects in great detail. Given the assumptions made above, a signal recorded by the radar can be written as

$$s(u,t,d) = \iint_{-\infty}^{\infty} f(x,y)\; p\left[t - \frac{r(x,y,u,d)}{c}\right] \mathrm{d}x\,\mathrm{d}y, \tag{3.4}$$

with r, the round trip distance given as

$$\begin{aligned} r(x,y,u,d) &= \sqrt{(x-X_1)^2 + (y-Y_1-u)^2} \\ &\quad + \sqrt{(x-X_1)^2 + (y-Y_1-u+d)^2} \end{aligned} \tag{3.5}$$

$f(x,y)$ is the target area's reflectivity function. It is a slice of the three-dimensional function $g(x,y,v_x)$ at $v_x = 0$

$$f(x,y) \equiv g(x,y,0) \tag{3.6}$$

$p(t)$ represents a radar pulse. In our case we shall simply consider a rectangular pulse

$$p(t) = \begin{cases} 1, & \text{if} \quad 0 \le t < t_0 \\ 0, & \text{otherwise.} \end{cases} \tag{3.7}$$

The radar pulse travels a round trip distance r from a transmitter to a reflecting point at coordinates (x, y) and back to a receiver, experiencing a delay r/c, where c is the speed of light. Signal $s(u, t, d)$ records contributions from all points of the target area. Taking the temporal (*fast-time*) Fourier transform of both sides of (3.4) yields

$$s(u, \omega, d) = P(\omega) \iint_{-\infty}^{\infty} f(x, y) \exp\left[-\jmath k r(x, y, u, d)\right] \, \mathrm{d}x \, \mathrm{d}y, \tag{3.8}$$

where the wave number $k = \omega/c$. Term $P(\omega)$ can be removed either by means of Wiener filtering: $s(u, \omega, d)/P(\omega)$, or by means of matched filtering: $s(u, \omega, d) \times P^*(\omega)$. This operation concentrates the energy from radar pulses in the range direction, marking the instantaneous positions of the targets in this direction. The normalised or *range compressed* version of $s(u, \omega, d)$ is

$$s(u, \omega, d) = \iint_{-\infty}^{\infty} f(x, y) \exp\left[-\jmath k r(x, y, u, d)\right] \, \mathrm{d}x \, \mathrm{d}y. \tag{3.9}$$

As shown in Appendix A.1, the two-dimensional Fourier transform of both sides with respect to u and d yields

$$S(k_u, \omega, k_d) = \exp\left(\jmath X_1 k_x + \jmath k_y Y_1\right) F\left(k_x, k_y\right), \tag{3.10}$$

where

$$\begin{aligned} k_x &\equiv \sqrt{k^2 - (k_u + k_d)^2} + \sqrt{k^2 - k_d^2}, \\ k_y &\equiv k_u. \end{aligned} \tag{3.11}$$

Finally, from (3.10), we obtain the following inversion given by equation (3.3)

$$G(k_x, k_y, k_{vx}) = \exp\left(-\jmath X_1 k_x - \jmath k_y Y_1\right) S(k_u, \omega, k_d), \tag{3.12}$$

where

$$F(k_x, k_y) = G(k_x, k_y, 0). \tag{3.13}$$

Relation (3.11) dictates a rather complex interpolation from (k, k_u, k_d) domain to (k_x, k_y) domain. It is shown in Section 3.5 that a much more practical inversion scheme based on a SAR-like model inversion can be devised.

Since we defined $f(x, y)$ as $g(x, y, 0)$ we can write

$$f(x, y) = \mathcal{F}^{-1}_{(k_x, k_y)}\{F(k_x, k_y)\}, \tag{3.14}$$

meaning that to focus the two-dimensional *stationary* target domain using a three-dimensional signal $S(k_u, \omega, k_d)$, we only need to take a slice of the resulting three-dimensional spectrum at $k_d = 0$ and perform the two-dimensional inverse Fourier

transform. Thus, the shape of the function $G(\cdot)$ in k_{vx} domain is irrelevant in this case. However, we would like to use this inversion to focus a three-dimensional domain $g(x, y, v_x)$ in presence of moving targets in the signal, since the inversion given by equation 3.12 does not require any information about moving targets.

In order for this inversion to be useful for moving targets separation, we need to show that $G(k_x, k_y, k_{vx})$ has a finite extend in the v_x domain for stationary targets. We plot the so-called *point spread function* (PSF) of a single stationary target located at the origin of the imaged area in figure 3.2

$$|g(X_1, y, v_x)| = |\mathcal{F}^{-1}_{(k_x,k_y,k_{vx})}\{G(k_x, k_y, k_{vx})\}| \tag{3.15}$$

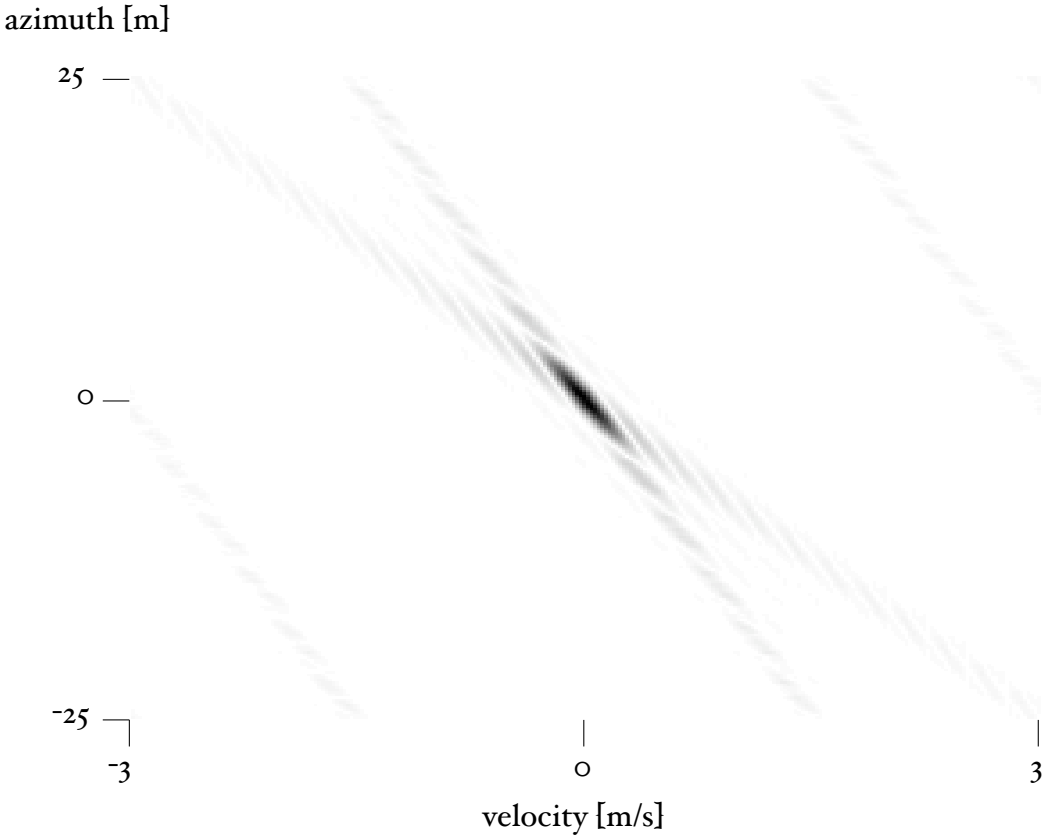

Figure 3.2: Point spread function of a stationary target located at $(x, y) = (0, 0)$ meters. Parameters: carrier angular frequency $\omega_c = 2\pi 10^9$ rad/s. $(X_1, Y_1) = (-1000, 0)$, $L = 30$ and $D = 120$ meters. The (y, v_x) domain was sampled with 256×256 samples. The pixels are scaled to 256 shades of grey; white is zero, black is the maximum.

We see that the focused point representing a stationary target does indeed have a finite extend in the velocity domain v_x. The side-lobes extend diagonally from

the centre instead of more usual perpendicular directions. This feature is common to other multi-static radars, see for example three-dimensional imaging with two-dimensional synthetic apertures in reference [37, Chapter 7]. The linear features in top right and bottom left corners of figure 3.2 are due to partial aliasing of the steeper diagonal line of side-lobes.

Point spread function indicates resolution of an imaging system and is, in fact, the autocorrelation of the signal produced by a single target. To see this, consider that for a single stationary target located at the origin of the imaged area, the spectrum of the signal recorded by radar is given as

$$S(k_u, \omega, k_d) = \exp\left[\jmath X_1 \left(\sqrt{k^2 - (k_u + k_d)^2} + \sqrt{k^2 - k_d^2}\right) + \jmath k_u Y_1\right] \tag{3.16}$$

Using equations (3.12) and (3.11) we get

$$G(k_x, k_y, v_x) = S(k_u, \omega, k_d) S^*(k_u, \omega, k_d) \tag{3.17}$$

In line with other authors, for instance [17, 24], we intend to use the (y, v_x) domain for moving targets separation. Thus, one can choose an arbitrary available range slice, for instance $x = X_1$. Focused targets (moving or stationary) present in this range slice will occupy a frequency slice in the spectral domain corresponding to the wave number $k = k_c$, where $k_c = \omega_c / c$. Hence,

$$G(k_x, k_y, v_x) = S(\omega_c, k_u, k_d) S^*(\omega_c, k_u, k_d), \tag{3.18}$$

and

$$g(X_1, y, v_x) = s(2k_c X_1, u, d) ** s(2k_c X_1, -u, -d), \tag{3.19}$$

where $**$ denotes the two-dimensional convolution in the (u, d) domain.

3.3 Inverse problem solution for moving targets

Consider a broadside target moving at a velocity (v_x, v_y). Analogically to the signal model defined by equation (3.4), one can write [35, Chapter 5]

$$s(u, t, d) = \iint_{-\infty}^{\infty} f(x + v_a u, y + v_b u)\ p\left[t - \frac{r(x, y, u, d)}{c}\right] \mathrm{d}x\, \mathrm{d}y, \tag{3.20}$$

where

$$v_a = v_x / v_r \tag{3.21}$$

$$v_b = v_y / v_r \tag{3.22}$$

with r, the round trip distance given as in equation (3.5). Here, $f(x, y)$ represents a moving target reflectivity function. It is difficult to evaluate the integral in equation (3.20) directly. However, it is possible to convert it to the previous case, where only stationary targets were considered. One can define the following substitution

$$x + v_a u = x' \tag{3.23}$$
$$y + v_b u = y' \tag{3.24}$$

Then, one can rewrite the equation (3.20) in the following fashion

$$s(u, t, d) = \iint_{-\infty}^{\infty} f(x', y')\ p\left[t - \frac{r(x', y', u, d)}{c}\right]\ \mathrm{d}x'\,\mathrm{d}y', \tag{3.25}$$

with

$$\begin{aligned} r(x', y', u, d) &= \sqrt{(x' - v_a u - X_1)^2 + (y' - v_b u - u)^2} \\ &\quad + \sqrt{(x' - v_a u - X_1)^2 + (y' - v_b u - u + d)^2} \end{aligned} \tag{3.26}$$

This relation is analogical to the stationary target model and it shows that a moving target can be modelled as a stationary target at a certain squint angle in transformed coordinates.

In order to show how a moving target can be extracted and possibly focused using the inversion derived in the previous section, a closed-form formula for a spectrum of a moving target will be given in this section. The model of the signals coming from moving targets located at coordinates (x_i, y_i) is given as [37, Chapter 8]

$$s(u, \omega, d) = \sum_i f(x_i, y_i) e^{\jmath\psi(u,d)} \tag{3.27}$$

with the phase function

$$\begin{aligned} &\psi(u, d) = \\ &-k\sqrt{(x_i - v_{xi}\tau)^2 + (y_i - v_{yi}\tau - v_r\tau)^2} \\ &-k\sqrt{(x_i - v_{xi}\tau)^2 + (y_i - v_{yi}\tau - v_r\tau + d)^2}, \end{aligned} \tag{3.28}$$

where v_{xi}, v_{yi} are velocities of a moving target in x and y directions, respectively. v_r is the radar velocity, and $u = v_r\tau$. Variable τ is essentially a time variable, since $\tau = u/v_r$. However, it was not taken into account when the signal in equation (3.25) was transformed into the spectral domain. This is the principle of the *stop-and-go* approximation: due to the fact that the radar pulse travels at the speed of light, the

phase function ψ varies much slower with respect to τ than it does with respect to k. Therefore, τ is considered constant while the Fourier transform of the signal in equation (3.25) from t to k is taking place. Hence, t is also called the *fast time* and τ is called the *slow time*.

Note that we write the measured signal $s(u, \omega, d)$ as a sum of contributions from discrete scatterers. Using the principle of superposition, one can first evaluate the spectrum of each scatterer and then sum the individual spectra to obtain a signal in the spectral domain. It is shown in Appendix A.2 that the spectral response of an individual scatterer depends on its position and velocity vector. Thus one can write

$$\begin{aligned} S(k_u, \omega, k_d) \;\approx\; & \sum_i f(x_i, y_i) \\ & \times \exp\left\{ \jmath \left[-X\sqrt{4k^2 - \left(\frac{k_u}{\alpha}\right)^2} - \frac{k_u}{\alpha} Y \right.\right. \\ & \left.\left. -\frac{x}{4k}\left(\frac{2kv_x}{v_r} - \frac{k_u}{\alpha} - 2k_d\right)^2 \right] \right\}, \end{aligned} \tag{3.29}$$

where:

$$\begin{aligned} X &= \frac{(v_{yi} + v_r)x_i - v_{xi}y_i}{\sqrt{v_{xi}^2 + (v_{yi} + v_r)^2}} \\ Y &= \frac{v_{xi}x_i + (v_{yi} + v_r)y_i}{\sqrt{v_{xi}^2 + (v_{yi} + v_r)^2}} \\ \alpha &= \frac{\sqrt{v_{xi}^2 + (v_{yi} + v_r)^2}}{v_r} \end{aligned} \tag{3.30}$$

To focus a particular target with reflectivity $f(x_i, y_i)$, one needs to know its speed vector (v_{xi}, v_{yi}). This is not possible, of course, since it is actually the velocity vector which is being estimated. One can also note that it is no longer possible to formulate the inversion in the same way as done in Section 3.2, since the domains (x, y) and (X, Y) are no longer the same. That is the reason why the double integral from equation (3.9) was replaced by the sum in equation (3.27). The purpose of this section was to provide a response of a moving target in the spectral domain. The following section will investigate the idea to apply the inversion given by equation (3.12) for stationary targets to moving targets' model in order to separate them.

3.4 Moving targets separation

In this section, it will be shown that a moving target will be displaced in the d domain after the focusing scheme given by formula (3.12) is applied. Suppose a broadside case ($Y_1 = 0$) and a moving target at coordinates $x_i = X_1$ and y_i with unit reflectivity, that is $g(X_1, y_i) = 1$. In order to simplify the solution, an approximate version of formula (3.12) will be used.

It is assumed that for slow speeds, one can have $\alpha \approx 1$. Should α be bigger than one, we would get a mismatch between the terms $X\sqrt{4k^2 - k_u^2}$ and $X_1\sqrt{4k^2 - k_u^2}$ which would then not cancel completely. Nevertheless, it makes sense to investigate slowly moving targets, as they are expected to be closest to the stationary ones. Further, we can set $v_y = 0$. For slow targets $v_r \gg v_x$ and so

$$X \approx x - \frac{v_x}{v_r}y, \qquad Y \approx \frac{v_x}{v_r}x + y,$$

because v_y only causes de-focusing [35]. Actually, it also changes the slope on which a moving target signature appears for various v_x, but it does not change the fact that moving targets will be displaced.

Further assuming that $kv_{xi}/v_r \ll 2(k_u + k_d)$ we could formally write (see Appendix A.2.1)

$$G(k_x, k_y, k_{v_x}) = \exp\left\{\jmath\left[\frac{v_{xi}}{v_r}y_i\sqrt{4k^2 - k_u^2} - k_u\left(y_i + \frac{2X_1v_{xi}}{v_r}\right) - k_d\frac{2X_1v_{xi}}{v_r}\right]\right\}, \tag{3.31}$$

where

$$\begin{aligned} k_x &\equiv \sqrt{4k^2 - k_u^2} \\ k_y &\equiv k_u \\ k_{v_x} &\equiv k_d \end{aligned} \tag{3.32}$$

The three-dimensional inverse Fourier transform of the function $G(k_x, k_y, k_{v_x})$ will yield a three-dimensional function $g(x'_i, y_i, v'_{xi})$, where

$$\begin{aligned} x'_i &\equiv \frac{v_{xi}}{v_r}y_i \\ y'_i &\equiv -y_i - \frac{2X_1v_{xi}}{v_r} \\ v'_{xi} &\equiv -\frac{2X_1v_{xi}}{v_r} \end{aligned} \tag{3.33}$$

The coordinate transform given by equation (3.33) *shifts* moving targets from their real positions to the new ones which also depend on their velocities. This shift is apparent in the simulation results in figure 3.7.

Since our focusing algorithms assume

$$g(x, y, v_x, v_y) \approx g(x, y, v_x), \tag{3.34}$$

velocity component v_y will introduce an error that manifests itself by slight smearing of the focused moving target signature. This smearing is apparent in some numerical examples shown in Section 3.6.

3.5 SAR-based inversion technique

Albeit approximately, we attempted to show that an inversion scheme derived for stationary targets will shift the moving targets along the third dimension: the velocity axis. Hence, one should succeed in extracting the moving targets from a stationary background. Note that our results do not depend on a particular distribution of stationary or moving targets, but the inversion method presented so far requires a complex 2-D interpolation scheme. This is very impractical due to the complexity and computational cost of 2-D interpolators. Interestingly, similarities between SAR phase functions and some terms in the phase functions derived above can be observed. The following section will present an inversion scheme based on standard SAR processing.

Recall the phase function from moving targets' model in equation (3.28). By using equation (A.34) in Appendix A.2

$$\psi(u, d) \approx -2k\sqrt{X^2 + \left(Y - \alpha u + \frac{d}{2}\right)^2} + \frac{kdv_x}{v_r} - \frac{kd^2}{4x} \tag{3.35}$$

the Fourier transform of $\exp[\jmath\psi(u, d)]$ with respect to u will give $\exp[\jmath\varphi(k_u, d)]$ with

$$\varphi(k_u, d) \approx -X\sqrt{4k^2 - \left(\frac{k_u}{\alpha}\right)^2} - \frac{k_u}{\alpha}\left(Y + \frac{d}{2}\right) - \frac{kdv_x}{v_r} - \frac{kd^2}{4x}, \tag{3.36}$$

where X, Y and α are again given by linear transformations from expression (3.30). At very low target velocities, $\alpha \approx 1$, some terms are approximated by

$$\sqrt{4k^2 - \left(\frac{k_u}{\alpha}\right)^2} \approx \sqrt{4k^2 - k_u^2} \tag{3.37}$$

$$k_u/\alpha \approx k_u \tag{3.38}$$

These terms appear also in the Fourier-based focusing for SAR. Setting $v_x, v_y = 0$ in equation (3.30) would yield

$$X = x_i \qquad \text{and} \qquad Y = y_i. \tag{3.39}$$

Therefore, if a moving target produces a signal $s(u, \omega, d)$ given by equation (3.27), one could suggest the following focusing scheme

$$g(x_i', y_i', k_v) = \mathcal{F}^{-1}_{(k_u,k)} \mathcal{F}_{(d)} \left\{ \exp\left[\jmath X_1 \sqrt{4k^2 - k_u^2} + \jmath \left(Y_1 + \frac{d}{2} \right) k_u \right] \exp\left(\jmath \frac{kd^2}{4x} \right) S(k_u, \omega, d) \right\}, \tag{3.40}$$

where $k_v = k v_a$ and $v_a = v_x / v_r$. Note that one does not get original coordinates (x_i, y_i) of a moving target but a ***shifted and rotated*** set (x_i', y_i') where the shift and rotation depend on the velocity vector. This result is consistent with the in-depth analysis of moving targets in single-channel SAR images given in [37, Section 6.4]. A schematic depiction of the focusing scheme given by equation (3.40) is shown in figure 3.3. The term $\exp[-\jmath k d^2/(4x)]$ can be identified as a phase correction term which compensates for the phase differences due to nonplanar waves impinging on the antenna array. It can be neglected in the far-field region where $D^2/(X_1 \lambda) \ll 1$, with λ being the wavelength of the received waveform. The remaining phase function in equation (3.40) translates coordinates from the measured domain into the imaged domain.

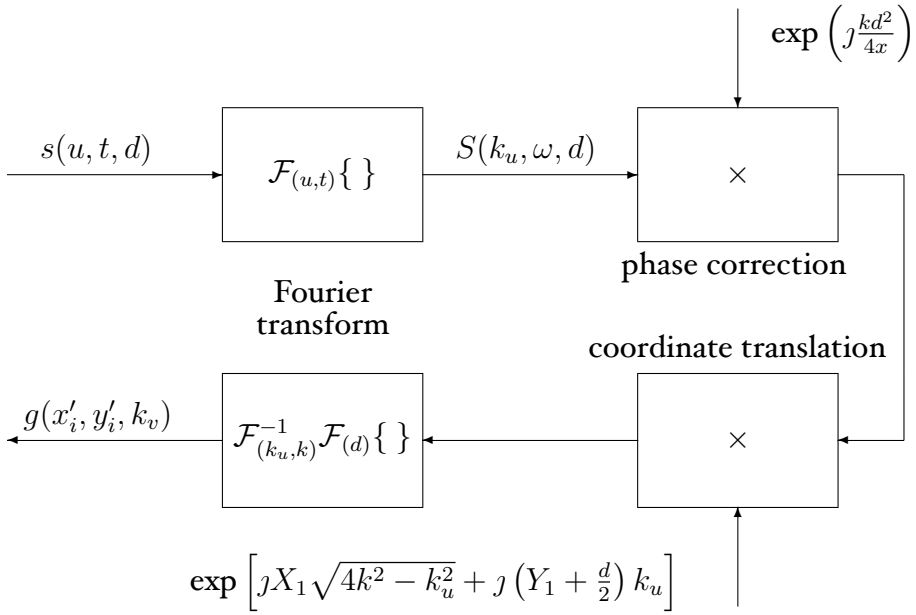

Figure 3.3: Schematic diagram of the SAR-based inversion.

We again test the usability of our approach by plotting the point spread function in figure 3.4. The directions in which the side-lobes extend are different when

compared to the generalised inversion in figure 3.2. This can be attributed to the different inversion formula used to produce the plot. Although it is generally difficult to to predict the behaviour of a multi-dimensional PSF, it is possible to obtain some quantitative comparisons of our two different inversions. The following reasoning was used: We are primarily interested in how well can two targets be discerned in azimuth and velocity domains. We can try to obtain "marginal" distributions of the PSFs in azimuth and velocity domains by adding all amplitudes in the two respective directions. What is obtained are projections that would appear if the PSFs were viewed sidewise from azimuth or velocity directions.

Figure 3.5 shows such comparison between figures 3.2 and 3.4. Amplitudes in each image are summed in velocity and azimuth directions and their absolute value is taken. Azimuth profiles are shown on the left. The full line represents the generalised inversion, the dashed line the SAR-based inversion. One can observe broader main lobes in case of the generalised inversion. This is caused by a more complex shape of the PSF. When the images of both PSFs in figures 3.2 and 3.4 are cut on the main diagonal, the profiles are identical with the azimuth profile corresponding to the SAR-based inversion. On the right hand side of figure 3.5, velocity profiles for both PSFs are shown. One can see that they are practically identical.

A closer look at the two-dimensional plots of PSFs in figures 3.2 and 3.4 reveals that perhaps there are some fine details that would indicate the superiority of the general inversion (the main lobe is narrower in the diagonal direction in figure 3.2, moving target appears to be less defocused in figure 3.7, top). However, given the difficulties connected with the multi-dimensional interpolation required for the general inversion, it would seem that the complexity of implementation outweighs potential merits of the general solution.

In order to estimate v_a, knowledge of k is necessary. One can observe that the x position of a target can be related to a particular wave number k; for instance, by noting that $k_x \approx 2k$ for $4k^2 \gg k_u^2$. Thus, k could be estimated from (x', y') and v_a could be calculated. However, such estimation is not currently accurate in practise, due to a small number of channels typically used in MTI phased arrays. This touches another important aspect of SAR MTI the so called *blind-angle problem* [4,35] referring to the fact that in general, velocity and azimuth of a moving target are mutually dependent in a single-sensor SAR data, which motivates the use of more sensors to resolve this ambiguity. However, the sole aim of the investigation presented here is to show the relation between SAR processing and multi-channel MTI and to establish the fact that moving targets will be displaced outside of the two-dimensional (x, y) domain in the third dimension: v_x. This fact can be used to separate moving targets from stationary ones. Also, it is possible to split the velocity domain into smaller parts for an easier velocity estimation.

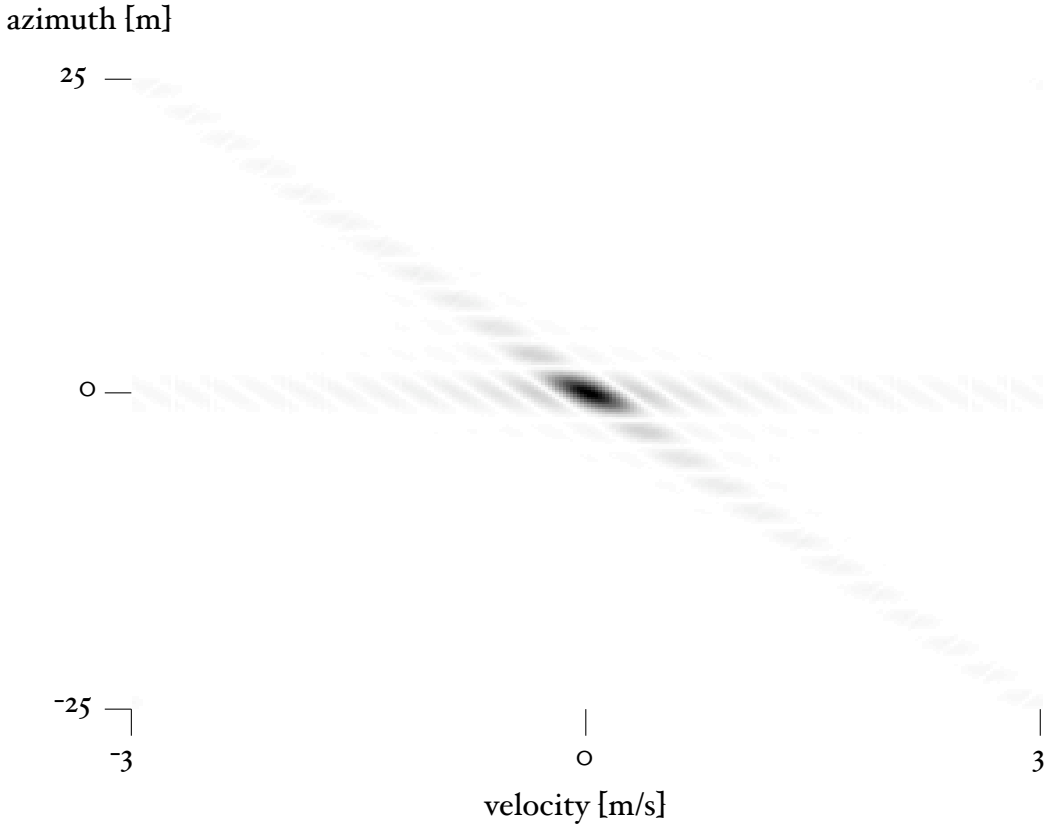

Figure 3.4: Point spread function for the SAR-based inversion. $(X_1, Y_1) = (-1000, 0)$ meters, carrier angular frequency $\omega_c = 2\pi 10^9$ rad/s. $L = 30$ and $D = 120$ meters. The (y, v_x) domain was sampled with 256×256 samples. The pixels are scaled to 256 shades of grey; white is zero, black is the maximum.

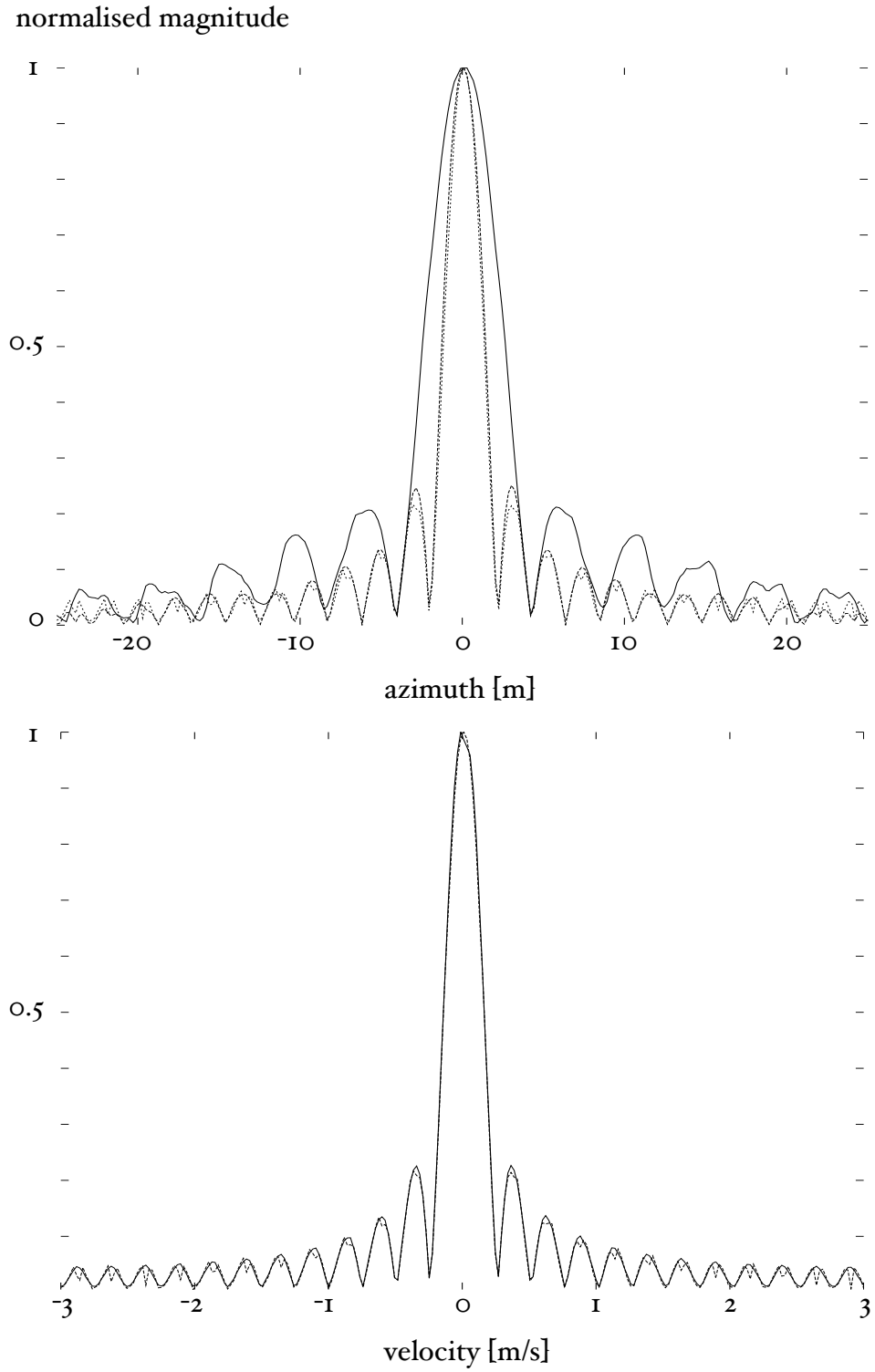

Figure 3.5: Comparison of point spread functions from figures 3.2 and 3.4. Line plots are formed by summing the values of the PSFs in azimuth and velocity directions and taking the magnitude of these sums: (top) azimuth profile, (bottom) velocity profile. Dashed line: SAR-based inversion. Full line: generalised inversion.

3.6 Simulations

The purpose of this section is to build a confidence in theoretical results found and stipulations made in this chapter. Inversions defined by equations (3.12) and (3.40) will be numerically tested for the case of multiple stationary targets and one moving target. Inversion defined by equation (3.12) was proposed for moving targets extraction in Section 3.2. However, due to its relative complexity, the subsequent theoretical analysis in Section 3.4 only *approximately* confirmed the validity of this inversion for moving targets separation. Numerical experiments testing the inversion (3.12) on moving targets will be shown next.

The layout of the general scenario considered in this section is depicted in figure 3.6. The simulated phased array consists of N sensors that are spaced with a distance $\Delta d = D/N$. Each sensor takes M measurements along the u coordinate. Thus, one can imagine that radar stops at positions u_m spaced $\Delta u = 2L/M$ apart, and it records all the responses for a time interval $\Delta\tau = \Delta u/v_r$ sampling it at a rate of P samples per $\Delta\tau$.

Ten stationary targets (designated "$\circ$") are aligned with the y axis at a distance X_1. A moving target (designated "$\bullet$") with a velocity vector v_t is located in the middle of this line. τ is sampled at much slower rate than t ($\Delta\tau$ is also called *pulse repetition interval*), τ is referred to as *slow time* and the sampled time variable t as *fast time*. So, with N sensors, M space, and P range acquisitions, one obtains a three-dimensional array called *datacube* of a size $M \times N \times P$. Since this chapter was concerned with normalised, that is *range compressed* (range focused) signal models, our calculations deal with the two-dimensional domain (d, u). We take a slice of the datacube at a particular range, namely X_1. That means we have taken a two-dimensional array $M \times N$.

3.6.1 Example 1

The simulation parameters are given as follows

parameter	ω_c	X_1	L	D	M	N	v_r	v_x	v_y
value	$2\pi 10^9$	-1000	30	120	256	256	100	-1	5
units	rad/s	m	m	m	–	–	m/s	m/s	m/s

Figure 3.7 shows results after the application of the inversion scheme for stationary targets to the data composed of stationary targets and a moving one. As expected, stationary targets are located on a straight vertical line. Even though the moving target is located on the broad side, we see it vertically shifted in Doppler (azimuth) domain in the figures. This is caused by the transformation (3.33). This transformation quantifies the shift for broad side moving targets processed by the SAR-based inversion as equal in angular and Doppler frequency domains. Indeed,

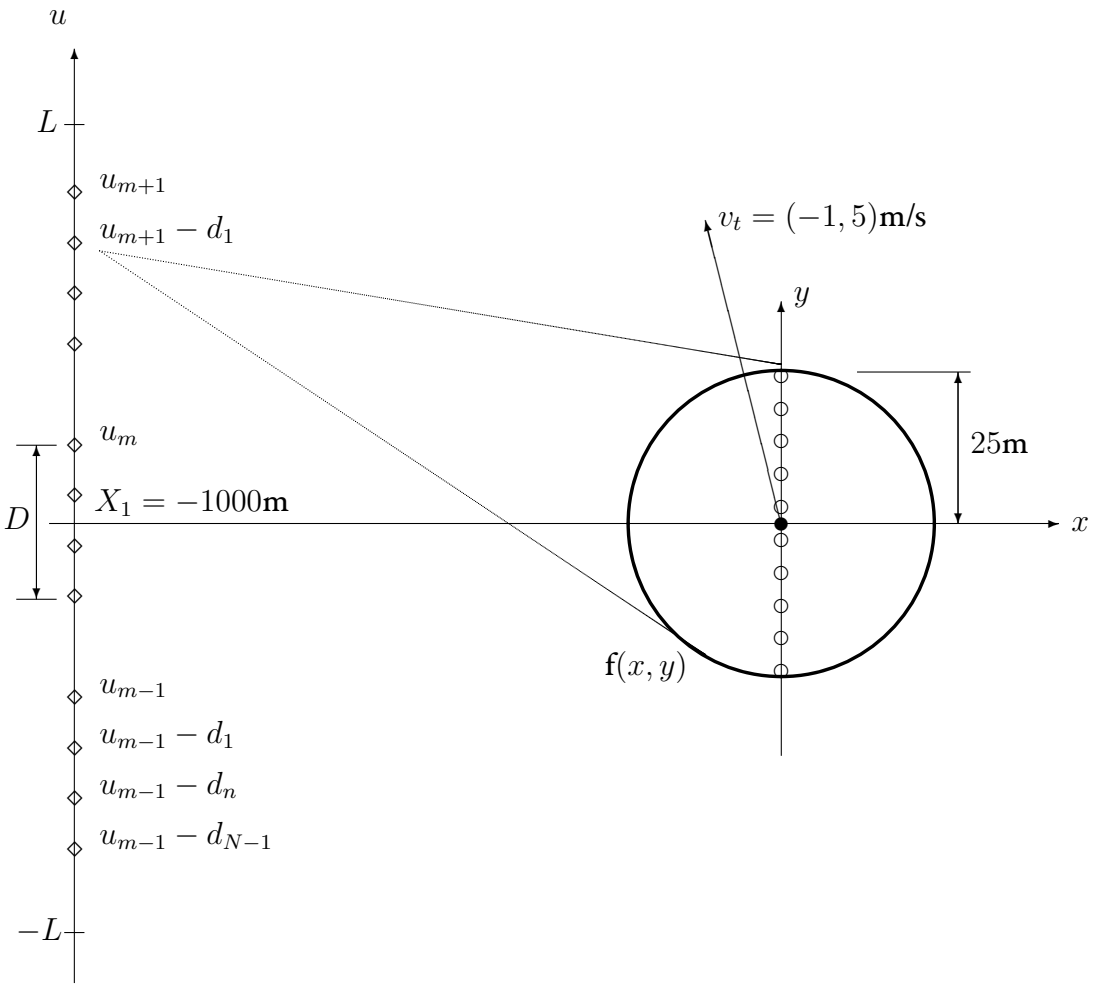

Figure 3.6: A schematic layout of the simulation scenario. Please note that $D > L$ in example 1.

since the plots are made for equal number of samples in Doppler and angular frequencies, the moving target is shifted along the main diagonal of the lower plot. The velocity and azimuth axis were scaled to fit the imaged area and velocity range. Similar behaviour can be observed in the upper plot, but the exact expression for this shift could not be found. Also note that the moving target is slightly defocused due to its along-track velocity component v_y. However, the most important thing to be observed here is that the moving target is shifted in the horizontal direction and thus separable from the stationary targets in the angular (velocity) domain. Its velocity component v_x could be in principle extracted using this horizontal shift, but this can be done more accurately in azimuth-range domain, once the moving target is isolated.

Stationary and moving target models from equation (3.4) and from equation (3.27), respectively, were used. High numbers of samples and large apertures are necessary if inversions (3.12) and (3.40) are to be applied directly. This leads to rather impractical scenarios such as the one in this example. The following examples introduce somewhat more realistic parameters with modified processing.

3.6.2 Example 2

The next example uses the following set of parameters:

parameter	ω_c	X_1	L	D	M	N	v_r	v_x	v_y
value	$2\pi 10^9$	-62.5	30	20	256	8	100	-1	5
units	rad/s	m	m	m	–	–	m/s	m/s	m/s

In this case, the number of sensors N is relatively small to sufficiently sample the rapidly fluctuating received signal in the spatial domain. This does not necessarily imply insufficient sampling of the focused target domain. Nevertheless, the inversion defined by equation (3.40) requires correct sampling also in the measured domain and needed to be modified. We use two important components of Fourier-based SAR processing: interpolation and spectral windowing. Note that after $S(k_u, \omega, d)$ has been transformed into $S(k_u, \omega, k_d)$, the k_d spectral domain corresponds to the sampling of *measured data*. Since k_d is essentially the Doppler domain, the moving target will be located at a frequency proportional to $2kv_x/v_r$. One can thus use interpolation to relate d domain to d' domain corresponding to *expected velocity range*. One simply computes samples required to properly sample estimated velocity range of interest and then uses interpolation to pick corresponding samples (if any) from the measured data in d domain. A window function in the spectral domain k_d is applied to reduce the artefacts caused by rounding errors, aliasing and to generally regularise the inversion. The simplest choice is a rectangular function; however, other windows such as Hamming can also be applied.

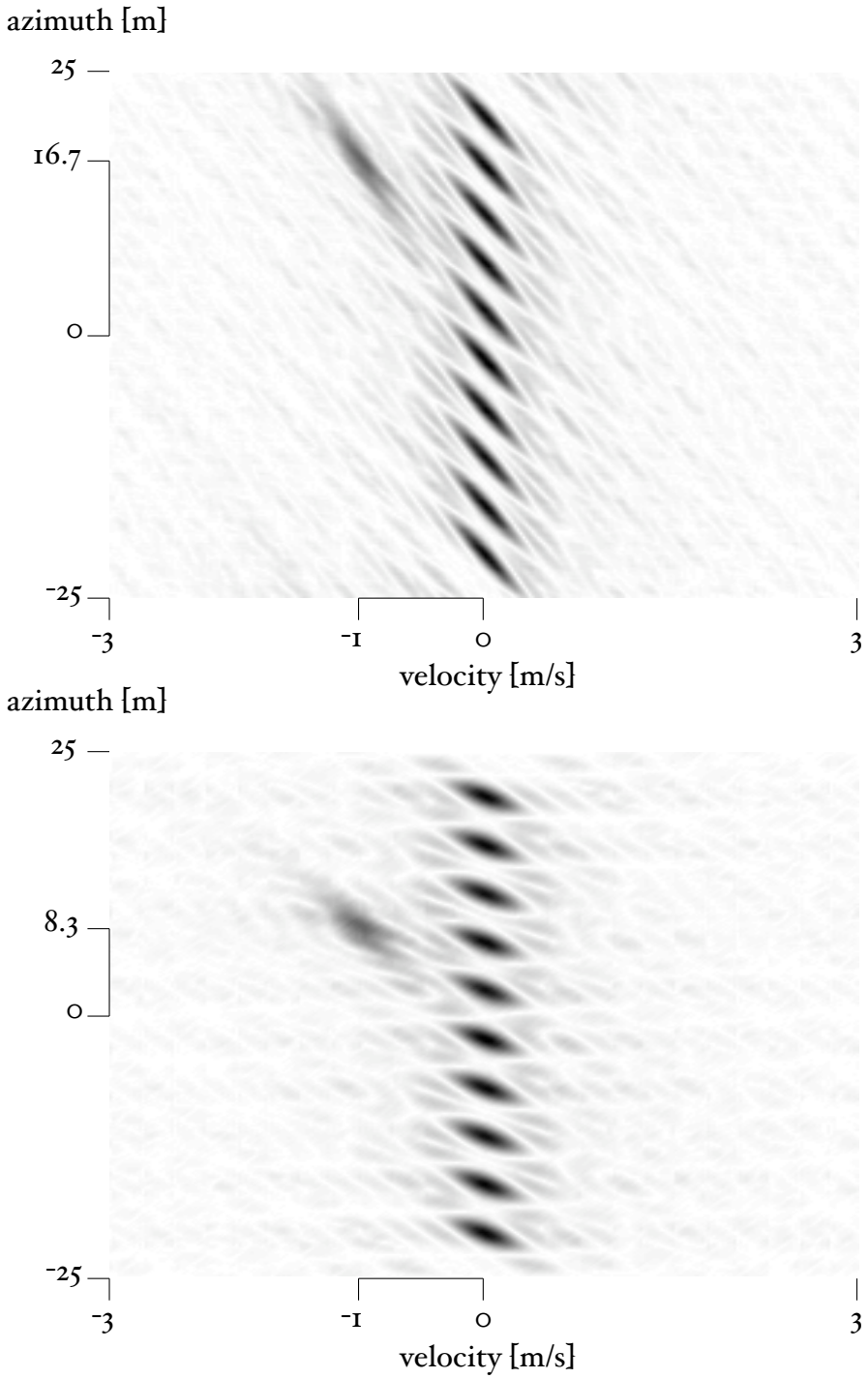

Figure 3.7: Full inversion according to Section 3.2 (top), SAR-based inversion according to Section 3.5 (bottom).

Thus, the modified focusing scheme can be formulated as follows

$$g(x'_n, y'_n, k_v) = \tag{3.41}$$
$$\mathcal{F}^{-1}_{(k_u,k)}\mathcal{F}_{(d)}\left\{W(d)\exp\left[\jmath X_1\sqrt{4k^2-k_u^2}+\jmath\left(Y_1+\frac{d}{2}\right)k_u\right]\exp\left(\jmath\frac{kd^2}{4x}\right)S(k_u,\omega,d)\right\},$$

where

$$k_v \equiv k_d \approx 2k\frac{v_x}{v_r} \tag{3.42}$$

and

$$W(d) = \begin{cases} 1, & \text{if} \quad d < |D'/2| \\ 0, & \text{otherwise.} \end{cases} \tag{3.43}$$

Constant D' denotes support $[-D'/2, D'/2]$ that can be larger than the support $[-D/2, D/2]$ of the measured data domain d. From the Discrete Fourier Transform equations, we find that

$$\Delta d' = \frac{\pi v_r}{2kv_{xmax}}, \tag{3.44}$$

where d' is the re-sampled domain d and v_{xmax} is the maximum expected target v_x velocity.

Figure 3.8 schematically shows the procedure. The resulting focused target domain is shown in figure 3.9. The moving target is still distinguishable. Strong influence by the windowing function is noticeable from the changed shape of the side lobes as well as their elevated levels, which are now dictated by the shape of function $W(d)$ rather than the original point spread function. This explains why the defocusing is not as significant as in the previous example. It is noticeable only in the strength of the target signature when compared to the stationary ones. The moving target is only slightly shifted in azimuth, since the shift given by equation (3.33) depends also on X_1, which is now relatively small.

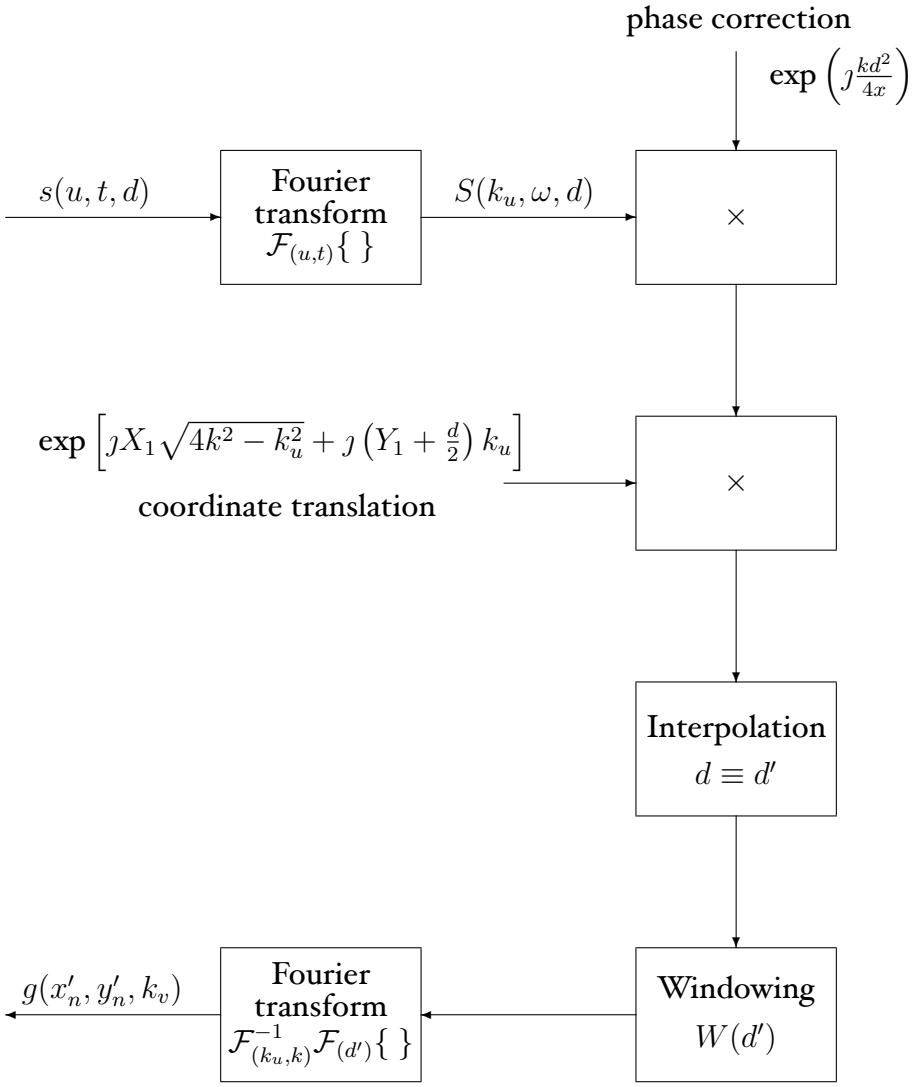

Figure 3.8: Schematic depiction of the algorithm from example 2.

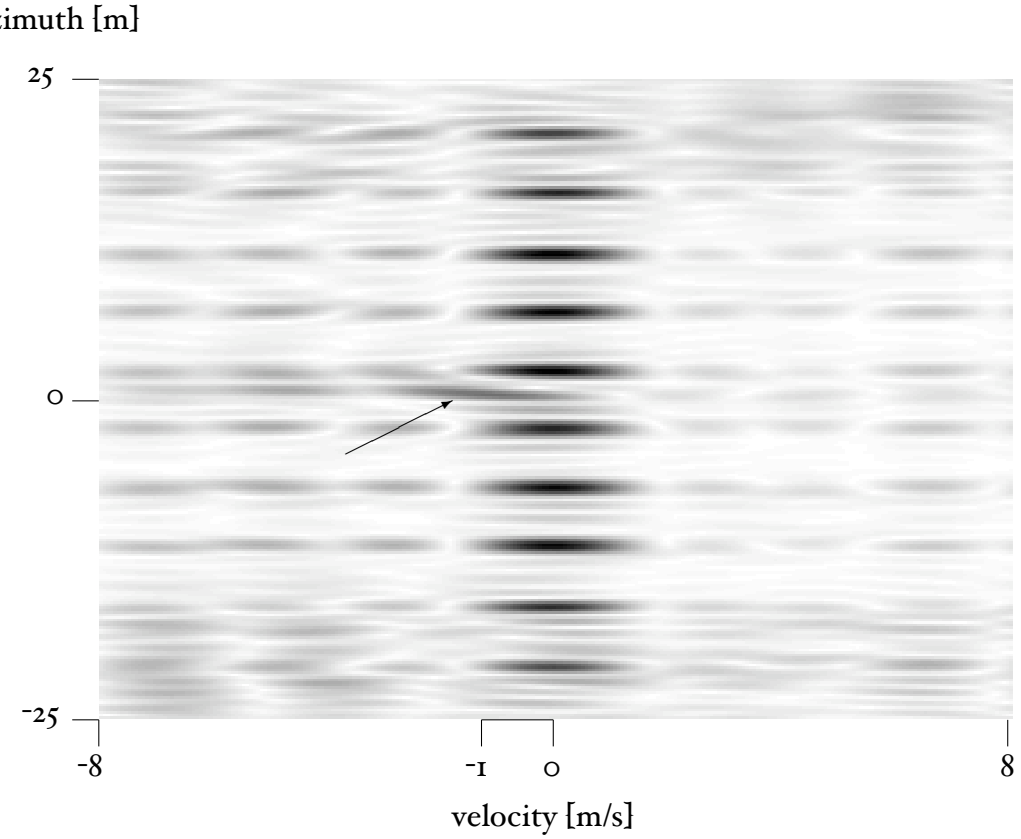

Figure 3.9: Simulation result from example 2. Moving target is indicated by the arrow.

3.6.3 Example 3

It can be deduced from the previous example and from the mathematical description itself that if the aperture length D is decreased even further, the phase measured along the dimension d will be almost linear and the term $\exp(jkd^2/(4x))$ will not make any significant difference on the processing. The inversion algorithms presented in this paragraph, however, use a nonlinear phase behaviour to obtain better resolution. If this advantage is lost, it makes no longer sense to apply the model inversions presented here. Instead, an approximation can be assumed. Namely, the Fresnel's approximation of a planar wave impinging on an antenna array is applied and the focused domain v_x is obtained by directly mapping it into the k_{vx} domain, i.e.

$$v_x \equiv k_{vx} \tag{3.45}$$

This example represents a case in which even a smaller antenna array is used. One is not necessarily interested in a possibility to accurately visualise the moving targets

in the velocity domain; the objective is simply to separate them.

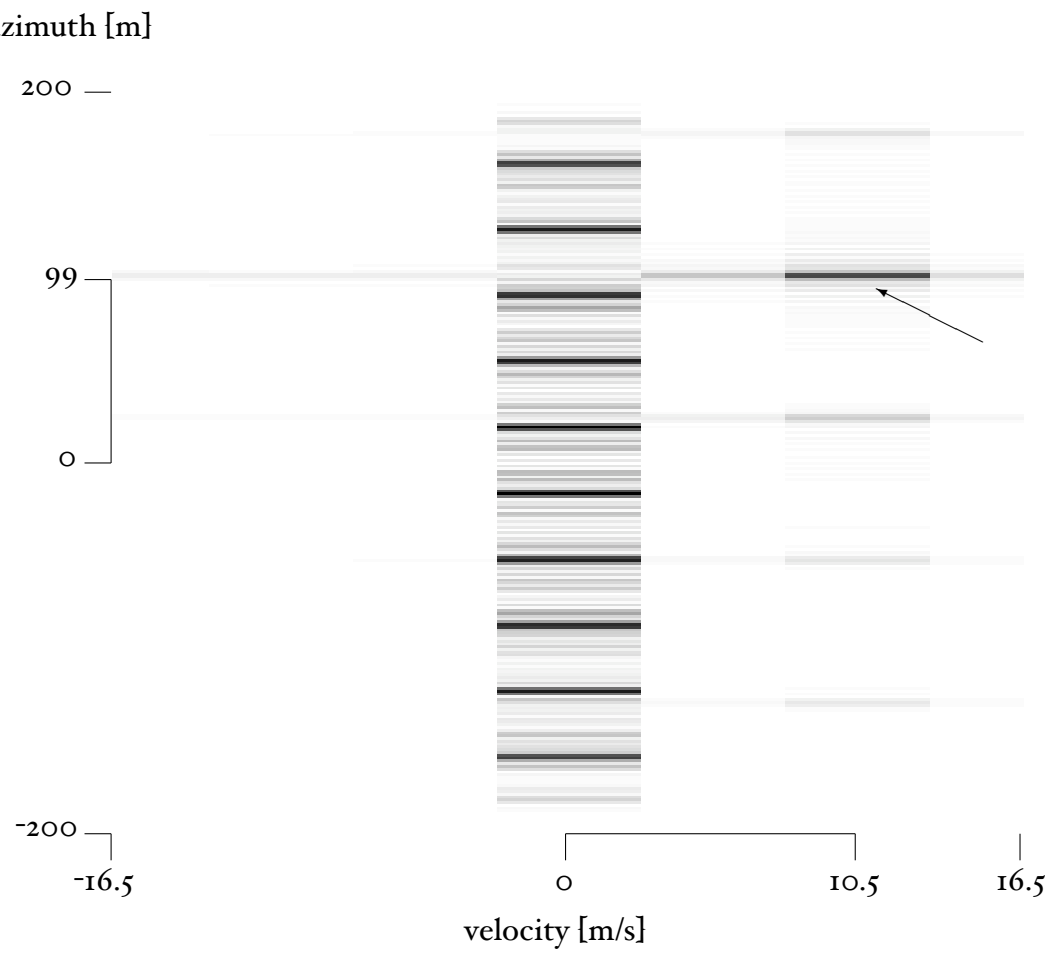

Figure 3.10: Simulation result from example 3. Moving target is indicated by the arrow.

The parameters of such a scenario could be as follows:

parameter	ω_c	X_1	L	D	M	N	v_r	v_x	v_y
value	$2\pi 10^9$	-1000	240	5	2048	8	100	10.5	5
units	rad/s	m	m	m	–	–	m/s	m/s	m/s

Figure 3.10 shows results of the simulation. As expected, the resolution in the velocity domain deteriorated due to the small size of the antenna array D. One can anticipate that with a further decrease of D, the FFT-based spectral analysis will not be sufficient for moving targets extraction. The next chapter will consider such scenario and use the *principal components analysis* (PCA) as the main tool.

This example links our approach to some practical radar systems currently in use. In fact, experimental results from a real case study of the application to an ultra-wideband radar for detection of human victims buried underground during natural disasters will be provided in Chapter 5. Nevertheless, one should not expect such a solution to resolve all issues connected with a SAR-MTI using small-size antenna arrays. Namely, the *blind angle* ambiguity is an important problem [35, Chapter 5]. It is noted here that for a good resolution in the velocity domain, at least a sufficient number of antenna elements to perform an FFT is essential to resolve all ambiguities. This argument is a subject to ongoing research and its outcome largely depends on current developments in radar hardware, which are beyond the scope of this thesis.

3.7 Concluding remarks

Section 3.2 introduced a general inversion for stationary targets. Section 3.3 analysed an inversion for moving targets. However, only an approximate solution was found when compared to the solution from the first section. This is due to a considerably increased complexity of the inverse problem in case of moving targets. In Section 3.4, we proceeded to approximately analyse an extraction of moving targets from data containing stationary targets as well. That section showed how moving targets could be extracted when inversion for stationary targets is applied to moving targets data: the central idea of this chapter. Section 3.5 studied a relation of the proposed inversion to SAR processing. Theoretical results were numerically verified in the previous section. It could be concluded that the generalised inversion is interesting only from the theoretical point of view and the SAR-based inversion will suffice for all practical purposes.

The models and algorithms discussed in this chapter make use of the fact that at close ranges, the phase of the wave impinging on an antenna array ceases to be linear or even quadratic. Current airborne MTI radars operate at much longer distances and have much coarser spatial resolution then the models studied in this chapter. For this reason, no advantage would be gained by applying the inversions presented here. One can formulate a simplified model of the problem and seek a processing algorithm that would require less computations at the expense of some loss of spatial resolution. Nevertheless, it is desirable to keep a good sensitivity in velocity domain. We have seen from numerical examples that such requirement will not be met in case of small antenna arrays, unless other algorithm than the FFT is used. Next chapter presents a suitable solution for practical airborne MTI radars by applying principal component analysis to SAR-MTI.

There were no fewer than four radar screens, as well as a prominent vertical panel carrying three large meters. One was labeled ELEVATION, another AZIMUTH, the third RANGE. It needed no great intelligence to deduce that this was where the controller sat, and that these meters told him what was happening to the aircraft he was talking down.

Arthur C. Clarke, *Glide Path*

Chapter 4

Special Approach to Multi-Channel MTI

This chapter has several objectives: The first one is to study a simplified multi-channel model for airborne SAR-MTI. Unlike in the general approach, the approximate methods described in this chapter cope better with scenarios applicable to current airborne MTI. Section 4.1 presents a relevant model. The next objective is to show a relation of our model to a standard STAP model. This is attempted in Section 4.2, where the relation of the simplified SAR-MTI model to current STAP models is analytically established. In Section 4.3, the PCA-based method of Kirsteins and Tufts [23] is used to extract moving targets even if there are not enough sensors to focus them in velocity domain. First, a special case of well calibrated sensors is shown, which reduces to averaging in the angle domain. Then, the PCA approach is discussed. It is shown that the problem of moving targets' extraction can be de facto treated as a one-dimensional spectral filtering. The separation is independent of a moving or stationary targets' distribution. Thus, a covariance estimation from measured data is not required. Some numerical experiments will be carried out in Section 4.4.

4.1 Airborne MTI model

In Section 3.3, a response of a multi-channel SAR system to a moving or stationary point target, was modeled by equations (3.27) and (3.28) as

$$s(k,u,d) = \sigma \exp\left[-\jmath k\sqrt{\kappa^2+\zeta^2} - \jmath k\sqrt{\kappa^2+(\zeta+d)^2}\right], \tag{4.1}$$

where

$$\kappa = x - v_x\tau \tag{4.2}$$
$$\zeta = y - v_y\tau - v_r\tau \tag{4.3}$$

and τ is related to u via $\tau = u/v_r$; v_r, v_x, v_y are the velocities of the radar platform and the target, respectively; x, y indicate target position; σ is the target reflectivity. The index n is dropped for clarity.

Suppose a signal produced by a stationary, unit reflectivity point target located at coordinates $(X_1, 0)$. By substituting these coordinates with reflectivity for x, y and σ in equation (4.1) and applying derivations given in Appendix B one gets

$$s_0(k, u, d) \approx \exp\left[-\jmath 2k\sqrt{X_1^2 + u^2 - ud + d^2/2}\right]. \tag{4.4}$$

X_1 is the perpendicular distance to the center of the area to be imaged. We call s_0 the *reference function*. It is used to convert the function in equation (4.1) to a linear function of coordinates and cross-track velocity. To achieve this, so-called *digital focusing* [35, 37] will be applied

$$s_c(k, u, d) = s(k, u, d)s_0(k, u, d)^*, \tag{4.5}$$

where * denotes complex conjugation. After evaluating this expression one gets

$$s_c(k, u, d) \approx \sigma \exp\left\{-2\jmath k\left[x - X_1 + \frac{y}{X_1}\left(\frac{d}{2} - u\right) - uv_a\right]\right\}. \tag{4.6}$$

x, y are the spatial coordinates with the origin at the center of the area. $v_a = v_x/v_r$ is a ratio of the radial velocity to the velocity of radar platform. A detailed derivation of this expression is given in Appendix B.

We have neglected v_y here, since we have seen in Chapter 3 that along-track velocity v_y only introduces defocusing; not a shift in the velocity domain. Therefore, a moving target with $v_x = 0$ cannot be separated from clutter in this domain.

In contrast with the case of equation (4.1), the phase function in equation (4.6) is linear with respect to x, y, and v_x. This means that the three-dimensional Fourier transform will now produce focused points in the domain of interest, that is (x, y, v_x). Thus, an approximate solution to the inversion of the model defined by equation (4.1) is found.

It is useful to observe that for $|\alpha u| \ll R$

$$\sqrt{X^2 + (Y - \alpha u)^2} \approx R - \frac{\alpha u \sin\phi}{R}, \tag{4.7}$$

where $\sin\phi = Y/R$, $R = \sqrt{X^2 + Y^2}$ and X, Y, α are defined as in equations (3.30). This means that expression (4.1) will be already roughly linear with respect to u and d for small synthetic apertures L compared to the distance X_1 (basically, the approximation neglects quadratic terms u^2 and d^2 with respect to the rest of the terms under the square root). In such case, the digital focusing using equation (4.5) will not be necessary. This approximation is used later on to process MCARM and SOSTAR data in Chapter (5).

The following paragraphs will deal with the design of efficient algorithms to separate stationary and moving targets at various circumstances. At this point, we shall define *clutter* as all stationary targets' signatures present in MTI radar data. A "clutter-rejecting algorithm" will, in this thesis, not only represent an algorithm capable of discarding such signatures, but rather in a broader sense a *classifier* capable of a separation of stationary and moving targets into two classes.

It has been already mentioned in Chapter 3 that range compressed data are assumed. Analysis provided there showed that, unlike stationary targets, moving targets will be shifted in the direction of the k_d axis proportionally to their velocities. Although the moving targets' positions will also change in the direction of the k axis or range, this change is difficult to be exploited because the (k_u, k) domain is also occupied by stationary targets. Hence, it makes sense to design a clutter-rejecting algorithm in the (k_u, k_d) domain, thus working independently of the k domain. This means, a two-dimensional model can be considered

$$s(u,d) \approx \sum_{i=1}^{M_i} \sigma_i \exp\left[-\jmath\, a_i(d/2-u) + \jmath\, b_i u\right], \tag{4.8}$$

where $i \in \mathbb{N}, \sigma \in \mathbb{C}$ and $a, b \in \mathbb{R}$. Formally, the model given by equation (4.8) corresponds to equation (4.4) as follows: Constants $2k, X_1$ and the variable x have been removed, since we are trying to design a clutter rejecting algorithm that is independent of range. Thus, $a_i \approx y_i$ is an azimuth position of a target, $b_i = v_{ai}$ is its relative speed. The objective is to divide this function into two functions s_a and s_b, i.e.

$$s(u,d) = s_a(u,d) + s_b(u,d), \tag{4.9}$$

such that

$$s_a(u,d) = \sum_{k=1}^{K} \sigma_k \exp\left[-\jmath\, a_k(d/2-u)\right] \tag{4.10}$$

$$s_b(u,d) = \sum_{l=1}^{O} \sigma_l \exp\left[-\jmath\, a_l(d/2-u) + \jmath\, b_l u\right] \tag{4.11}$$

$$M_i = K + O \qquad k, l \in \mathbb{N}. \tag{4.12}$$

We do not know the values of a_i and b_i. What we do know, however, is that in the 2D spectral domain (k_u, k_d), function s_a will produce peaks located on a straight line (see equation (B.17) in Appendix B)

$$S_a(k_u, k_d) = 4\pi^2\sigma(k_u)\delta(k_d + k_u/2), \tag{4.13}$$

$$k_d = -k_u/2. \tag{4.14}$$

The points on this line can be shifted in such a way that $k_d = 0$. This shift will in fact allow an application of one-dimensional MTI processing techniques. As shown in Appendix B, we multiply the Fourier transformed signal given by equation (4.6) $s_c(k_u, d)$ by a function $s_s(k_u, d)$ that aligns the individual SAR images

$$s(k_u, d) = s_c(k_u, d)s_s(k_u, d), \tag{4.15}$$

where

$$s_s(k_u, d) = \exp(\jmath\, k_u d/2). \tag{4.16}$$

This step is performed implicitly by a more general inversion algorithm introduced in Chapter 3, equation (3.40). The inversion is in turn a form of a bi-static along-track MTI algorithm presented in [36], generalized for multiple channels.

4.2 Connection to the traditional application of STAP in airborne MTI

In this section, we will restrict ourselves to one particular application of STAP: airborne MTI. The purpose is not to compare clutter-rejecting algorithms proposed here to the scores of methods proposed elsewhere. We will rather attempt to show how the signal model commonly used as a starting point in [13, 17, 28] can be derived from the model proposed here. We will do that by showing that the standard airborne MTI model for stationary targets formally corresponds to the two-dimensional Fourier transform of the function s_a defined by the equation (4.10). Hence, the standard airborne MTI model can be considered as a special case of the general model derived in Chapter 3. Further, the operation defined by equation (4.15) will be presented here as an additional operation performed on the conventional airborne MTI STAP model. Again, the result of this operation yields an orthogonal domain. This generally decreases the computational demands on the solution of any inverse problem [14], including airborne MTI.

For example, authors of references [13, 17, 28] define a normalised signal returned by a target as

$$u(n, l) = \exp(\jmath 2\pi\omega_i n)\exp(\jmath 2\pi\theta_i l), \tag{4.17}$$

where n, l are variables, ω_i, θ_i are normalised Doppler frequency and a normalised spatial frequency of a target i, respectively. Please note that this expression is analogous to equation (4.8) with

$$(n, l) \equiv (u, d) \tag{4.18}$$

$$2\pi\omega_i = -a/2 \tag{4.19}$$

$$2\pi\theta_i = a + b. \tag{4.20}$$

In fact, a discrete form of equation (4.17) is more often in use. In that case, variables n, l became column vectors $[1 \dots N-1]^{\mathrm{T}}, [1 \dots L-1]^{\mathrm{T}}$, respectively ($^{\mathrm{T}}$ denotes transpose). Equation (4.17) then becomes

$$\boldsymbol{u} = \boldsymbol{a} \otimes \boldsymbol{b}, \tag{4.21}$$

with $\otimes$ being the Kronecker product, or simply

$$\boldsymbol{U} = \boldsymbol{a}^{\mathrm{T}}\boldsymbol{b}, \tag{4.22}$$

which is the notation favoured here. Further, an important relationship for stationary targets is defined as:

$$\omega_i = \beta\theta_i \tag{4.23}$$

Thus, for stationary targets, one can write

$$u(n, l) = \exp\left[\jmath 2\pi\theta_i(\beta n + l)\right] \tag{4.24}$$

We can now calculate a spectral response of the standard model for targets located at the same distance from the radar at all angles; the purpose is to show that the result is analogous to equation (4.13) and thus the constant β can be evaluated. Consider a continuous case of an infinite number of stationary targets located at all possible angles θ

$$u(n, l) = \int_{\infty}^{\infty} e^{\jmath 2\pi\theta(\beta n + l)} \mathrm{d}\theta \tag{4.25}$$

Following the procedure in Appendix B.2, the two-dimensional Fourier transform of this expression is

$$U(\theta, \omega) = 4\pi^2\delta(\theta - \omega/\beta), \tag{4.26}$$

which again shows that stationary targets will be located at a "ridge" defined by the relation $\omega = \beta\theta$.

Authors of [17, 25] refer to the (θ, ω) domain as the *angle-Doppler* domain. Since one can relate the expression above to equation (4.13), the (k_u, k_d) domain is the Doppler-angle domain. Therefore, using our notation the factor β can be defined as

$$k_u = \beta k_d \tag{4.27}$$

From equation (4.14) it follows that $\beta = -2$. Even though our consideration implies that the constant β assumes only one value, it is sometimes expressed as a variable dependent on other parameters such as D or v_r. In order to find such a relation, we note that by using equation (4.16), one can construct the two-dimensional shifting function $s_s(w_1, w_2)$ of a variable w_1 defined within an interval $[-\pi M/2, \pi M/2]$, a variable w_2 defined within an interval $[-N, N]$, and a constant

$$\gamma = \frac{D}{N4L}, \tag{4.28}$$

so that

$$s_s(w_1, w_2) = \exp(\jmath\gamma w_1 w_2). \tag{4.29}$$

This function is identical to the function defined by equation (4.16). We have simply scaled its argument such that $\gamma w_1 w_2 = k_u d/2$. Using $D/N = \Delta d$, $2L = M\Delta u$, and $\Delta u = v_r \Delta\tau$, one can further express γ as

$$\gamma = \frac{\Delta d}{2 v_r T_p}, \tag{4.30}$$

where T_p is the pulse repetition interval, M is the number of azimuth samples and N is the number of sensors. This is a reciprocal value of the constant β, as defined in references [13,17,28]. One can now see that since the support of w_1 can be chosen arbitrarily ([13, proposition 1]), many expressions for β can be found – as long as the relation between supports of w_1 and w_2 is kept such that the relation $k_{w_2} = -k_{w_1}/2$ is satisfied. Constants γ or β are only useful in cases where the ratio L/D is not known and needs to be guessed. It is a simple process of trying to align the stationary targets in vertical position in the (k_u, k_d) domain (see results with measured data in Chapter 5) by substituting a suitable number for γ or β. This does not affect the slope of the line of stationary targets, which is known and can be corrected for by effectively setting $\beta = 0$.

4.3 Multi-channel SAR MTI

The dependency of $k_u = \beta k_d$ means that a signature of any target, moving or stationary, will occupy a two-dimensional domain (k_u, k_d). This makes MTI difficult, because one needs to identify the line of stationary targets first by means of some two-dimensional spectral estimator and then detect moving targets placed off that line. However, since the dependency is known as well as the fact that the stationary targets will be concentrated in one line (and therefore in one dimension) in the (k_u, k_d) domain, one can shift the entire domain as depicted in figure 4.1 using equation (4.15). Dashed line depicts stationary targets together with a moving target

focused in angle-Doppler domain of the original data. The stationary targets are aligned on the main diagonal. The moving target is located off that diagonal. Targets shifted by the function s_s are shapes filled in black. The following convention for the *shifted* targets will be used in this section: the stationary targets are always located on a horizontal line at frequency $k_{d,0}$ which can in principle have a nonzero value. In the k_u domain, a k^{th} stationary target will be located at frequency $k_{u,k}$. An l^{th} moving target will be located at frequencies $(k_{d,l}, k_{u,l})$. We distinguish between $(k_{d,0}, k_{u,k})$, the position of a stationary target, and (k_{d_0}, k_{u_m}), the discrete sample pair in the angle-Doppler domain, since the number of stationary or moving targets can be larger than the number of discrete frequencies at which the angle-Doppler domain is sampled.

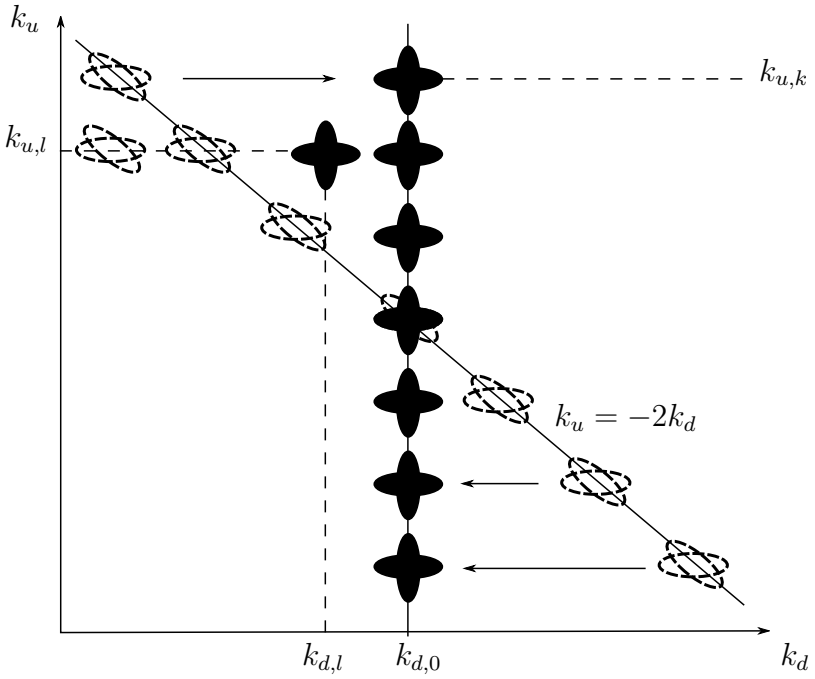

Figure 4.1: Schematic description of the shifting operation: The (k_u, k_d) domain before and after applying function $s_s(k_u, d)$.

After the shift, the model of a multi-channel SAR MTI signal can be expressed in the form of

$$\sum_k A_k \exp\left[-\jmath(uk_{u,k} + dk_{d,0})\right] = f(u) \cdot h(d) \tag{4.31}$$

where

$$f(u) = \sum_k A_k \exp\left(-\jmath u k_{u,k}\right) \tag{4.32}$$

$$h(d) = \exp\left(-\jmath d k_{d,0}\right) \tag{4.33}$$

and

$$k_{u,k} \in [-K_u, K_u], \qquad K_u = \text{const.}$$

Thus, axes k_u, k_d now represent target's azimuth position a and velocity v_a ***independently***. Also, one can observe that for velocity estimation, only a one-dimensional spectrum estimation is now needed.

The idea to use some transformation in order to simplify the MTI processing is not new. A target velocity-dependent transform in the angle-Doppler domain was proposed in reference [10], as well as in reference [27]. However, the transform defined by equation (4.15) does not depend on target's velocity as it does in the latter work. We have seen that the relation described here is a consequence of the problem geometry and it is, in this sense, optimal; there is not a better transform that would reduce the problem dimensionality even further.

The claim of one-dimensional processing being possible is supported by the fact that, after the data shift, the angle-Doppler domain data matrix is analogous to data from stationary time-varying sources located at different angles (see reference [6], for instance). The azimuth axis can now be treated as "time". Clutter is located at the zero angle, moving targets have nonzero bearings. Azimuth processing constitutes "demodulation" or spectral estimation in the transformed "time" domain of a signal received by each sensor. We can see from this analogy that the parameters of the beamformer will not change in time – as long as the amplification of each antenna sensor does not vary with time. The weights of the beamformer can be estimated from data. Since the zero-angle is being separated, the beamformer will correspond to a high-pass or a low-pass filter, depending on whether stationary or moving targets are being suppressed. This idea was exploited in [10] for a practical design of such a beamformer. However, we consider the mathematical approach presented here slightly more direct.

4.3.1 Target separation using averaging

The sampled version of expression (4.31) can be decomposed into the column vector $f(\boldsymbol{u})$ and the row vector $h(\boldsymbol{d})$. Hence,

$$\boldsymbol{S} = \boldsymbol{f}\boldsymbol{h} \tag{4.34}$$

Suppose we know $\boldsymbol{S}$ and $k_{d,0}$ and we are trying to estimate A_i and $k_{u,i}$. Equation (4.34) implies that

$$\hat{\boldsymbol{f}} = \boldsymbol{S}\boldsymbol{h}^{\dagger} \tag{4.35}$$

$\hat{\boldsymbol{f}}$ is an estimate of $\boldsymbol{f}$ and † denotes pseudo inverse. This solution is called *Wiener filter*. It is also called the least squares solution to an inverse problem by matrix inversion [33, Chapter 9]. For vectors, we have

$$\boldsymbol{h}^{\dagger} = \boldsymbol{h}'/N, \tag{4.36}$$

where $'$ denotes a conjugated transpose. N is the length of vector $\boldsymbol{h}$. In the signal processing literature, $\boldsymbol{h}'/N$ is called *matched filter*. Further, suppose that $k_{d,0} = 0$. In that case, vector $\boldsymbol{h}$ equals $[1\,1\,1\,\ldots]$. Clearly, $\hat{\boldsymbol{f}}$ can then be calculated as

$$\hat{\boldsymbol{f}} = \frac{1}{N}\sum_j \{S\}_{i,j}. \tag{4.37}$$

This means simply a calculation of an average over columns of matrix $\boldsymbol{S}$.

Now suppose that we have some other signals $\boldsymbol{S_m}$ with amplitudes B_l at unknown frequencies $(k_{u,l}, k_{d,l})$ but $k_{d,l} \neq k_{d,0}$ (see figure 4.1). These signals represent moving targets and will be added to the signal from expression (4.34)

$$\boldsymbol{Z} = \boldsymbol{S} + \boldsymbol{S_m} \tag{4.38}$$

One can then estimate signals $\boldsymbol{S_m}$ as follows:

$$\widehat{\boldsymbol{S_m}} = \boldsymbol{Z} - \frac{1}{N}(\boldsymbol{Z}\cdot\boldsymbol{h'})\boldsymbol{h} \tag{4.39}$$

4.3.2 PCA-based target separation

As shown in Section 2.4, by computing the *singular value decomposition* (SVD) of matrix $\boldsymbol{Z}$, one obtains several singular values. Under certain conditions, their number indicates the number of moving objects plus the biggest singular value, responsible for the entire clutter region. By removing the biggest singular value, clutter is removed also. The restriction is that moving targets should be much weaker than clutter. Similar algorithm has been studied before by authors of [23] and the trade-off between the strength of clutter compared to moving targets is treated ibidem. The general problem at hand is also called the *principal components analysis*, (PCA). An excellent overview of PCA can be found in reference [39].

Recall expression (4.34). Note that the decomposition into two singular vectors can be achieved by SVD. One can write that

$$\boldsymbol{S} = \boldsymbol{U}_a\boldsymbol{\Sigma}_a\boldsymbol{V}_a', \tag{4.40}$$

where

$$\begin{aligned}
\boldsymbol{U}_a &= \begin{bmatrix}\exp(-\jmath\boldsymbol{u}k_u) & 0 & \ldots\end{bmatrix}\\
\boldsymbol{\Sigma}_a &= \mathrm{diag}(\lambda_1, 0\ldots)\\
\boldsymbol{V}_a &= \begin{bmatrix}\exp(\jmath\boldsymbol{d}k_d) & 0 & \ldots\end{bmatrix}\\
\lambda_1 &= \sum_k A_k
\end{aligned}$$

Similarly, one can decompose matrix $\boldsymbol{Z}$ as

$$\boldsymbol{Z} = \boldsymbol{U}_b \boldsymbol{\Sigma}_b \boldsymbol{V}_b', \tag{4.41}$$

where

$$\begin{aligned} \boldsymbol{U}_b &= \big[f_1(\boldsymbol{u}), \ldots, f_N(\boldsymbol{u})\big] \\ \boldsymbol{\Sigma}_b &= \mathrm{diag}(\lambda_1, \ldots, \lambda_N) \\ \boldsymbol{V}_b &= \big[h_1(-\boldsymbol{d}), \ldots, h_N(-\boldsymbol{d})\big] \end{aligned}$$

The decomposed matrices in equations (4.40) and (4.41) are only equal in case [23]

$$\sum_{k=1}^{K} A_k \gg \sum_{n=2}^{N} \lambda_n \tag{4.42}$$

while in general the following condition is satisfied

$$\sum_{n=2}^{N} \lambda_n = \sum_{l=1}^{O} B_l. \tag{4.43}$$

Meaning that in special cases, the condition holds

$$\lambda_n = B_l. \tag{4.44}$$

Clutter rejection can be achieved by setting $\lambda_1 = 0$ and recalculating matrix $\boldsymbol{Z}$ using equation (4.41), for example. There are many solutions to the singular value decomposition of the matrix $\boldsymbol{Z}$ – the method is *ambiguous*. The reason is that SVD performs a so-called *orthogonalisation*. This means it finds signals which are *uncorrelated* [39, Chapter 10], in stricter sense *signal independence*. A potentially more powerful method would then be ICA – the *independent component analysis* [39]. In spite of this, equation (4.42) implies that the amplitudes of clutter signals must be significantly bigger than amplitudes of moving targets' signals. This is precisely the case of our interest, meaning that PCA will then provide satisfactory results.

Once the signal has been separated into components, one can set their corresponding amplitudes (singular values in case of the PCA) to zero, thus removing some parts of the data. One can use this technique to extract white noise from the data, thus perform so-called *de-noising*. Consider figure 4.2. Unlike shifted data (singular values depicted as •), unshifted data (singular values depicted as ○) produce mixtures of signals, with the result that clutter cannot be easily separated from moving objects. Also note that there is no clear distinction between noise and useful

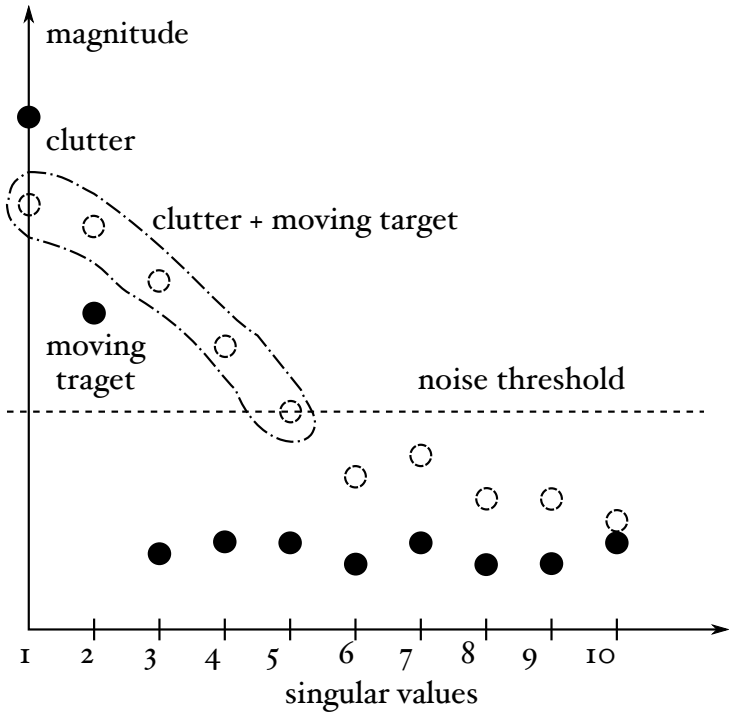

Figure 4.2: A possible SVD decomposition of the data from figure 4.1.

signals in the unshifted domain (Gaussian noise theoretically exhibits a flat plateau, as seen in the shifted case). It can be shown that singular values of a white (Gaussian) noise matrix will have the same values, forming a horizontal line in the plot, provided that the useful signal occupies only some smaller subspace [1]. Depending on the signal-to-noise ratio (SNR), a threshold can be defined above this line and all values below it are set to zero. Unlike the clutter rejection proposed above, this operation depends on SNR. However, it can considerably improve data quality. One can observe from figure 4.2 that a horizontal line representing noise is much harder to be found in the case of unshifted data.

4.3.3 Channel mismatch

The angle-independent channel mismatch model described in reference [17, Section 4.2.1] will be reviewed in this subsection. Instead of the original discrete formulation, a continuous version will be used here.

In practice, every channel in the phased array will have slightly different gain and phase shift given by the manufacturing tolerances or other construction-related factors. We suppose that each channel n has a complex gain $e(d_n)$ slightly different from a mean gain $\overline{e(d_n)}$. These discrete gains can be considered as samples of a

continuous function $e(d)$, which is generally unknown. This function will modulate function $h(d)$

$$s_a(u,d) \equiv f(u)h(d)e(d) \tag{4.45}$$

In such a case, the solution presented in subsection 4.3.1 will fail to perform correct factorization for the unknown $e(d)$. However, this is not true for PCA. Indeed, using the same procedure as in the Appendix B.2, one can write

$$\hat{s}_a(k_u,d) = 2\pi\sigma(k_u)e(d)\exp(-\jmath\, k_u d/2), \tag{4.46}$$

and

$$S_c(k_u,k_d) = 2\pi \int_{-\infty}^{\infty} \sigma(k_u)e(d)\exp(-\jmath\, k_d d)\,\mathrm{d}d, \tag{4.47}$$

$$S_c(k_u,k_d) = 4\pi^2\sigma(k_u)\left(\delta(k_d) * E(k_d)\right), \tag{4.48}$$

$$S_c(k_u,k_d) = 4\pi^2\sigma(k_u)E(k_d). \tag{4.49}$$

$E(k_d)$ denotes the Fourier transform of $e(d)$ and * denotes convolution. What is known about the result $r(d) = h(d) \cdot e(d)$ is that it is still a function of d only and therefore ***orthogonal*** to the function $f(u)$. So, under the conditions discussed earlier, one can still estimate functions $f(u)$ and $r(d)$ using SVD without really knowing them in advance. Furthermore, since we know $h(d)$, we could in principle estimate $e(d)$ – thus performing ***channel mismatch estimation*** using PCA.

4.4 Simulations

A three-dimensional data set has been created using the airborne MTI model given by formula (4.1). The layout of the target area and overall geometry of the simulation scenario are depicted in figure 4.3; Five stationary targets S_1 to S_5 (designated "$\circ$") are located at a distance $X_1 = -10000$ meters. Two moving targets M_1 and M_2 (designated "$\bullet$") are located on the x axis. The diameter of the imaged area is 4 km which means that the antenna beam width is about 22°. The reflectivity of all stationary targets was assumed to be equal to one. Moving targets were simulated for two cases with different values of reflectivity: i) Moving targets shown in figures 4.4, 4.5 had unit reflectivity. ii) Moving targets in figures 4.6 and 4.8 were simulated with a reflectivity ten times smaller than unity. The remaining parameters are summarised in table 4.1.

The simulated data set is first focused using the digital focusing described by equation (4.5). This operation converts three-dimensional complex chirps to complex harmonics having frequencies proportional to positions and velocities of the

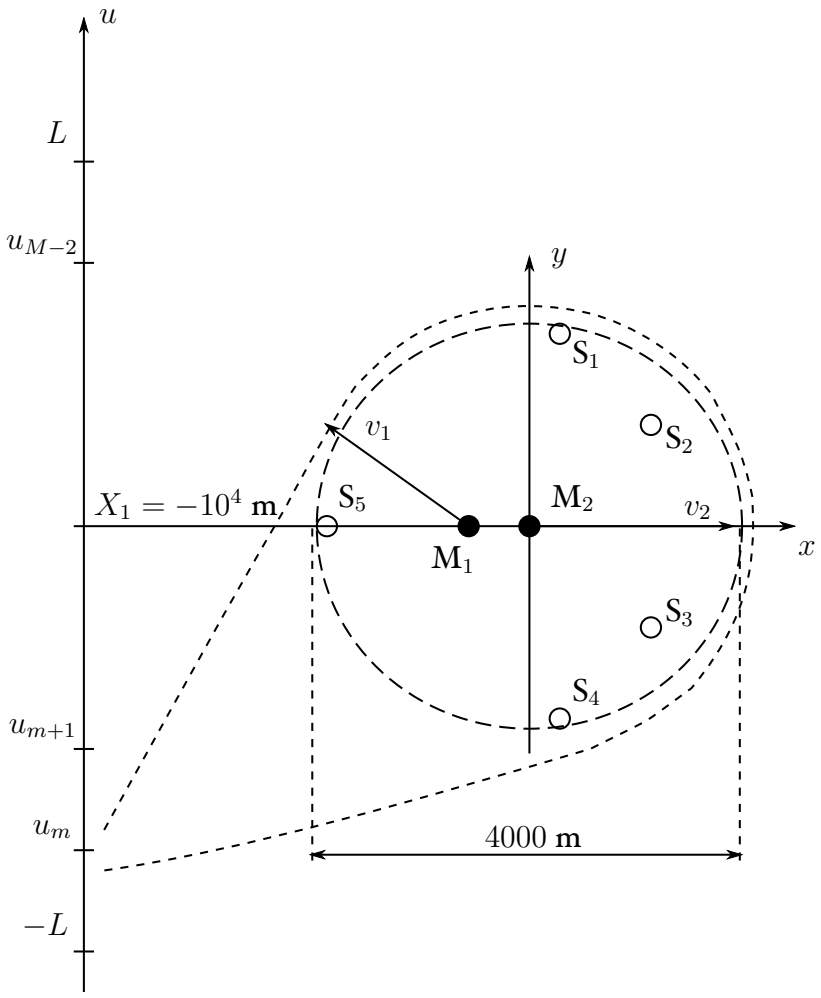

Figure 4.3: A schematic layout of the simulation scenario. Stationary targets: S_1 to S_5, moving targets: M_1 and M_2.

targets. Thus, focused points can be obtained after the application of the three-dimensional Fourier transform. However, as already shown in figure 4.1, digital focusing alone will not produce orthogonal domains; e.g. stationary targets will appear to have some velocities in the angle-Doppler (velocity-azimuth) domain. To obtain orthogonal domains corresponding to velocity, azimuth and range, it is necessary to account for the fact that the imaged scene is being viewed by different antennas at different angles. These angles can be compensated before or after digital focusing using the equation (4.15).

Table 4.1: Simulation parameters, airborne scenario

parameter	value	description
X_1	-10 km	distance to the centre of imaged area
R_1	2 km	radius of the imaged area
L	10 m	synthetic aperture length
D	5 m	phased array length
M	64	number of azimuth samples
N	16	number of sensors
P	8	number of range samples
ω_c	$2\pi \cdot 10^9$ rad/s	angular carrier frequency
v_r	100 m/s	radar velocity
v_{x1}	-7 m/s	velocity vector, $x-$component, moving target 1
v_{y1}	5 m/s	velocity vector, $y-$component, moving target 1
v_{x2}	10 m/s	velocity vector, $x-$component, moving target 2
v_{y2}	0 m/s	velocity vector, $y-$component, moving target 2

Figure 4.4 shows two plots representing magnitudes of the two-dimensional Fourier transform applied on the data in (u, d) domain. The top of the figure depicts the two-dimensional spectrum of the data after the digital focusing given by equation (4.5). The bottom of the figure depicts the two-dimensional spectrum of the data after the digital focusing and shifting using equations (4.5) and (4.15). Stationary and moving targets are labeled according to the simulation scenario depicted in figure 4.3. One can observe that in fact a two-dimensional filter is required to suppress the stationary targets in the case shown on top of figure 4.3 [17, 25, 28]. However, when the shift is employed, the stationary targets do not have any velocity component and therefore they are located on a vertical line as shown in the bottom of figure 4.4. Only a one-dimensional filter is required in this case.

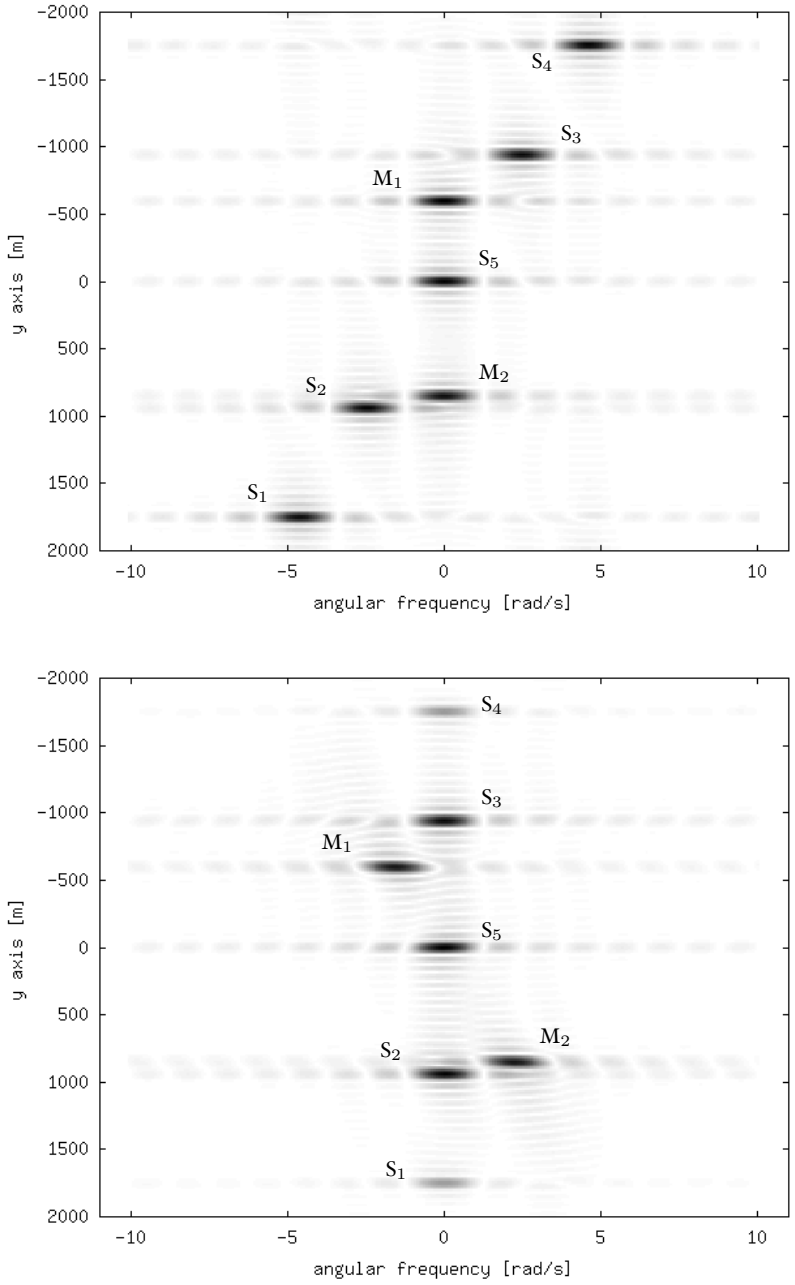

Figure 4.4: Simulation results, magnitude of a 2D-spectrum, constant range slices: (top) digital focusing applied to the data model, (bottom) digital focusing and shift applied to the data model.

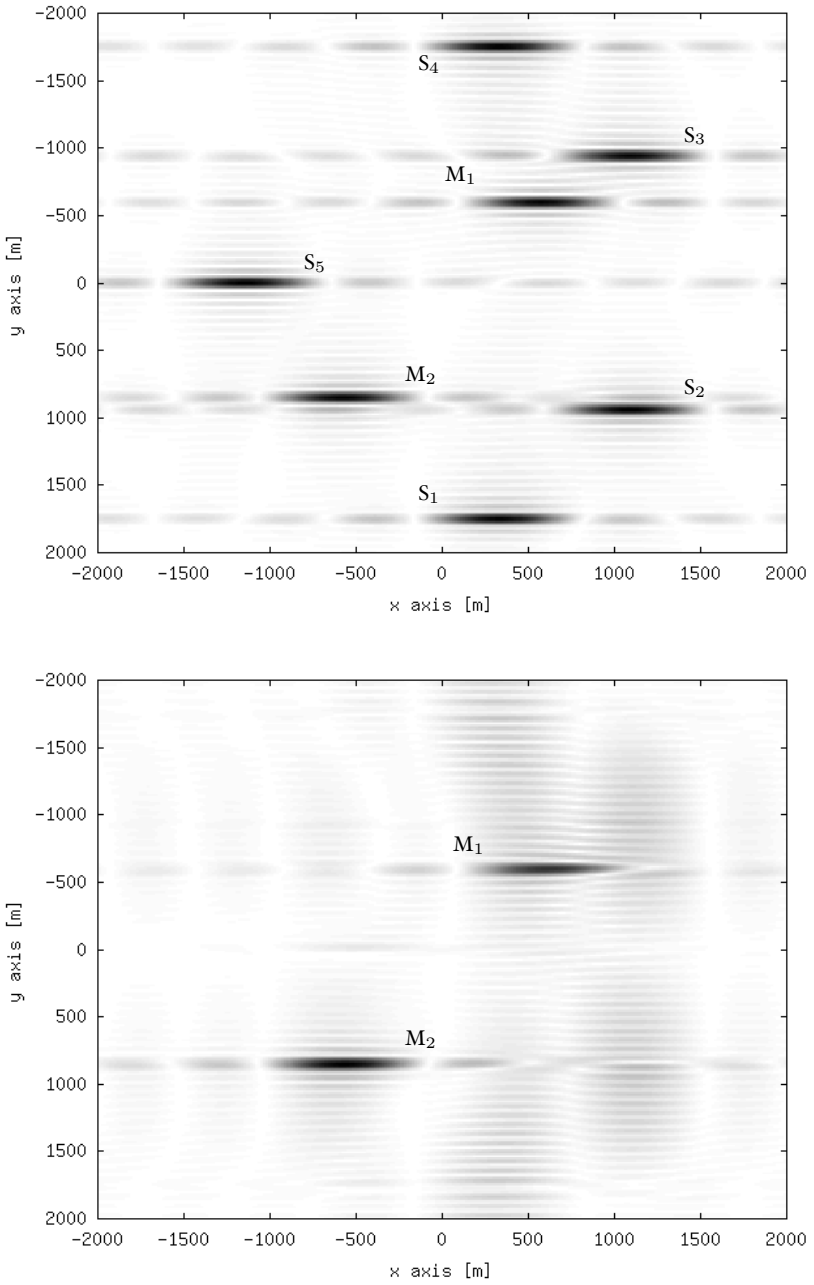

Figure 4.5: Slices of data at zero velocity: (top) SAR image with moving targets present, (bottom) SAR image of moving targets extracted using principal components analysis.

Figure 4.5 (top) shows a slice of the data cube representing a single-sensor focused SAR image. Note that the moving targets are slow enough to be fully focused. Also, their spectra are overlapping with the spectra of the stationary targets – it is the slice of the shifted three-dimensional spectral domain that is shown in the figure. Hence, the moving targets cannot be removed by single-channel based methods unless some extra measures are taken, as in reference [8]. Figure 4.5 (bottom) shows the result of PCA-based filtering. One can see that the moving targets are now extracted nearly perfectly.

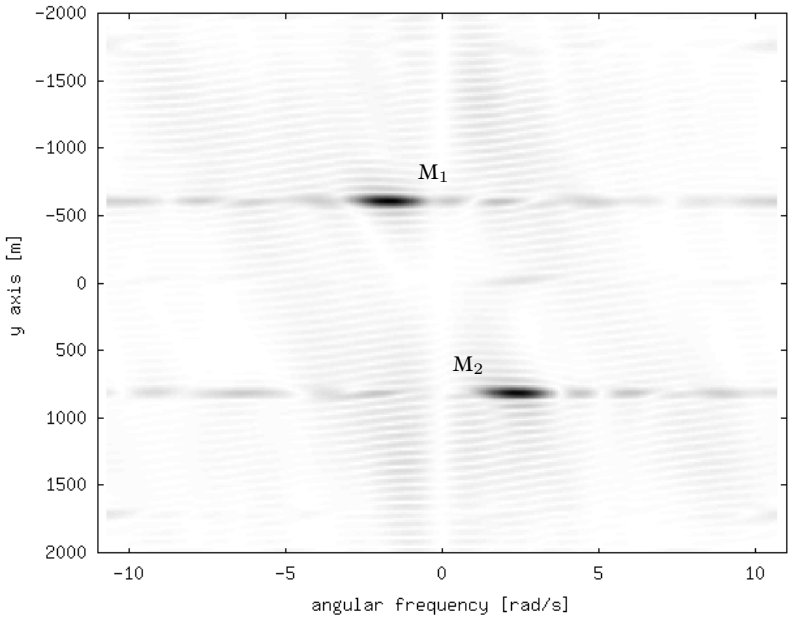

Figure 4.6: PCA with channel mismatch.

The channel mismatch influence is shown in figure 4.6. The simulation was set up as follows: Each channel was given a random complex gain, that is

$$s(d_n) = s(d_n) + \mathcal{N}_n s(d_n), \tag{4.50}$$

where $\mathcal{N}_n$ was a random Gaussian complex number with zero mean and variance equal to 10. As expected, the simulated channel mismatch changed the side lobe pattern related to moving targets (e.g. compare to the bottom of figure 4.8 where no channel mismatch was introduced), but it is interesting that for such a large mismatch, the filtration ability of the PCA-based method was not affected. This property was derived in paragraph 4.3.3 and it is generally known. The simulation results are shown here merely for completeness.

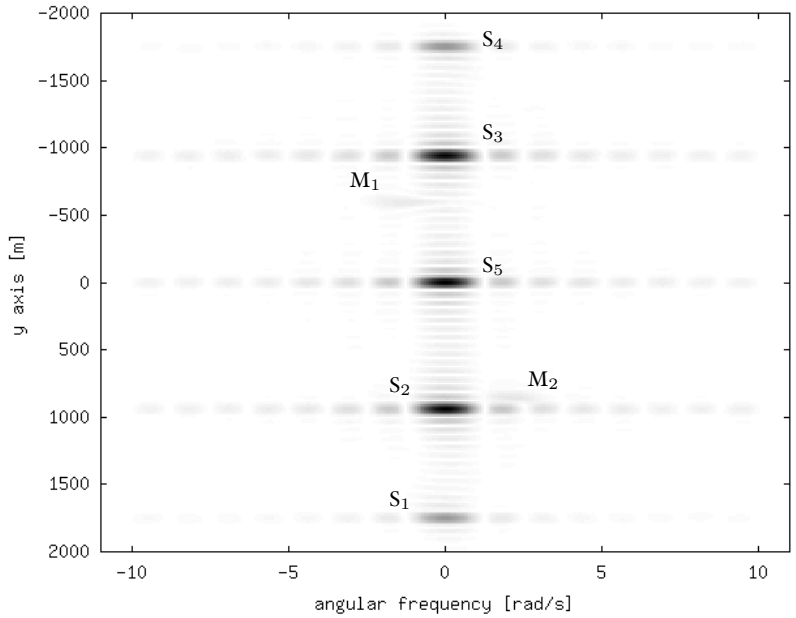

Figure 4.7: Focused azimuth-angle domain. Moving targets are ten times weaker than the stationary ones. SAR-MTI data is contaminated by Gaussian noise with zero mean and variance equal to 0.3.

The previous examples model the case where all targets have equal reflectivity. The moving targets can be clearly identified in figure 4.4 even without any attempts to remove the stationary clutter. FFT-based processing on data with a finite support produces side lobes that can mask weak targets. Using windows different than the rectangular one prior to the FFT can reduce this effect. Nevertheless, should a target be weaker than the resulting side lobes due to other targets, it will be obscured. In current airborne scenarios, it is typical that the number of stationary targets is very large, whereas the moving targets are rather sparse. It is very likely that the side lobes due to high-energy clutter will obscure weaker moving targets even if they travel at relatively high velocities. This situation is illustrated by figure 4.7. The simulation parameters are again given by table 4.1, the difference from previous examples is that the moving targets are now ten times weaker than the stationary ones. Figure 4.7 shows their focused responses to be significantly weaker than the side lobes due to the stationary targets.

In addition to decreasing the reflectivity of moving targets, noise modelled as random Gaussian complex numbers $\mathcal{N}_{m,n,p}$ of zero mean and variance equal to 0.3 was added to the signal as follows:

$$s(u_m, d_n, k_p) = s(u_m, d_n, k_p) + \mathcal{N}_{m,n,p} \tag{4.51}$$

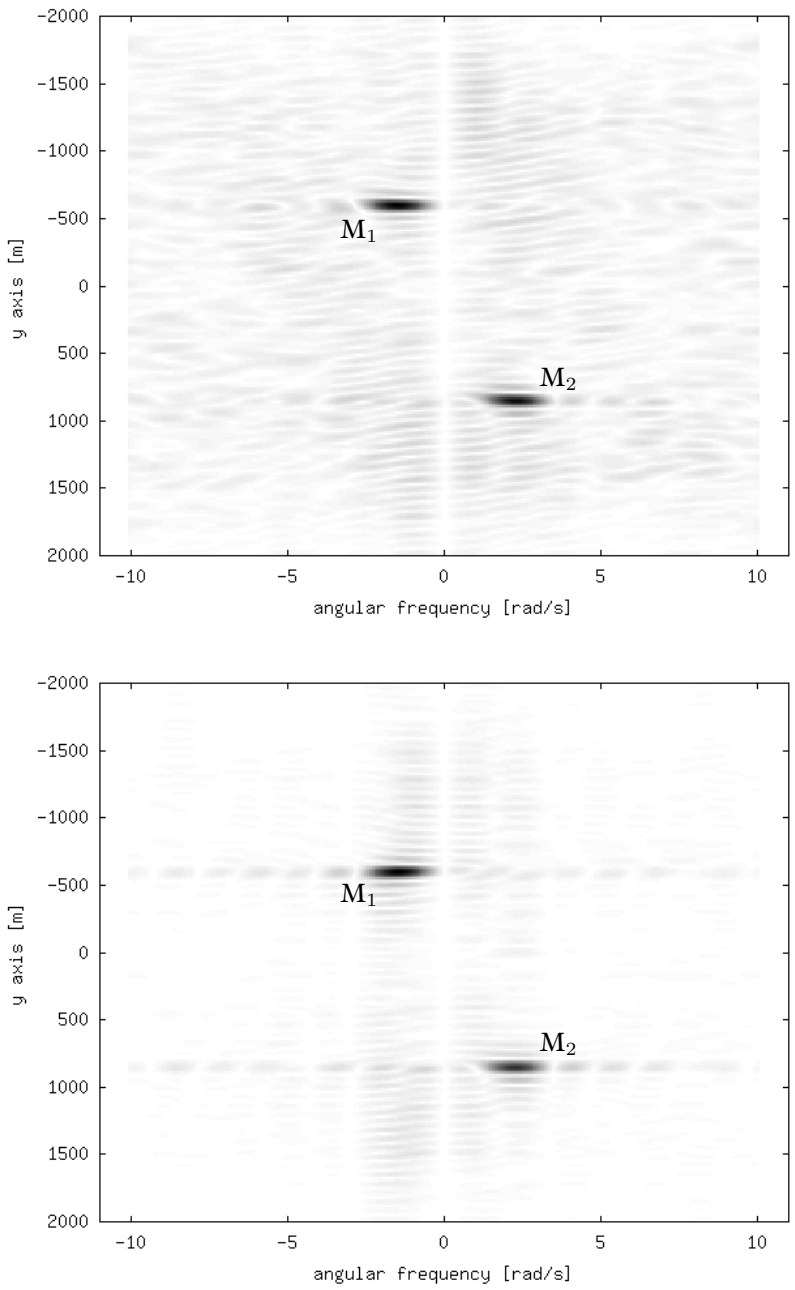

Figure 4.8: PCA-based processing of SAR-MTI data contaminated by Gaussian noise with zero mean and variance equal to 0.3: (top) the strongest singular value removed, (bottom) all except the second singular value removed.

This is not apparent in figure 4.7, since the noise floor is lower than the intensity range of the image. We applied the PCA to every range slice p of the data cube by means of decomposing the slice using the SVD, setting some of the singular values to zero and recomputing the data slice as shown in subsection 4.3.2. The results are shown in figure 4.8. The top figure shows clutter-free data after the largest singular value was set to zero. The bottom figure shows recomputed data after all except the second singular value were set to zero. This de-noising operation requires a reliable matrix rank estimation technique, which is a problem in its own right (see [23], for instance). It can be observed that the clutter filtering capability is not affected by noise. Additive noise reduces the visibility of the moving targets, but it is decoupled from the clutter signal and its distribution. This simplifies the problem of moving target detection to the known problem of a single harmonic signal in noise. This would be the lower limit. The upper limit is given by the constraint that moving targets must be weaker than clutter – a condition relatively common in real-life problems.

4.5 Concluding remarks

Simplified multi-channel model for airborne SAR-MTI has been studied in Section 4.1. We have seen that in the simplest case, focusing the airborne data in the azimuth-Doppler domain by the model inversion requires a two-dimensional spectral estimation applied directly to the data. In a more general case, a multiplication with a two-dimensional chirp-like function followed by a two-dimensional spectral estimation can be performed. This model is identical to the MSAR model treated in reference [12] and obeys the detection bounds derived ibidem. Section 4.2 showed a relation of our model to a standard STAP model. The known PCA-based algorithm by Kirsteins and Tufts was used to extract moving targets even if there are not enough sensors to focus them in velocity domain. A special case, when the averaging in angle domain can be applied was discussed. It can be concluded that only two sensors are necessary to perform averaging, or to obtain a rank-2 matrix, which allows a separation between two classes: moving targets and stationary ones. However, the blind angle problem will still persist in that case. As already mentioned in Chapter 2, SVD does not require the formation of a covariance matrix, which is typically very expensive to be computed. The approach chosen here completely circumvented such computation, saving a considerable amount of resources in the process. SVD was applied to a matrix of a size $N \times M$ in this chapter. The corresponding computational load required is $O(MN^2)$, where $M \geq N$. This can be compared to the SVD of a covariance matrix $M \times N$, which would take $O(M^3N^3)$ multiplications. Nevertheless, if averaging is possible, only division by the number of channels N is required, which can be implemented by means of a shift register

in digital hardware. In this case, no multiplications are required to perform STAP. Thus, averaging constitutes the simplest and the least expensive STAP algorithm discussed in this thesis.

And therefore in the whole work it is perceived Who the Maker is.

Hildegard of Bingen, *Liber Scivias, II, Vision 2*

When there was an E, I played on E. When there was a G, I played on G. And when there was no bow, I even played with a twig rubbed with rosin...

Dušan Holý (ed.), *Mudrosloví primáše Jožky Kubíka*

Chapter 5

Experiments

The experiments in Section 5.1 were inspired by recent attempts to use ultra-wideband ground-penetrating radar (UWB GPR) in detection of buried victims and for through-wall vision. We experimentally investigate a technique that aims at taking advantage of fast and robust processing thanks to FFT-based algorithms and slow-speed detection capabilities due to STAP. A potential application of this technique would be for instance detection of humans based on the motion of their bodies while breathing.

The multi-channel airborne radar measurement (MCARM) program [20] was developed at the Air Force Research Laboratory, in Rome, New York. Within this program, multi-channel clutter data were collected using an L-band phased array. The MCARM database comprised pre-processed airborne radar datacubes. Each acquisition data file consists of a single coherent processing interval. MCARM data were collected during several Delmarva and East Coast fly-overs terminating in Florida. Section 5.2 is describing some experiments done with the data.

In Europe, a legal entity has been established by Germany, France, Italy, Spain and The Netherlands in order to develop a Stand-Off Surveillance & Target Acquisition Radar (SOSTAR) and execute a demonstration program (SOSTAR-X) [2]. The system incorporates a next generation Imaging SAR/MTI Radar representing the scalable state-of-the-art solution for ground surveillance. The SOSTAR-X demonstrator is integrated into an airborne platform to demonstrate the feasibility of its sophisticated sensor technology, alongside with near real-time processing and visualisation functionality. MTI processing results using data recorded by SOSTAR-X are presented in Section 5.3.

5.1 GPR data

Ultra-wideband (UWB) data from a ground penetrating radar (GPR) designed by the International Research Centre for Telecommunication and Radar (IRCTR) [32]

of the Delft University of Technology was acquired. It was used to demonstrate the potential of our models and algorithms for the buried victims detection using UWB GPR technology. A non-calibrated phased array of seven sensors was used in the scanning system developed in the IRCTR's lab. The first results with proposed models even for this type of radar system will be presented in this section.

Table 5.1: GPR processing parameters

parameter	value	description
X_1	-0.3 m	distance to the center of imaged area
L	0.72 m	synthetic aperture length
D	0.3 m	phased array length
M	145	number of azimuth samples
N	7	number of sensors
P	100	number of range samples
ω_c	0 rad/s	angular carrier frequency
Δt	$10^{-9}/4096$	fast time sampling rate

Parameters relevant to the processing are summarized in table 5.1. Note that the perpendicular distance X_1 from the array to objects was set to a value larger than the actual distance. X_1 was found experimentally during the processing to center the area of focused objects and to compensate for spatial inaccuracies such as transmitter located above the receivers rather than in-line with them.

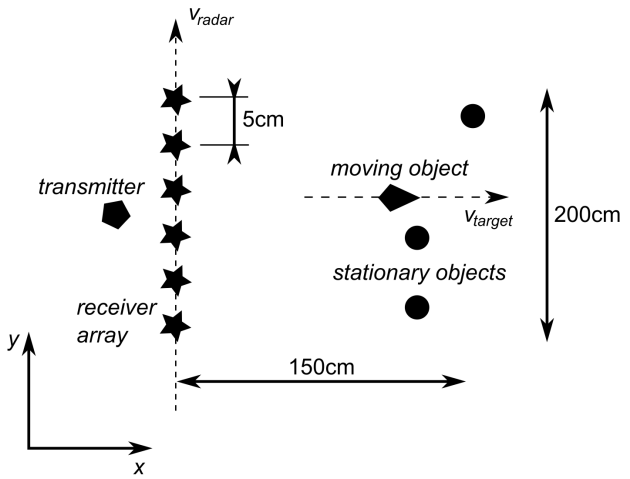

Figure 5.1: GPR setup viewed from top (not to scale).

Figure 5.1 schematically shows the actual setup. The geometry chosen is identical to the airborne moving target indicators (MTIs). A linear array of sensors is placed on a line in the direction of the y axis and it is moved in this direction over a certain distance. Each sensor records data in the same way a SAR sensor would. A SAR image is produced by each sensor. Since the sensors do not share the same viewpoint, stationary objects are shifted in azimuth over a certain amount, in each image. This shift is known and can be corrected. After that, the Fourier transform over all sensors is calculated. As a result, a three-dimensional data set is obtained where x and y axes represent space and z axis represents velocity.

Processing algorithms described in this thesis are designed for homogeneous media. In the case of GPR, a different problem arises: in the simplest approximation, a radar pulse travels first through free space (air) and then enters a different medium (soil, concrete). This medium is most likely to have different electromagnetic properties (such as permittivity) than free space. Thus, refraction will occur. In free space, the radar would see a surface target at its actual position. However, in sand (figure 5.2), a target should appear to the radar at a position that is not real. Using refraction, one would expect that in an UWB GPR experiment where a frequency-domain SAR processing is used, objects on the surface will appear closer than objects at the same vertical positions under the surface.

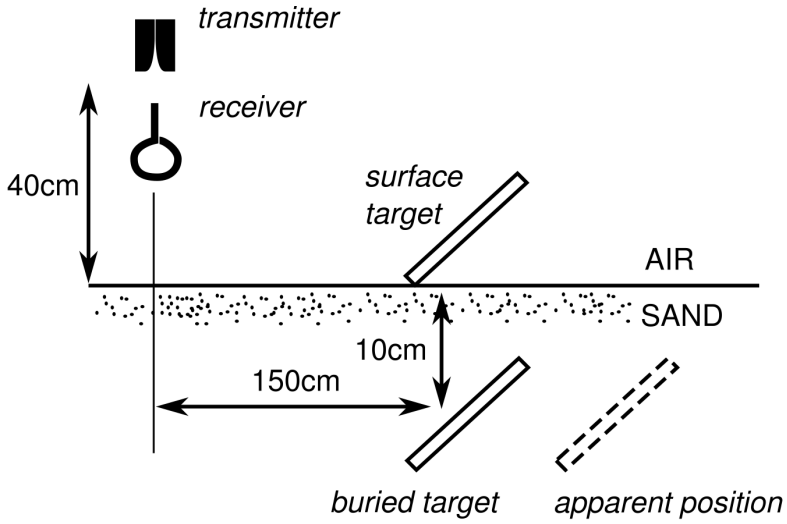

Figure 5.2: GPR setup viewed from a side (not to scale).

Therefore, the first experiment was set up to confirm that the two-layer media model is suitable for our needs. The refraction due to the boundary causes a buried object to appear at a virtual position, but the signature stays focused. Figure 5.3 shows two focused objects from the scenario depicted in figure 5.2. One reflective plate was placed on the surface of a sand pit, the other was placed about 10 cm below

the surface. One can observe that the shape of the focused signature is nearly the same in both cases. The only difference is the position. One can thus deduce that the focusing properties of a free-space based SAR-MTI processing algorithm will not be affected by the different media in our experiment.

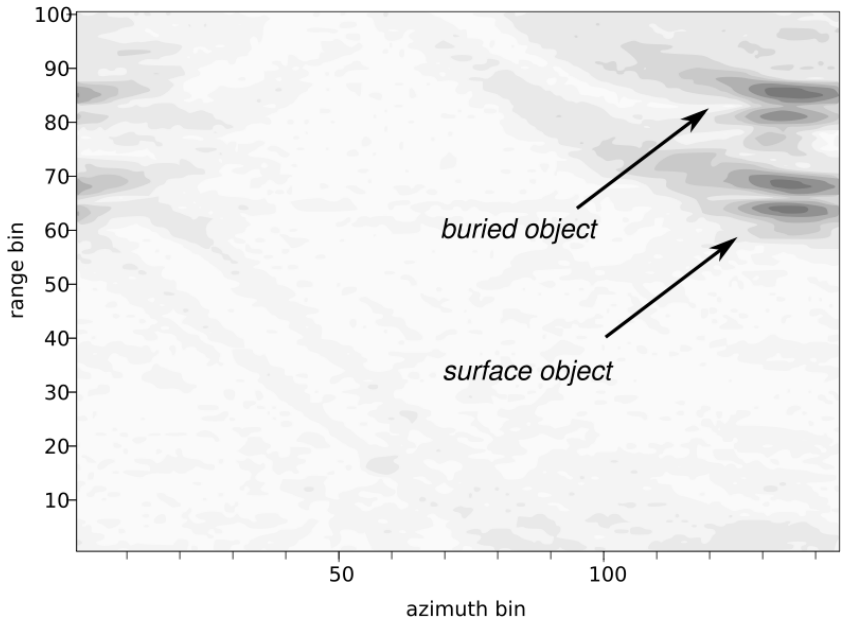

Figure 5.3: GPR processed data: surface and buried targets.

The second experiment was aimed at detection of a slowly moving target in stationary background. At the time of the experiment, it was difficult to carry such campaign out with a moving object actually buried in the sand. However, since it was confirmed that results after processing will not depend on whether the object is underground or not, surface measurements were performed. Three metallic discs were placed on the surface of the sand and a small metallic object of a comparable radio cross section was slowly pulled on a cotton thread during the data acquisition, as shown in figure 5.1. To have an easy comparison, a baseline measurement of the background without any targets in the scene was done first. Then, stationary targets were placed on the sand and the measurement was repeated. Then, the moving target was slowly towed across the sand. We were only interested in how well the moving target could be separated from the three stationary ones. The remaining background due to surface reflection and edges of the sand pit was removed by subtracting the baseline measurement from the data with stationary and moving objects. Two raw datasets were created:

1. stationary and moving targets measured with background subtracted,

2. stationary and moving targets measured with background and stationary targets subtracted

The first dataset was processed by using the algorithm described by example 2 in Chapter 3. Since the sensors were not calibrated, PCA was applied before the Fourier transform in the d domain (the sensors). The second dataset was processed by the same algorithm, only without PCA, to focus onto the moving object under the same conditions in order to make comparisons. Since all stationary targets and background were removed from the dataset number 2 in the best possible way, this result serves as a measure of how well the PCA worked in the first case. Slices of the processed data cube are shown in figure 5.4. They are taken at zero velocity, so the domain shown is the spatial (x, y) azimuth-range domain – or in other words, it shows a SAR image. Note that due to a poor velocity resolution given by the small number of antennas, the moving target signature will be visible also in the zero-velocity slice. This slice is chosen allowing to evaluate how well the stationary objects were suppressed. The top of figure 5.4 shows all targets including the moving one processed without stationary targets removal. The middle of figure 5.4 shows a moving target extracted using the PCA method. This can be compared to the bottom of figure 5.4 where the moving target is extracted via subtraction.

One can observe a very good match between the ideal result (figure 5.4, bottom) and the estimated one (figure 5.4, middle). Some weak remains of stationary targets are still visible after PCA extraction. Note that averaging was not possible due to a severe channel mismatch.

Our processing methods were designed to be robust enough to cope with a relatively large error margin. Various locations of the transmit antenna with respect to the receive array were tested. Even if the transmitter was actually some 25 cm from the array with a length of 30 cm, a basic SAR processing assuming collocated transmitter and receivers was used. The sensitivity to the relative positions of the transmitter and receiving array was found to be low. For a system with a range resolution of about 15 cm, this is to be expected. Also, different transmit antennas were tested, namely Vivaldi and loop antennas. The difference was found only in gain, which affects the brightness of the SAR images.

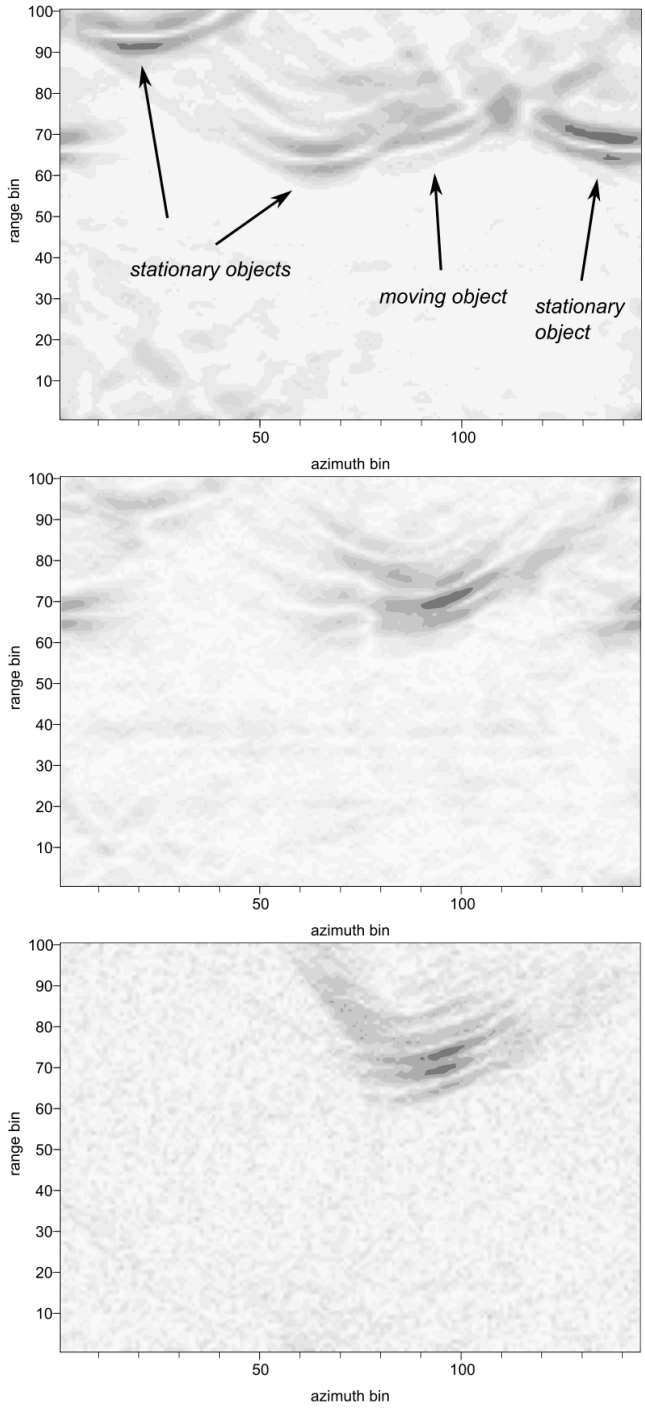

Figure 5.4: GPR processed data: (top) stationary and moving targets; (middle) a moving target extracted using PCA; (bottom) a moving target extracted using subtraction.

5.2 MCARM data

The data from the MCARM database [20] were used to carry out some validations. Due to their low resolution the following approximation was used [20,46]:

$$\mathrm{f}(x, y, v_x) = \mathcal{F}_{u,d}\left\{s(t, u, d)\right\} \tag{5.1}$$

This means the model described by equation (4.6) applies. The data were treated as a three-dimensional array, with a size as given by table 5.2. The array is arranged in two rows of sensors that are placed vertically on top of each other. The provided MCARM data is organised in several files according to different flights and different acquisition regimes. In this section, results obtained from the upper half of the sensor array of the data set from file `re050146` are presented. The Fourier transform was calculated using the FFT and the d domain was zero padded up to 256 points, so the resulting data cube is of a size $M = 256, N = 256$ for $P = 630$ range samples. Note that unlike most authors dealing with these data, only lower or upper part of the sensor array was used in this thesis, hence $N = 11$ before zero-padding.

Table 5.2: MCARM processing parameters, file `re050146`, upper half of the sensor array.

parameter	value	description
PRF	1984 Hz	pulse repetition frequency
Δd	4.3 in	sensor spacing
M	128	number of azimuth samples
N	11	number of sensors
P	630	number of range samples
ω_c	$2\pi \cdot 1.25 \cdot 10^9$ rad/s	angular carrier frequency
v_r	413 ft/s	radar velocity

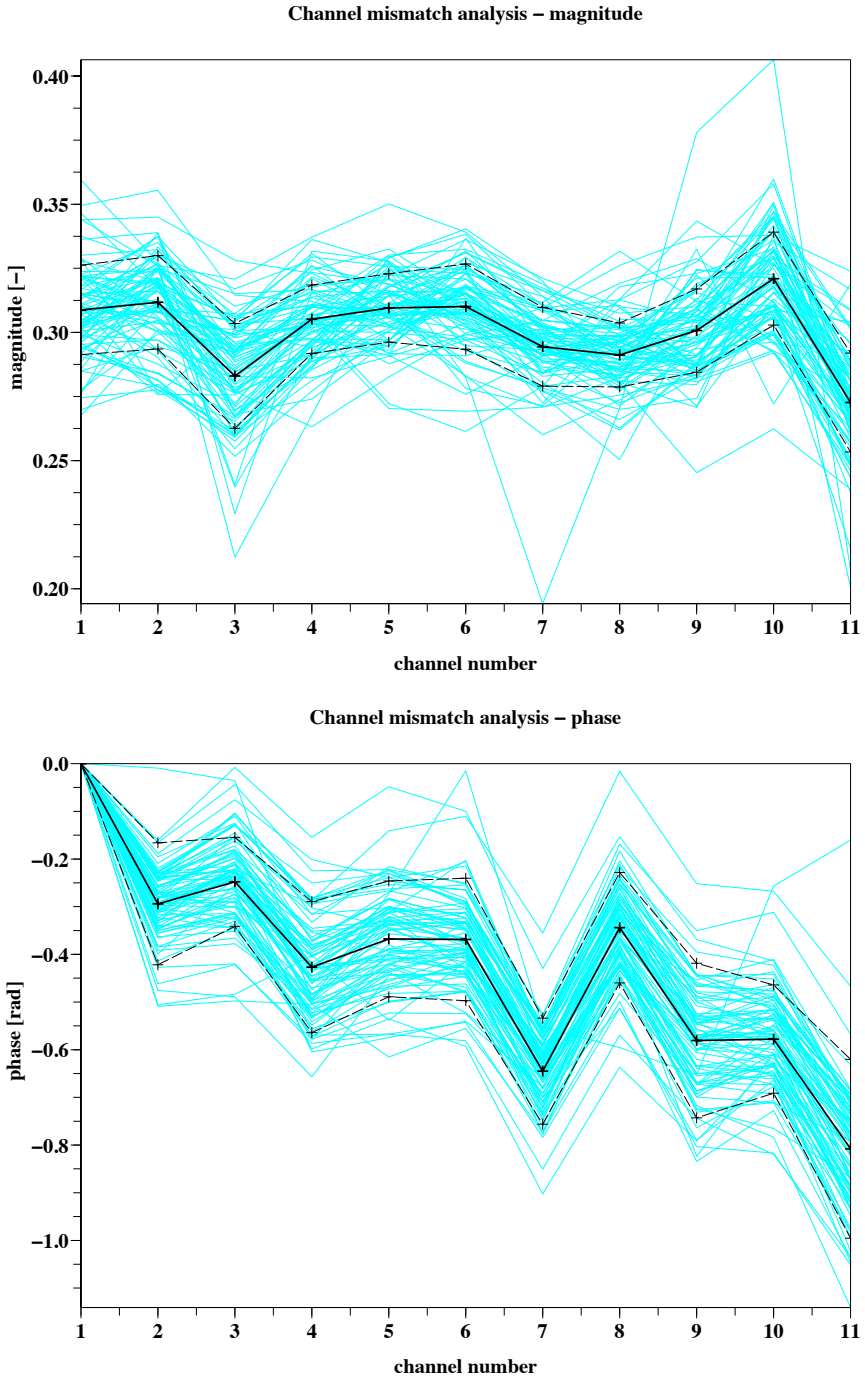

Figure 5.5: Channel mismatch: (top) magnitude, (bottom) phase.

5.2.1 Studies of channel mismatch

As explained in subsection 4.3.2, an estimate of the complex channel mismatch function $e(d)$ can be obtained from the first column of matrix $\boldsymbol{V}$. Magnitude and phase of this function are depicted in figure 5.5. The thin lines represent every 10^{th} range line p in the data. The thick solid line represents an average over all range lines, the dashed lines depict the standard deviation also calculated from all range lines. Comparison of these results with figure 3 in [20] reveals that the PCA based method implicitly performs a so-called *global calibration*. One can observe a similar trend in all lines in the phase plot. This supports the initial assumption of a range (time) independent function e. The situation is different in the magnitude plot. However, this result will still satisfy the requirement of orthogonality, since the randomness of magnitude will be averaged out in the final processing step (see subsection 4.3.1). This range-variant magnitude of function e is almost certainly due to noise.

5.2.2 Moving Target Detection and Indication

In figure 5.6 (top) the magnitude of the two-dimensional Fourier transform of the range slice $p = 386$ is displayed. The marked target is moving target M_4. The target is identified as moving because it is visibly offset from a line running diagonally, which represents stationary targets. Figure 5.6 (bottom) depicts the same situation, after the shifting function s_s was applied. To obtain the top picture from the bottom one in figure 5.6, a factor $\gamma = 0.0736$ was used. This particular value of γ gives maximum clutter suppression in the measured data. Using $PRF = 1984$ Hz, $v_r = 413$ ft/s, and $\Delta d = 4.3$ in obtained from data description in table 5.2, factor γ is calculated to be 0.0795. The difference between the values of γ obtained experimentally and by calculation is approximately equal to 7.4%. It is probably caused by the difference between the nominal values of the acquisition parameters and the actual ones. Applying the calculated γ to the data causes a perceptible but not significant change in the clutter suppression.

Figure 5.7 (top) shows the case when clutter is stronger than the moving target M_4, which would not be detected in a single-channel SAR image by simple thresholding. Target M_4 was located at range $p = 386$ in the examined MCARM data set. The included results of PCA but especially the results of figure 5.7 (bottom) reveal a very good performance of the simple algorithm from subsection 4.3.1 based on taking the average of the data from multiple channels after the alignment by using function s_s and subtracting this average from each channel's data. This example would also suggest that MTI based on averaging would not fail on this particular dataset due to a calibration error, which seems to be contrary to the statements in [20]. Since the phases and gains of each channel were calculated earlier and therefore they are known, some idea can be gained on what constitutes a "well calibrated"

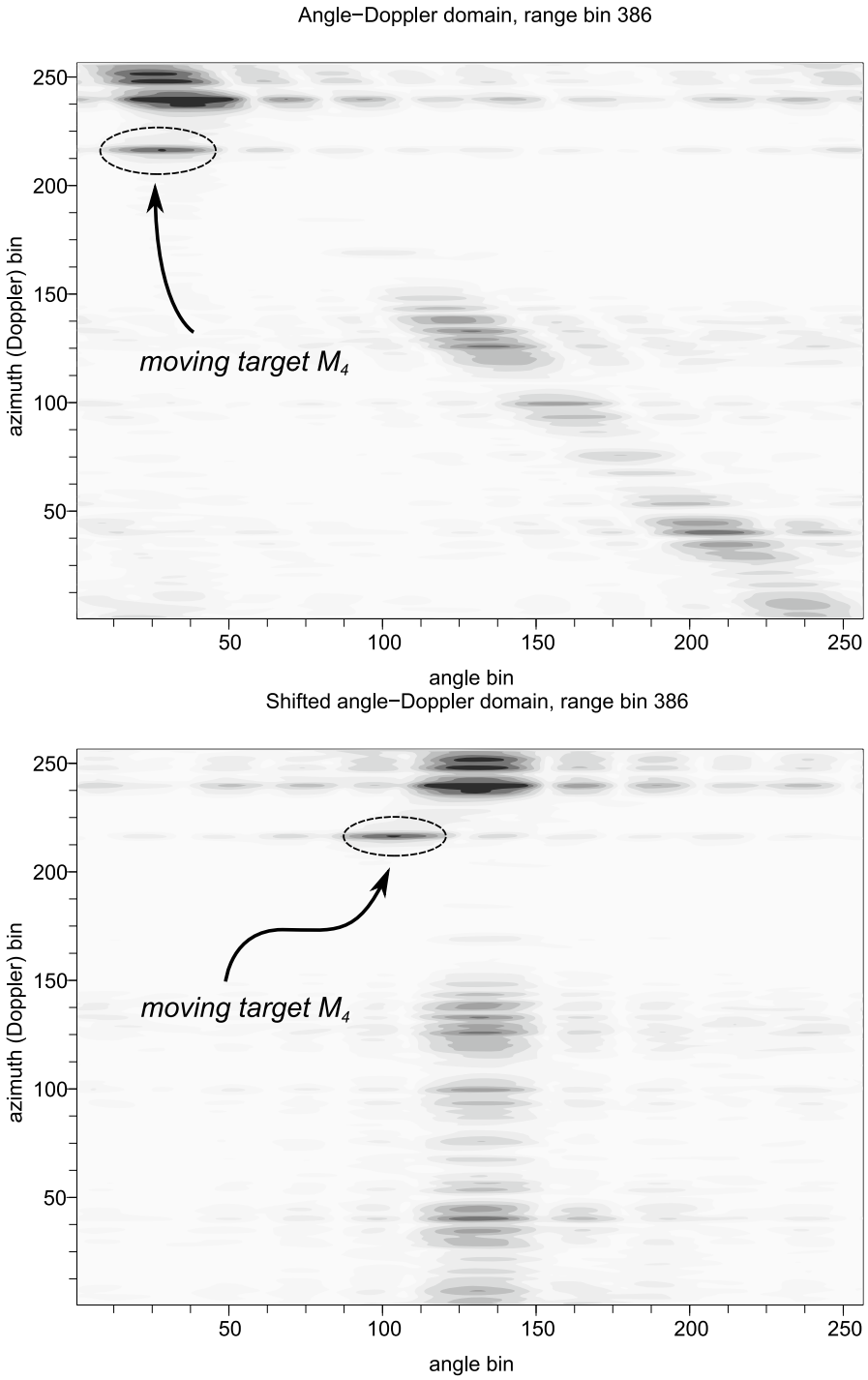

Figure 5.6: Top: Data in the angle-Doppler domain. Bottom: Data in the angle-Doppler domain, shifted.

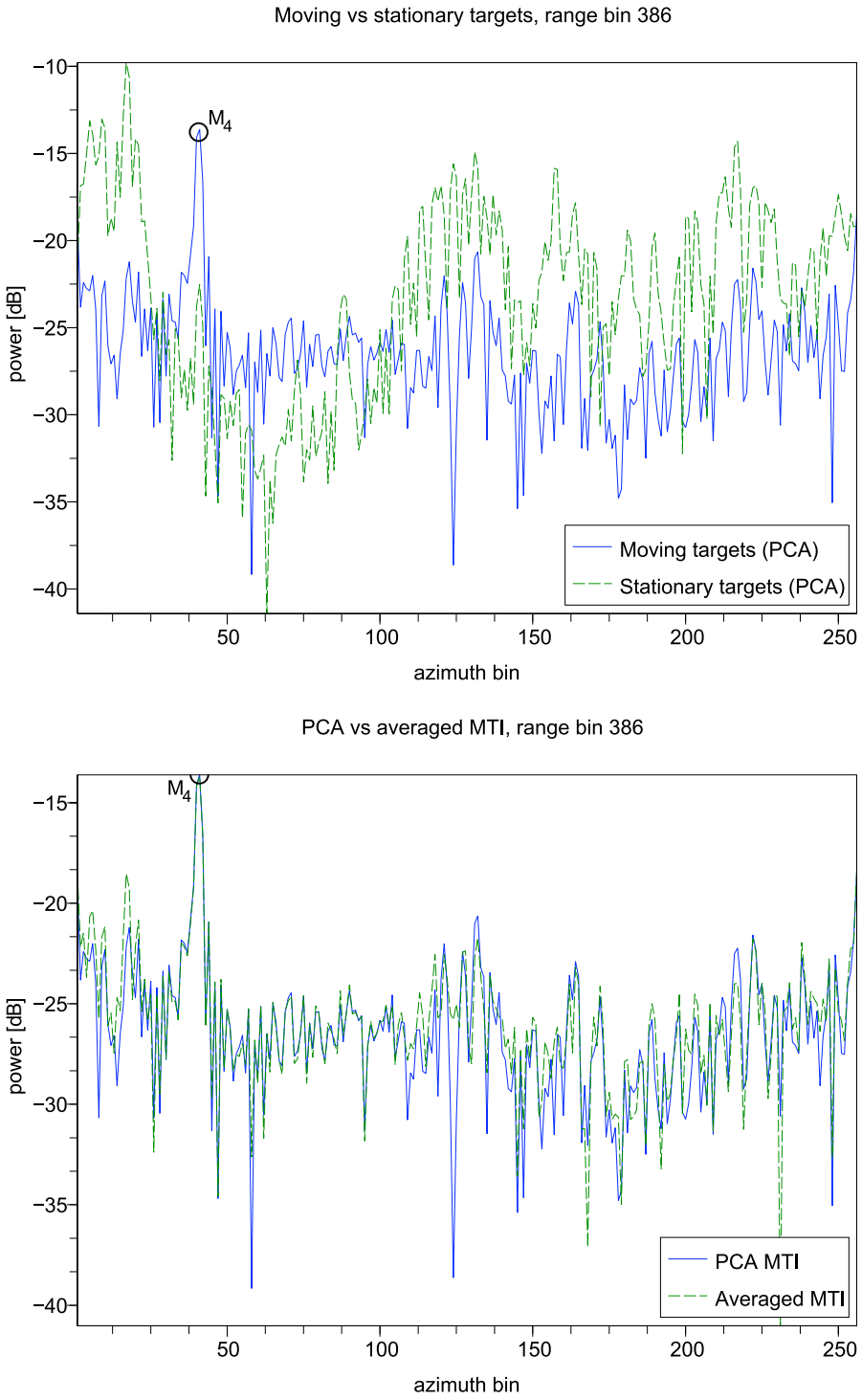

Figure 5.7: Weak moving target in clutter: (top) stationary targets and moving targets extracted using PCA, (bottom) moving targets extracted using PCA and using the algorithm from subsection 4.3.1.

multi-channel airborne radar data set. Hence, the following statement can be made: *The MCARM dataset* `re050146` *exhibits a relatively low channel mismatch.*

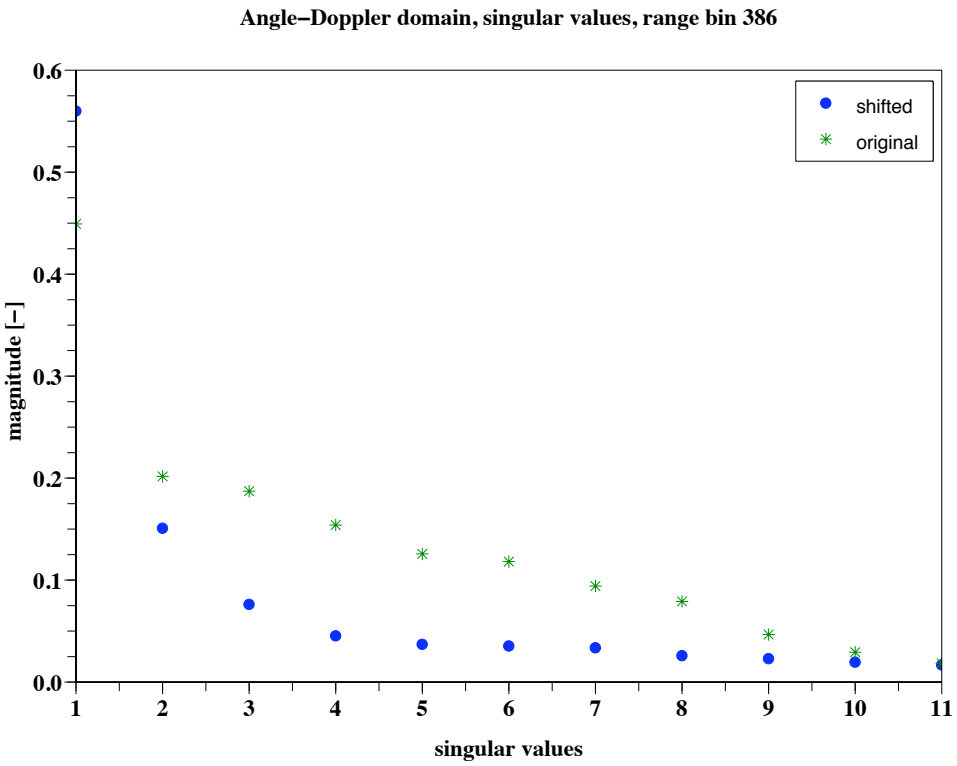

Figure 5.8: SVD analysis, range 386.

Figure 5.8 shows singular values of the range slice $p = 386$ before and after the shift, respectively. A significant change of higher singular values due to the shift can be observed. In this particular case, most of what is called "subspace leakage" in STAP literature [17, 18] seems to have deterministic origin and it can be removed.

Authors [15, 20, 46] chose a slice of the datacube at range $p = 450$ due to a simulated moving object present there. Figure 5.9 displays our results. They are nearly identical with the results of previous authors, yet they are obtained by much simpler and faster means. Figure 5.9 (top) shows that a good separation between stationary (S_1 to S_4) and moving (M_1 to M_3) targets is provided. Figure 5.9 (bottom) shows a comparison between the MTI algorithm based on averaging over the data from multiple channels and PCA-based MTI. Nevertheless, it is obvious from the data that any reasonable MTI method will perform well, since moving targets are stronger than the stationary ones at this particular range. This is clearly demonstrated on various results shown in reference [20].

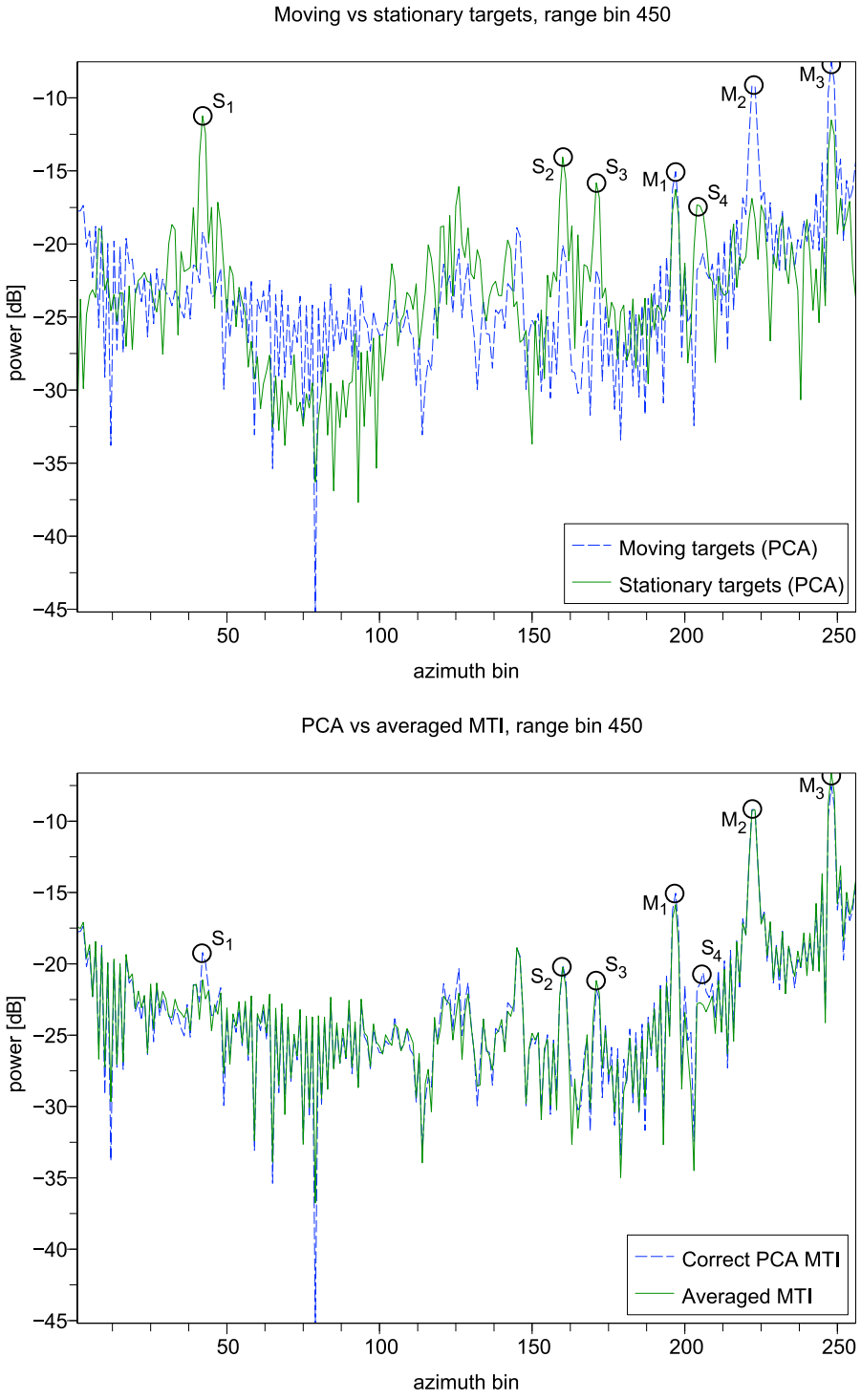

Figure 5.9: Strong moving targets in clutter. Top: MTI processing versus SAR processing. Bottom: PCA versus averaging.

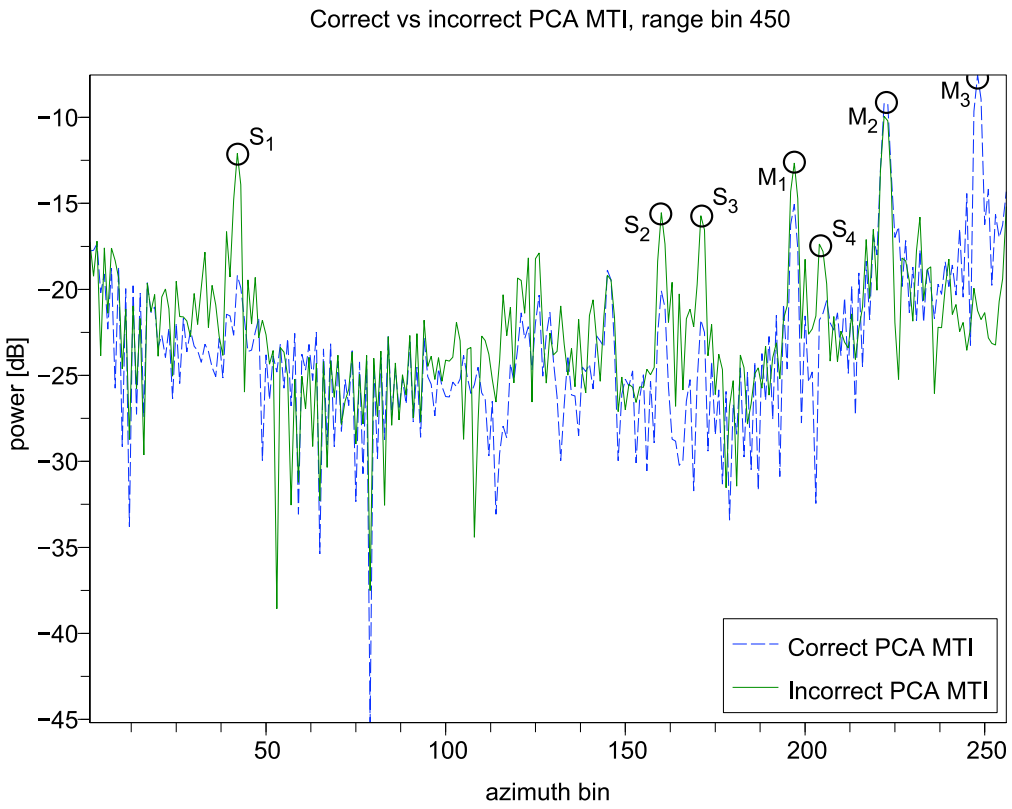

Figure 5.10: Shortcomings of PCA.

It was mentioned in subsection 4.3.2 that the PCA-based MTI method will fail in case the clutter is weaker than the reflections from moving targets. This is illustrated in figure 5.10. It shows that in case of PCA, performed on an one range slice only, the strongest target M_3 will be suppressed while the stationary targets S_1 to S_4 will remain unaffected. A simple remedy to this problem is taking more range slices into account and stacking them one on top of another. A dashed line in the same figure shows the result after stacking of 20 adjacent range slices around $p = 450$. However, this might not be a desirable solution, since it increases the computational complexity. One could rather conclude that a different signal separation algorithm, such as ICA should then be sought.

5.3 SOSTAR data

This section presents data from an early SOSTAR system test flight. Although nearly all information about this data set was classified, results with the MCARM data and GPR data MTI processing provided necessary confidence and validation

of the MTI algorithms. Again, the approximation

$$\mathrm{f}(x, y, v_x) = \mathcal{F}_{u,d}\{s(t, u, d)\} \tag{5.2}$$

was used. This made the knowledge on L, D, ω_c or PRF irrelevant. We set $D = 1$ and estimated the factor $\gamma = 0.0449$ for the best clutter suppression. The original range-compressed data consisted of an array of $M \times N \times P = 128 \times 3 \times 91$ azimuth, channel and range samples. The data was shifted in angle-Doppler domain using the function s_s and zero-padded up to 256 samples in the azimuth direction. To extract the moving targets, MTI algorithms based on PCA and on averaging were applied to the data set. The two-dimensional Fourier transform was calculated for each range slice p. In this way, three new data sets were obtained: i) a data set where only function s_s, zero-padding and the Fourier transform was applied; ii) a data set where PCA was applied prior to the Fourier transform to remove clutter; iii) a data set where the algorithm based on averaging over the channels was applied prior to the Fourier transform. Each of these new data sets represents focused data in azimuth, angle and range domain. Since $N = 3$, there will be virtually no difference between focused data from any channel. We chose a slice for $N = 2$ from each dataset. The slice from the first data set would represent a SAR image with moving targets present, the slices from remaining data sets should represent SAR images with stationary targets (clutter) removed.

Figure 5.11 shows SAR images of moving targets and clutter (top), and moving targets extracted by PCA (bottom). Clutter is represented by the horizontal band in the middle of the top picture. Originally, the SOSTAR data presented in this section were acquired for a purpose different than the multi-channel airborne MTI. For this reason, the measurement was set up in such a way that all moving targets are found outside of the clutter band. These moving targets can be clearly identified in the SAR image even without any MTI processing. A simulated target signature M_2 was inserted inside the clutter band to model the scenario where weak moving targets are masked by clutter. We note that *blind data processing* was employed, so no prior knowledge related to clutter or moving targets was used. The only assumption considered was a straight flight path. The bottom picture shows the results after clutter suppression using PCA. The SAR image reveals a number of signatures possibly representing moving targets. Two moving targets located in range bin $p = 10$ are identified: M_1 is a real moving target, M_2 is the simulated one.

As in the case of the MCARM data processing, the MTI algorithm from subsection 4.3.1 based on averaging of the data over multiple channels was tested on the SOSTAR data set. The objective was to see whether this simple algorithm would produce useful results in this case. Figure 5.12 shows first 20 range bins of SAR images obtained from the three different data sets discussed earlier. The SAR images on the left and in the middle are details of the images from figure 5.11. The picture

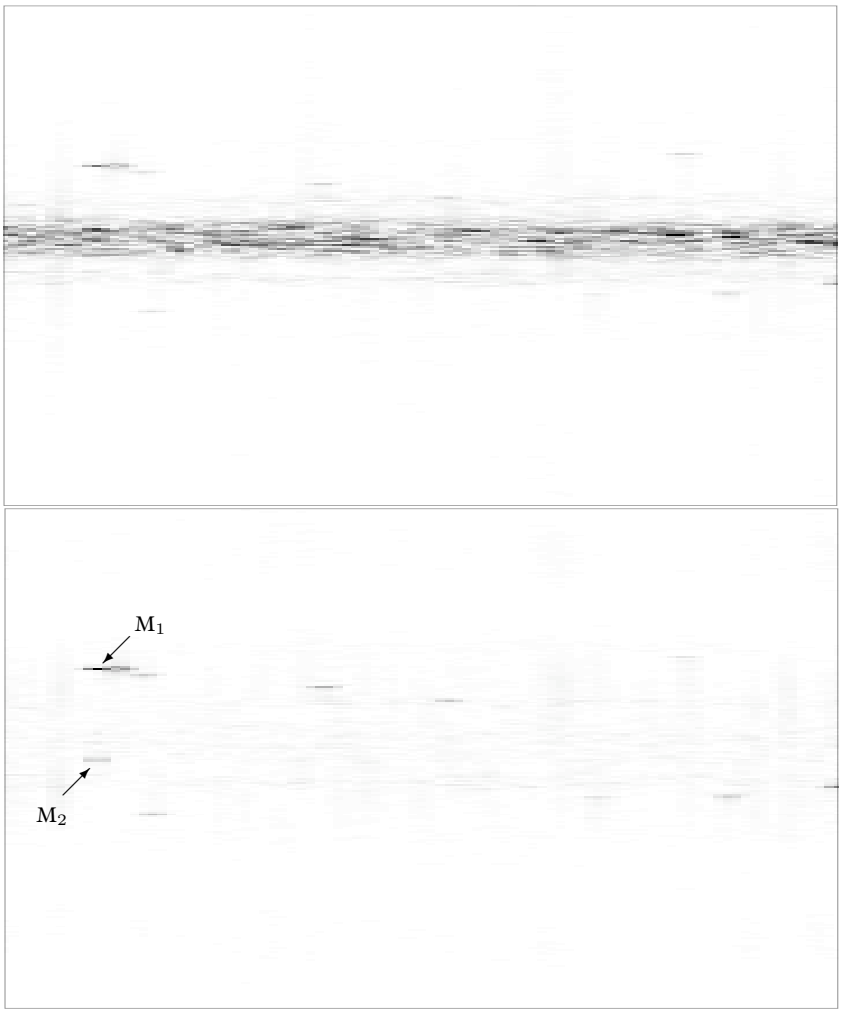

Figure 5.11: SOSTAR SAR images each consisting of 256 azimuth (vertical) $\times$ 91 range (horizontal) bins: (top) clutter and moving targets present; (bottom) presumed moving targets extracted using PCA. Moving target M_2 is simulated.

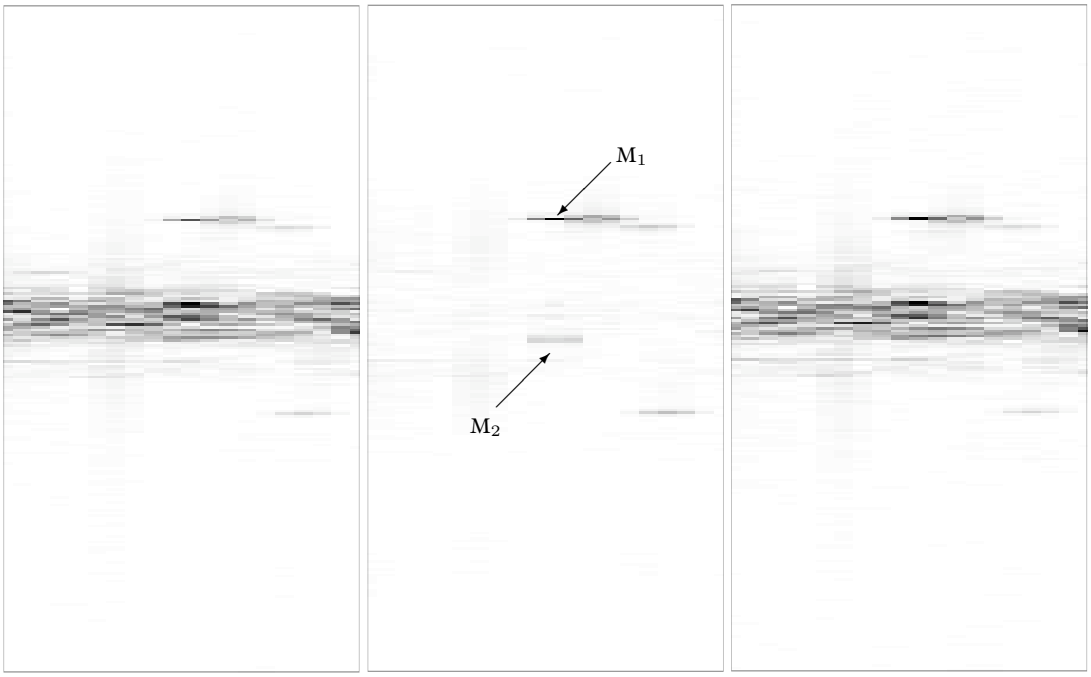

Figure 5.12: Detail of SOSTAR SAR images: (left) clutter and moving targets present; (middle) moving targets extracted using PCA; (right) results after the average over the channels was subtracted from the shifted data.

on the right shows results after the MTI algorithm based on averaging was used. One can see that this algorithm has left clutter practically unchanged. In the light of the results from the previous section, this is most likely caused by the channel mismatch. The two moving targets from figure 5.11 (bottom) are highlighted in the middle picture: Target signature M1 finds itself outside the clutter band – as well as many other similar signatures in the picture.

Figures 5.11 and 5.12 give a good overview of the overall performance of the MTI algorithms. Clutter suppression can be assessed for all range slices at once and any features such as moving targets are immediately visible in the SAR images. However, it is not easy to see by what amount exactly was clutter reduced, for instance. Figures 5.13 and 5.14 provide such information. They show line plots of range bin 10 obtained from SAR images in figure 5.12. Thus, this imaginary line runs vertically exactly in the middle of each SAR image. Target M2 is fully masked by clutter in the top and bottom pictures of figure 5.13, whereas it is visible in the top picture in figure 5.14. We note that should target M2 not be present, clutter would be further suppressed to a level of about -10 dB in figure 5.14 (bottom). Since the original level of clutter is about 2.5 dB higher than the level of target M_1 in figure 5.13 (top), the total clutter suppression was approximately 12.5 dB in this case.

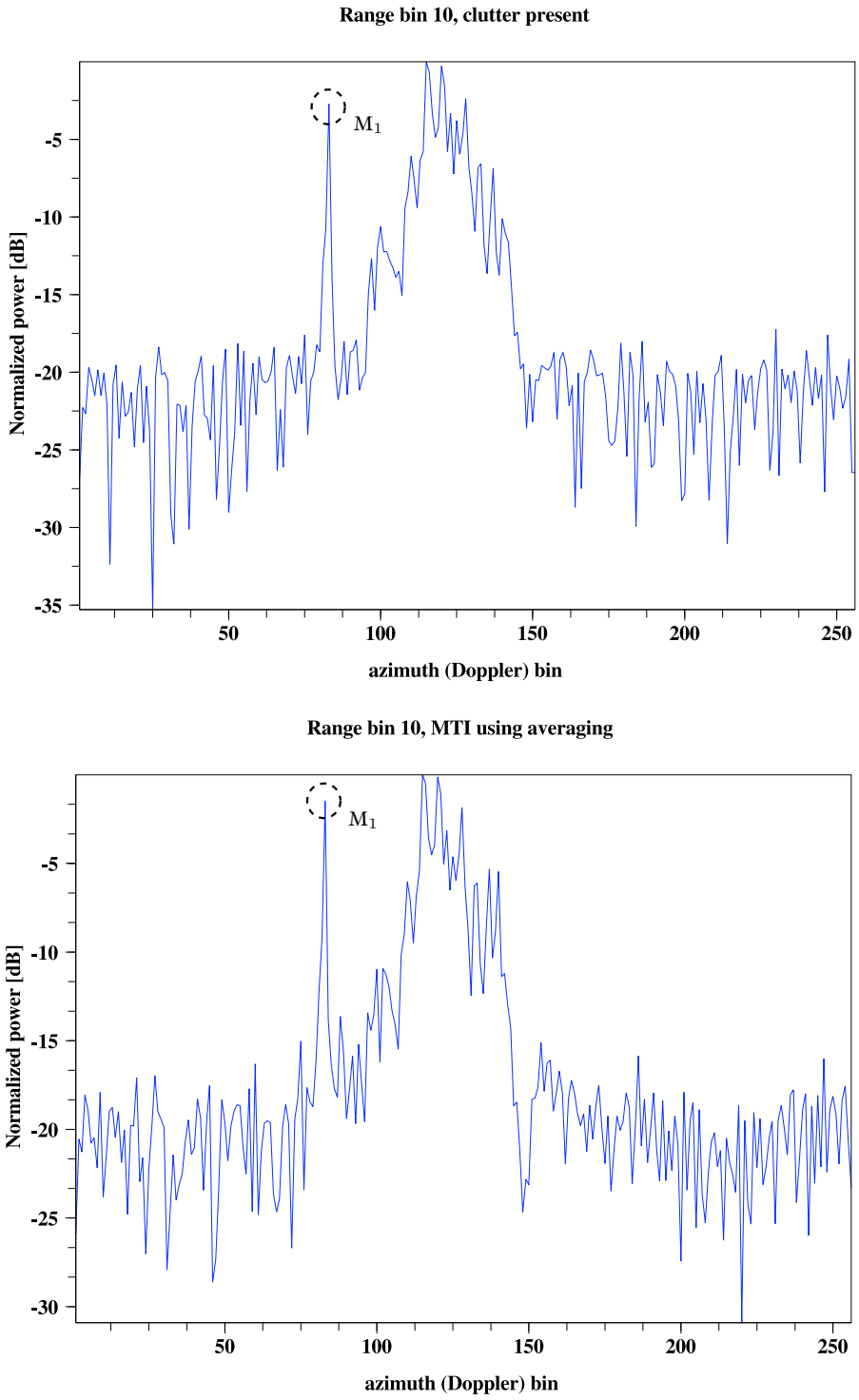

Figure 5.13: SOSTAR data line plots: (top) range bin 10, clutter + targets; (bottom) range bin 10, results after the average over the channels was subtracted from the shifted data.

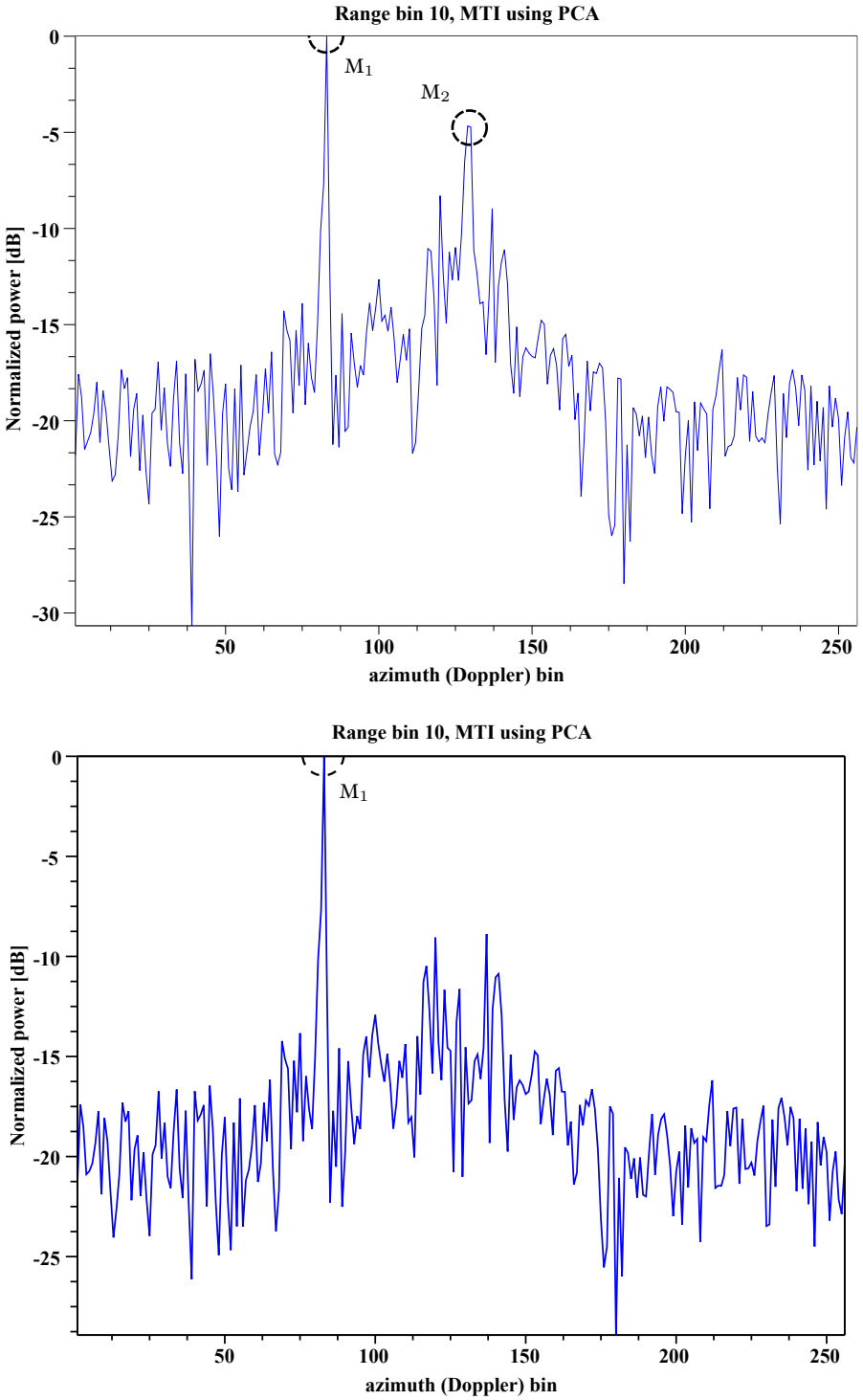

Figure 5.14: SOSTAR data line plots: (top) range bin 10, PCA applied; (bottom) range bin 10, synthetic target M2 not inserted, PCA applied.

5.4 Concluding remarks

We have experimentally shown that it is possible to treat subsurface UWB GPR imaging problems using the geometrical optics' point of view, which makes free-space based SAR algorithms suitable for use in GPR processing. Further, we have succeeded in detection of a slowly moving object in a scene where stationary moving objects were strongly present. Connecting these two findings establishes an experimental basis for further experiments in detection and imaging of objects moving under rubble, for example after an earthquake.

MCARM dataset was analyzed and results were compared to those found in literature. A good match was found. The PCA-based MTI algorithm was compared to averaging. Since the results were nearly identical, it was confirmed that averaging is a good approach to MTI in a well calibrated radar. The same MTI processing algorithms were tested on SOSTAR data. Although many data sets of SOSTAR-X were well calibrated, this particular one exhibits 3 uncalibrated sensors. Hence, averaging did not produce satisfactory results. When a PCA was applied, clutter was reduced significantly. Since PCA is known to work well only when the angle-independent channel mismatch model is assumed [17, Chapter 4], it could be concluded that this model is valid for SOSTAR data. MCARM and SOSTAR represent narrow-band radars. There are often concerns whether the same channel mismatch model can be applied to wide-band radars as well. The results with IRCTR's UWB GPR confirmed this possibility.

In this thesis, it is assumed that the path on which the radar travels is linear. This information is used in processing to expect clutter to be a rank-1 matrix. Naturally, such assumption is never entirely valid in practice, due to various external factors: wind, speed variations, etc. However, if the *intended* path was linear, it seems likely that the radar indeed travelled on a straight trajectory at least for a short period of time. For example, the entire MCARM dataset was recorded in $M/\text{PRF} \approx 65$ ms and the radar travelled about $v_r M/\text{PRF} \approx 89$ meters within this time interval (see table 5.2). 65 ms seems a very short time for a radar platform travelling at 413 ft/s to deviate significantly from a straight line. Validity of the straight trajectory assumption is supported by the analysis of singular values in Section 5.2.

Chapter 6

Conclusions and Future Work

What now? It was a vicious circle. If you succeed with one dream, you come back to square one and it's not long before you're conjuring up another, slightly harder, a bit more ambitious – a bit more dangerous.

Joe Simpson, *Touching the Void*

In this chapter, final conclusions are drawn. We start by providing answers to the key questions defined in the introduction. Then, we proceed to give some recommendations for future work. The main objective of this thesis was to answer four key questions:

Are there any benefits in combining SAR and STAP? In Chapter 3, we put forth an extended approach to modeling of multi-channel SAR moving target indicators. The main idea was to derive an inversion algorithm that would produce *images* of moving targets with resolution equal to the resolution of images of stationary targets using SAR. Indeed, such inversions have been found, albeit for some cases only. The signal model proposed in Chapter 3 is fully general for the given geometry. However, it is shown on numerical examples that its inversion is practically useful only for very short distances where the plane-wave approximation is no longer valid. Nevertheless, this is an area not yet thoroughly explored by other researchers. The approach discussed in Chapter 3 is therefore mainly suitable for generation of synthetic datasets for numerical evaluation of SAR/MTI processing techniques, but also for a study of new, potentially interesting applications such as MTI with ultra-wideband ground penetrating radar.

Is it possible to find a fast yet optimal or near-optimal MTI algorithm? Chapter 4 presents a simplified signal model more suitable for current multi-channel airborne MTI radars. A known STAP approach based on PCA is

applied to it. Two special cases are studied: i) the narrowband case of an angle-independent channel mismatch and ii) no channel mismatch present. It is shown that in the case of no mismatch, the clutter rejection reduces to simple averaging. Having to apply PCA on an angle-Doppler matrix is always a more complex task then obtaining a simple column (row) mean of the same matrix. Thus it is suggested that if the channel calibration is done properly, it will yield considerable savings in the computational power necessary to perform MTI. A real-time implementation of such an algorithm by means of a high-pass filter was already proposed by other authors.

How would such an algorithm perform when applied to measured data? A PCA-based algorithm and averaging was applied to two airborne datasets: i) one based on the MCARM data, ii) the other based on the SOSTAR-X data. Results with MCARM data produced by both methods were compared to other published results and they match well. Moreover, the results produced by PCA were nearly identical to the results produced by averaging. Thus, it was concluded that the narrowband angle-independent channel mismatch model could be assumed and that the MCARM dataset channel calibration was sufficient. Similar comparison was done for the SOSTAR-X dataset. Contrary to the MCARM data, the SOSTAR-X data contained a severe channel mismatch. This was asserted after it was found that PCA produced expected results.

How can we use STAP in a new fashion? A way to detect victims buried in debris during natural disasters or terrorist attacks is proposed in Chapter 5. Several experiments with ultra-wideband ground penetrating radar were carried out at the International Research Centre for Telecommunications and Radar of Delft University of Technology in the Netherlands. The models and multi-channel SAR/MTI processing methods developed in Chapter 3 were applied to the acquired data. Since the sensors were not calibrated, the PCA method was used. Although this method assumes a narrow band channel mismatch model, the results were in good agreement with predictions.

6.1 Recommendations

Every research work leaves several open questions. Some of the questions this work has possibly generated will be addressed in this section.

The number of available sensors. It is always desirable to keep the number of sensors to a minimum, mainly due to the costs. However, it can be shown that it is difficult to find the position and velocity of a moving target with an

insufficient number of sensors to determine the angle of arrival. This difficulty is caused by the *blind angle* problem [5, 35]. It is therefore very likely that when imaging SAR MTI radar is considered, a higher number of sensors – antenna elements (Klemm considers 1000 elements as a realistic number, see [24, Chapter 4]) needs to be taken into account. In such case, FFT-based processing becomes a viable option. To improve velocity resolution of FFT-based processing, a form of active beam steering was suggested [36]. A practical device utilizing this technique has not yet been reported in the open literature.

Sensor calibration. One of the useful properties of STAP algorithms (also used here) is the fact that they can – to some extent – cope with channel mismatch. Nevertheless, it was shown in this thesis that such capability comes at a price of increased processing complexity. We have shown that at least for one experimental radar system treated here, i.e. MCARM, a sufficient calibration was achieved. With the growing popularity of radars based on the MIMO principle, some of which require good channel calibration [21, 26], channel mismatch is expected to become less of an issue in the future. It is therefore recommended to focus further efforts on handling the increased data flow connected with a multichannel SAR imaging device.

Clutter separation. STAP is defined as a linear problem [17, 24]. The final formulation of the problem in Chapter 4 allows not only the application of PCA, but also independent component analysis (ICA) [39]. ICA generalizes PCA for non-Gaussian noise sources. Since radar clutter is made of reflections from natural or man-made objects, it is possibly non-stationary or even chaotic. Signal separation techniques for non-Gaussian and chaotic signals exist [22]. Their application in STAP could be suggested.

Appendix A

Solutions to Certain Integrals Using the Method of Stationary Phase

A.1 Stationary targets

We wish to evaluate the following integral

$$S(k_u, k_d) = \iint_{-\infty}^{\infty} \exp\left[-\jmath k r(u,d)\right] \exp\left[-\jmath(k_u u + k_d d)\right] \mathrm{d}u \, \mathrm{d}d, \tag{A.1}$$

where

$$\begin{aligned} r(u,d) \;=\; & \\ & \sqrt{x^2 + (y-u)^2} \\ & + \sqrt{x^2 + (y-u+d)^2}. \end{aligned} \tag{A.2}$$

First, a more suitable expression of the phase function will be written. By substitution $v = u - d/2$ one gets

$$S(k_u, k_d) = \iint_{-\infty}^{\infty} e^{\jmath\psi(v,d)} \, \mathrm{d}v \, \mathrm{d}d, \tag{A.3}$$

where

$$\begin{aligned} \psi(v,d) \;=\; & -k\sqrt{x^2 + (y-v-d/2)^2} \\ & -k\sqrt{x^2 + (y-v+d/2)^2} \\ & -k_u(v + d/2) - k_d d. \end{aligned} \tag{A.4}$$

If we denote values of the phase function at the stationary points as $\psi_l(v_l, d_l)$, then the value of the integral in equation (A.1) will be constant and can be calculated as follows

$$S(k_u, k_d) = \sum_l e^{-\jmath\psi_l(v_l,d_l)}. \tag{A.5}$$

In our case, the phase function is hyperbolic and will have one extremum. This means there will be only one stationary point. Partial derivatives of the phase function will be solved to find this point

$$\frac{\partial\psi}{\partial v} = 0, \qquad \frac{\partial\psi}{\partial d} = 0. \tag{A.6}$$

This gives

$$k_u = k\sin\phi_1 + k\sin\phi_2 \tag{A.7}$$

$$2k_d + k_u = k\sin\phi_1 - k\sin\phi_2, \tag{A.8}$$

with

$$\sin\phi_1 = \frac{y - v - d/2}{\sqrt{x^2 + (y - v - d/2)^2}} \tag{A.9}$$

$$\sin\phi_2 = \frac{y - v + d/2}{\sqrt{x^2 + (y - v + d/2)^2}}. \tag{A.10}$$

Expressions that depend on v and d were obtained. However, the phase function needs to be constant with respect to v, d. To achieve this, ψ will be expressed as $\psi(k_u, k_d)$. Using the fact that $\sin^2\phi = 1 - \cos^2\phi$ and with

$$\cos\phi_1 = \frac{x}{\sqrt{x^2 + (y - v - d/2)^2}} \tag{A.11}$$

$$\cos\phi_2 = \frac{x}{\sqrt{x^2 + (y - v + d/2)^2}}, \tag{A.12}$$

equations (A.7) to (A.12) yield

$$\sqrt{x^2 + (y - v - d/2)^2} = \frac{kx}{\sqrt{k^2 - (k_u + k_d)^2}} \tag{A.13}$$

$$\sqrt{x^2 + (y - v + d/2)^2} = \frac{kx}{\sqrt{k^2 - k_d^2}} \tag{A.14}$$

and also

$$d = -x\left(\frac{k_u + k_d}{\sqrt{k^2 - (k_u + k_d)^2}} + \frac{k_d}{\sqrt{k^2 - k_d^2}}\right) \tag{A.15}$$

$$v = y - \frac{x}{2}\left(\frac{k_u - k_d}{\sqrt{k^2 - (k_u + k_d)^2}} - \frac{k_d}{\sqrt{k^2 - k_d^2}}\right). \tag{A.16}$$

Finally, substituting previous expressions back into equation (A.4), one obtains

$$\varphi(k_u, k_d) = -x\left(\sqrt{k^2-(k_u+k_d)^2}+\sqrt{k^2-k_d^2}\right) - k_u y. \tag{A.17}$$

Thus, the asymptotic solution of the double integral in equation (A.1) is

$$S(k_u, k_d) = e^{-\jmath x\left(\sqrt{k^2-(k_u+k_d)^2}+\sqrt{k^2-k_d^2}\right)-\jmath k_u y}. \tag{A.18}$$

A.1.1 Derivation of expression (3.10)

Using the result (A.1), the convolutional integral (3.9)

$$s(u,\omega,d) = \iint_{-\infty}^{\infty} f(x,y)\exp\left[-\jmath k r(x,y,u,d)\right]\,\mathrm{d}x\,\mathrm{d}y, \tag{A.19}$$

where

$$x = x - X_1 \qquad \text{and} \qquad y = y - Y_1, \tag{A.20}$$

can be evaluated as follows. We can write that

$$\begin{aligned}\exp\left[-\jmath k r(x,y,u,d)\right] \;=\; & \iint_{-\infty}^{\infty}\mathrm{d}k_u\,\mathrm{d}k_d \\ & \exp\left[-\jmath(x-X_1)\left(\sqrt{k^2-(k_u+k_d)^2}+\sqrt{k^2-k_d^2}\right)\right] \\ & \exp\left[-\jmath k_u(y-Y_1)+\jmath(k_u u+k_d d)\right].\end{aligned} \tag{A.21}$$

Inserting (A.21) into (A.19), one finds

$$\begin{aligned}& s(u,\omega,d) = \\ & \iint_{-\infty}^{\infty}\exp\left[\jmath X_1\left(\sqrt{k^2-(k_u+k_d)^2}+\sqrt{k^2-k_d^2}\right)+\jmath k_u Y_1\right]\exp\left[\jmath(k_u u+k_d d)\right] \\ & \left\{\iint_{-\infty}^{\infty} f(x,y)\exp\left[-\jmath x\left(\sqrt{k^2-(k_u+k_d)^2}+\sqrt{k^2-k_d^2}\right)-\jmath k_u y\right]\,\mathrm{d}x\,\mathrm{d}y\right\} \\ & \mathrm{d}k_u\,\mathrm{d}k_d.\end{aligned} \tag{A.22}$$

The expression in curly brackets is a two-dimensional Fourier integral. One can also write that

$$\begin{aligned}& s(u,\omega,d) = \\ & \iint_{-\infty}^{\infty}\exp\left[\jmath X_1\left(\sqrt{k^2-(k_u+k_d)^2}+\sqrt{k^2-k_d^2}\right)+\jmath k_u Y_1\right]\exp\left[\jmath(k_u u+k_d d)\right] \\ & F\left(\sqrt{k^2-(k_u+k_d)^2}+\sqrt{k^2-k_d^2}, k_u\right)\,\mathrm{d}k_u\,\mathrm{d}k_d.\end{aligned} \tag{A.23}$$

The two-dimensional Fourier transform of both sides with respect to u and d gives

$$\begin{aligned} &S(k_u, \omega, k_d) = \\ &\exp\left[\jmath X_1 \left(\sqrt{k^2 - (k_u + k_d)^2} + \sqrt{k^2 - k_d^2}\right) + \jmath k_u Y_1\right] \\ &F\left(\sqrt{k^2 - (k_u + k_d)^2} + \sqrt{k^2 - k_d^2}, k_u\right), \end{aligned} \tag{A.24}$$

which is the result in equation (3.10).

A.2 Moving targets

We wish to evaluate integral

$$S(k_u, k_d) = \iint_{-\infty}^{\infty} e^{\jmath\psi(u,d)}\, \mathrm{d}u\, \mathrm{d}d, \tag{A.25}$$

where

$$\begin{aligned} &\psi(u, d) = \\ &-k\sqrt{(x - v_x\tau)^2 + (y - v_y\tau - v_r\tau)^2} \\ &-k\sqrt{(x - v_x\tau)^2 + (y - v_y\tau - v_r\tau + d)^2} \\ &-k_u u - k_d d. \end{aligned} \tag{A.26}$$

To simplify expression (A.26), substitute a dummy variable

$$\xi = \tau(v_y + v_r) - d/2.$$

That gives

$$\begin{aligned} &\psi(u, d) = \\ &-k\sqrt{\left(x - v_x\frac{\xi + \frac{d}{2}}{v_y + v_r}\right)^2 + \left(y - \xi + \frac{d}{2}\right)^2} \\ &-k\sqrt{\left(x - v_x\frac{\xi + \frac{d}{2}}{v_y + v_r}\right)^2 + \left(y - \xi - \frac{d}{2}\right)^2} \\ &-k_u u - k_d d. \end{aligned} \tag{A.27}$$

Expression (A.27) is now in a more suitable form for simplification. To obtain an even easier solution, formula (A.27) will be further approximated as

$$\begin{aligned}&\psi(u,d) \approx \\ &-2k\sqrt{\left(x - v_x\frac{\xi+\frac{d}{2}}{v_y+v_r}\right)^2 + (y-\xi)^2 + \left(\frac{d}{2}\right)^2} \\ &-k_u u - k_d d,\end{aligned} \tag{A.28}$$

using the approximation

$$\sqrt{a^2+(b+c)^2} + \sqrt{a^2+(b-c)^2} \approx 2\sqrt{a^2+b^2+c^2},$$

provided that

$$2bc \ll\ a^2+b^2+c^2.$$

Setting τ back one obtains

$$\begin{aligned}&\psi(u,d) \approx \\ &-2k\sqrt{(x-v_x\tau)^2 + \left(y-\tau(v_y+v_r)+\frac{d}{2}\right)^2 + \left(\frac{d}{2}\right)^2} \\ &-k_u u - k_d d,\end{aligned} \tag{A.29}$$

which then becomes

$$\begin{aligned}&\psi(u,d) \approx \\ &-2k\sqrt{X^2 + \left(Y-\alpha u+\frac{d}{2}\right)^2 + \frac{d^2}{4} - \frac{v_x x d}{v_y+v_r}} \\ &-k_u u - k_d d,\end{aligned} \tag{A.30}$$

where

$$X = \frac{(v_y+v_r)x - v_x y}{\sqrt{v_x^2+(v_y+v_r)^2}} \tag{A.31}$$

$$Y = \frac{v_x x + (v_y+v_r)y}{\sqrt{v_x^2+(v_y+v_r)^2}} \tag{A.32}$$

$$\alpha = \frac{\sqrt{v_x^2+(v_y+v_r)^2}}{v_r}. \tag{A.33}$$

Using the Taylor series, expression (A.30) can be approximated as

$$\begin{aligned}&\psi(u,d) \approx \\ &-2k\sqrt{X^2+\left(Y-\alpha u+\frac{d}{2}\right)^2}+\frac{kdv_x}{v_r}-\frac{kd^2}{4x} \\ &-k_u u-k_d d.\end{aligned} \tag{A.34}$$

Phase function in equation (A.34) will be dealt with in the same manner as in the case of equation (A.4). First, stationary points have to be found via

$$\frac{\partial\psi}{\partial u}=0, \qquad \frac{\partial\psi}{\partial d}=0. \tag{A.35}$$

Evaluating this set of partial differential equations yields

$$\frac{k_u}{\alpha} = 2k\sin\phi \tag{A.36}$$

$$0 = -k\sin\phi+\frac{kv_x}{v_r}-\frac{kd}{2x}-k_d, \tag{A.37}$$

with

$$\sin\phi = \frac{Y-\alpha u+d/2}{\sqrt{X^2+(Y-\alpha u+d/2)^2}} \tag{A.38}$$

$$\cos\phi = \frac{X}{\sqrt{X^2+(Y-\alpha u+d/2)^2}} \tag{A.39}$$

$$\frac{2kX}{\sqrt{4k^2-\left(\frac{k_u}{\alpha}\right)^2}} = \sqrt{X^2+(Y-\alpha u+d/2)^2}. \tag{A.40}$$

Substituting expressions (A.36) to (A.40) into equation (A.34) will finally provide the result

$$\begin{aligned}\varphi(k_u,k_d) \approx & \\ &-X\sqrt{4k^2-\left(\frac{k_u}{\alpha}\right)^2}-\frac{k_u}{\alpha}Y \\ &-\frac{x}{4k}\left(\frac{2kv_x}{v_r}-\frac{k_u}{\alpha}-2k_d\right)^2\end{aligned} \tag{A.41}$$

So, the spectrum of a moving target will be given by

$$S(k_u,k_d)=e^{\jmath\varphi(k_u,k_d)}. \tag{A.42}$$

Please note that by setting $v_x = 0, v_y = 0$ and replacing the square root with its so-called *Fresnel approximation*

$$\sqrt{a^2 + b^2} \approx a + \frac{b^2}{2a},$$

provided that

$$a \gg b$$

one gets

$$\varphi(k_u, k_d) = -2kx + \frac{x}{2k}\left[(k_u + k_d)^2 + k_d^2\right],$$

which is the spectral phase function of a stationary target if expression (A.4) is evaluated using the same approximation.

A.2.1 Derivation of the equation (3.31)

We will use equation (A.41) and obtain

$$\exp\left[-\jmath X_1\left(\sqrt{k^2 - (k_u + k_d)^2} + \sqrt{k^2 - k_d^2}\right)\right] \approx \exp\left[-\jmath\left(X_1\sqrt{4k^2 - k_u^2} - \frac{X_1}{4k}\left(-k_u - 2k_d\right)^2\right)\right] \tag{A.43}$$

In that case a spectral response of the moving target will be

$$S(k_u, \omega, k_d) = \exp\left\{\jmath\left[-X\sqrt{4k^2 - k_u^2} - k_u Y + \frac{X_1}{4k}\left(\frac{2kv_{xi}}{v_r} - k_u - 2k_d\right)^2\right]\right\} \tag{A.44}$$

Inserting expressions (A.43) and (A.44) into (3.12) gives

$$\exp\left[-\jmath\left(X_1\sqrt{4k^2 - k_u^2} - \frac{X_1}{4k}\left(-k_u - 2k_d\right)^2\right)\right] S(k_u, \omega, k_d) = \exp\left\{\jmath\left[\frac{v_{xi}}{v_r}y_i\sqrt{4k^2 - k_u^2} - k_u(\frac{v_{xi}}{v_r}X_1 + y_i) + \frac{X_1 v_{xi}}{v_r}\left(\frac{kv_{xi}}{v_r} - k_u - 2k_d\right)\right]\right\} \tag{A.45}$$

Appendix B

Approximations for Certain Phase Functions

B.1 Derivation of equation (4.4)

In order to simplify expression (4.1), we introduce the substitution

$$\zeta = b + c \tag{B.1}$$
$$\zeta + d = b - c. \tag{B.2}$$

Square roots in formula (4.1) can then be rewritten into the form

$$\sqrt{\kappa^2 + (b+c)^2} + \sqrt{\kappa^2 + (b-c)^2}.$$

This can be approximated by

$$2\sqrt{\kappa^2 + b^2 + c^2},$$

provided that

$$\kappa^2 + b^2 + c^2 \gg 2b^2c^2 - \kappa^2(b^2 + c^2).$$

Thus, after substituting for b and c, expression (4.1) becomes

$$\begin{aligned} s(k,u,d) \approx \sigma \exp\big[-\jmath 2k \\ \cdot \sqrt{\kappa^2 + (\zeta + d/2)^2 + d^2/4}\big]. \end{aligned} \tag{B.3}$$

Further, assuming that $x^2 \gg (v_x x/v_r)^2 + 2v_x xy$, we can write

$$\begin{aligned} s(k,u,d) \approx \sigma \exp\big[-\jmath 2k \\ \cdot \sqrt{x^2 + (y - u + v_a x)^2 + (y-u)d + d^2/2}\big], \end{aligned} \tag{B.4}$$

where $v_a = v_x/v_r$. Suppose a signal produced by a stationary, unit reflectivity point target located at coordinates $(X_1, 0)$ equals

$$s_0(k,u,d) \approx \exp\left[-\jmath 2k \cdot \sqrt{X_1^2 + u^2 - ud + d^2/2}\right]. \tag{B.5}$$

The compressed signal will then be

$$s_c(k,u,d) = s(k,u,d)s_0(k,u,d)^*, \tag{B.6}$$

where * denotes complex conjugation. To further simplify both expressions (B.4) and (B.5), the so-called Fresnel approximation will be employed

$$\sqrt{x^2+y^2} \approx x + \frac{y^2}{2x}. \tag{B.7}$$

This will yield

$$s(k,u,d) \approx \sigma \exp\left[-2\jmath\, kx - \jmath\, k\frac{(y-u+v_a x)^2 + (y-u)d + d^2/2}{X_1}\right]. \tag{B.8}$$

The same approximation is used to evaluate expression (B.5). Finally, the result is obtained

$$s_c(k,u,d) \approx \sigma \exp\left\{-2\jmath k \cdot \left[x - X_1 + \frac{y}{X_1}\left(\frac{d}{2} - u\right) - uv_a\right] - \jmath\phi\right\}, \tag{B.9}$$

where

$$\phi = k\frac{(y+v_a x)^2}{X_1}. \tag{B.10}$$

Note that ϕ can be split into two parts. One part is constant with u and d and independent of x. This part does not influence positions of targets after focusing and can be neglected on these grounds. The other part is dependent on x, but due to $v_a \ll 1$, it can be also neglected.

B.2 Finding the Fourier transform of function $s_a(u,d)$

Suppose a more general case when σ is a continuous amplitude function instead of a discrete one. Then,

$$s_a(u,d) = \int_{-\infty}^{\infty} \sigma(a) e^{-\jmath\, a(d/2-u)} \mathrm{d}a. \tag{B.11}$$

The Fourier transform $s_a(u, d)$ with respect to u will be [30]

$$\hat{s}_a(k_u, d) = \int_{-\infty}^{\infty} s_a(u, d) e^{-\jmath k_u u} \, \mathrm{d}u, \tag{B.12}$$

$$\begin{aligned} \hat{s}_a(k_u, d) = \int_{-\infty}^{\infty} \sigma(a) \\ \cdot e^{-\jmath ad/2} \mathcal{F}_{(u)} \left\{ e^{\jmath au} \right\} \, \mathrm{d}a, \end{aligned} \tag{B.13}$$

$$\begin{aligned} \hat{s}_a(k_u, d) = 2\pi \int_{-\infty}^{\infty} \sigma(a) \\ \cdot e^{-\jmath ad/2} \delta(a - k_u) \, \mathrm{d}a, \end{aligned} \tag{B.14}$$

$$\hat{s}_a(k_u, d) = 2\pi\sigma(k_u) e^{-\jmath k_u d/2}. \tag{B.15}$$

The Fourier transform of $\hat{s}_a(k_u, d)$ with respect to d will be

$$\begin{aligned} S_a(k_u, k_d) = 2\pi \int_{-\infty}^{\infty} \sigma(k_u) \\ \cdot e^{-\jmath k_u d/2} e^{-\jmath k_d d} \, \mathrm{d}d \end{aligned} \tag{B.16}$$

$$S_a(k_u, k_d) = 4\pi^2 \sigma(k_u) \delta(k_d + k_u/2). \tag{B.17}$$

Since Dirac delta $\delta(x)$ has a value other than zero only at $x = 0$, $S_a(k_u, k_d)$ will exhibit peaks at a line $k_d = -k_u/2$.

The Fourier transform of $\hat{s}_a(k_u, d) \exp(-\jmath \, k_u d/2)$ with respect to d gives

$$\mathcal{F}_{(d)} \left\{ 2\pi\sigma(k_u) \right\} = 4\pi^2 \sigma(k_u) \delta(k_d). \tag{B.18}$$

This function is a line of points located at $(k_u, k_d = 0)$.

Acknowledgements

Very few things are accomplished by a single person only. A PhD thesis should be one of those things. Even though this is true in this case as well, there are a number of people I am very much thankful to for their support and encouragement during this process:

A big credit is due to my promoters, prof.dr.ir Leo P. Ligthart and prof.ir. Peter Hoogeboom. I am grateful for professor Hoogeboom's calm, openness and trust. Under his supervision, I have learned that everyone can win in nearly every situation. Professor Ligthart's good heart and clear vision provided me with guidance and keen word when it was most needed.

I am indebted to Mattern Otten, Jacco de Wit and Wim van Rossum of TNO for their patience with me. I sometimes struggled (and often failed) to produce a correct mix of ambition and tact during our discussions. In spite of that, I have always encountered insight and good advice. For the superb coffee and a sturdy computer, thanks go to my colleagues from the TNO's *aquarium* room.

At TU Delft, prof. Alex Yarovoy and dr. Tim Savelyev granted me access to the GPR setup which I gratefully acknowledge. Pascal Aubry helped me with the instrumentation and GPR data acquisition in his spare time. His helpfulness and thorough knowledge of the equipment was essential to obtaining good results. Dr. Pavel Paclík of PR Sys Design introduced me to the basics of search algorithms, pattern recognition and various matters concerning programming tools and good design.

A very important part of my life in Delft was spent within the Delft International Student Chaplaincy. It was a place of refuge, reflection and a source of long-lasting friendships. Encounters with people such as Fr. Ben Engelbertink and Rev. Waltraut Stroh have had a profound impact on me which will be felt in many years to come.

Lastly, I would like to express my deepest gratitude to Ria Vroolijk, and Edwin and Melle Mollema for putting up with my poor Dutch but, above all, for the most precious experience a foreigner abroad can get: I felt welcome. I felt at home. Thank you for that, I shall never forget you.

Ludvík Lidický

Bibliography

[1] A. Swami, J. Mendel and Ch. Nikias. *Higher-Order Spectral Analysis Toolbox For Use with MATLAB.* United Signals & Systems, Inc., 1993-2001.

[2] P. Angenoorth, L. Chabod, and P. Hoogeboom. The SOSTAR-X program achievements. In *Proceedings EuRAD conference*. EuRAD conference, Oct 2008.

[3] S. Barbarossa. Detection and imaging of moving objects with synthetic aperture radar, part 1. *IEE Proceedings-F*, 139(1), February 1992.

[4] S. Barbarossa and A. Farina. Detection and imaging of moving objects with synthetic aperture radar, part 2. *IEE Proceedings-F*, 139(1), February 1992.

[5] S. Barbarossa and A. Farina. Space-time-frequency processing of synthetic aperture radar. *IEEE transactions on aerospace and electronic systems*, 30(2), April 1994.

[6] I. Bilinskis. *Digital Alias-free Signal Processing.* Wiley, 2007.

[7] V. A. Borovikov. *Uniform Stationary Phase Method.* IEE, 1994.

[8] J. M. B. Dias and P. A. C. Marques. Multiple moving target detection and trajectory estimation using a single SAR sensor. *IEEE transactions on aerospace and electronic systems*, 2003.

[9] R. B. Dingle. *Asymptotic Expansions: Their Derivation and Interpretation*. Academic Press, 1973.

[10] J. Ender and R. Klemm. Airborne MTI via digital filtering. In *IEE Proceedings*, volume 136, February 1989.

[11] J. H. G. Ender. Detectability of slowly moving targets using a multi channel sar with an along-track antenna array. In *SEE/IEE Colloquium on SAR-93*, pages 19–22, 1993.

[12] J. H. G. Ender. Detection and estimation of moving target signals by multi-channel sar. In *Proc. of the EUSAR conference, Koenigswinter, Germany*, pages 411–417, 1996.

[13] A. De Maio et al. KB-GLRT: exploiting knowledge of the clutter ridge in airborne radar. *IEE Proc.-Radar Sonar Navig.*, 152:421–428, 2005.

[14] C. Yang et. al. Matrix-free constructions of circulant and block circulant preconditioners. *Numerical Linear Algebra with Applications*, 11:773–793, 2004.

[15] T. K. Sarkar et al. A deterministic least-squares approach to space-time adaptive processing (STAP). *IEEE Transactions on Antennas and Propagation*, 49:91–103, 2001.

[16] G. Golub and Ch. van Loan. *Matrix computations*. The Johns Hopkins University Press, 3rd edition, 1996.

[17] J. R. Guerci. *Space-Time Adaptive Processing for Radar*. Artech House, 2003.

[18] J. R. Guerci and J. S. Bergin. Principal components, covariance matrix tapers, and the subspace leakage problem. *IEEE Transactions on Aeorspace and Electronic Systems*, 38:152–162, 2002.

[19] A. Haimovich. The Eigencanceler: Adaptive radar by eigenanalysis methods. *IEEE Transactions on Aerospace and Electronic Systems*, 32(2):532–542, Apr 1996.

[20] B. Himed and M. Soumekh. Synthetic aperture radar-moving target indicator processing of multi-channel airborne radar measurement data. *IEE Proc.-Radar Sonar Navig.*, 153:532–543, 2006.

[21] J.J.M. de Wit, W.L. van Rossum and F.M.A. Smits. SAPPHIRE: A novel building mapping radar. In *Proceedings of EuSAR, Rome*, 2009.

[22] H. Kantz and T. Schreiber. *Nonlinear Time Series Analysis*. Cambridge University Press, second edition, 2004.

[23] I. Kirsteins and D. Tufts. Adaptive detection using low rank approximation to a data matrix. *IEEE Transactions on Aeorspace and Electronic Systems*, 30(1), January 1994.

[24] R. Klemm. *Space-Time Adaptive Processing: principles and applications*. IEE, London, 1998.

[25] R. Klemm. Introduction to space-time adaptive processing. *Electronics and communication engineering*, February 1999.

[26] J. Li and P. Stoica. *MIMO Radar Signal Processing.* Wiley, 2009.

[27] P. Lombardo. A joint domain localized processor for SAR target detection. In *Proceedings of EUSAR*, 1998.

[28] W.L. Melvin. A STAP overview. *IEEE Aerospace and Electronic Systems Magazine*, 19:19 – 35, Jan 2004.

[29] C. Moler. Cleve's corner: Professor SVD. *MATLAB Digest Magazine*, Oct 2006.

[30] Paul J. Nahin. *Dr. Euler's fabulous formula : cures many mathematical ills.* Princeton University Press, 2006.

[31] A. Papoulis. *Systems and Transforms with Applications in Optics.* McGraw-Hill, 1968.

[32] F. Roth. *Convolutional Models for Landmine Identification with Ground Penetrating Radar.* PhD thesis, Delft University of Technology, 2005.

[33] C. Santamarina and D. Fratta. *Discrete signals and inverse problems : an introduction for engineers and scientists.* Chichester : Wiley, 2005.

[34] M. I. Skolnik. *Introduction to Radar Systems.* New York: McGraw Hill, 1980.

[35] M. Soumekh. *Fourier Array Imaging.* Prentice Hall, 1994.

[36] M. Soumekh. Phased array imaging of moving targets with randomized beam steering and area spotlighting. *IEEE Transactions on Image Processing*, 6:736 – 749, May 1997.

[37] M. Soumekh. *Synthetic Aperture Radar Signal Processing with MATLAB Algorithms.* Wiley-Interscience, 1999.

[38] J. Stamnes. Waves, rays, and the method of stationary phase. *OPTICS EXPRESS*, 10(16), August 2002.

[39] J. V. Stone. *Independent Component Analysis, a Tutorial Introduction*. MTI Press, 2004.

[40] K. Tomiyasu. Tutorial Review of Synthetic-Aperture Radar (SAR) with Applications to Imaging of the Ocean Surface. *Proceedings of the IEEE*, 66(5):563–583, May 1978.

[41] P. van Genderen et al. Radar development in the Netherlands: 100 years since Hülsmeyer. EuMW Conference booklet, Amsterdam, 2004.

[42] W. H. Press, S. A. Teukolsky, W. T. Vetterling and B. P. Flannery. *Numerical Recipes in C.* Cambridge University Press, second edition, 1992.

[43] Wikipedia. Battle of cascina. http://en.wikipedia.org/wiki/ Battle_of_Cascina_(Michelangelo), retrieved in, August 2009.

[44] Wikipedia. Optics. http://en.wikipedia.org/wiki/Optics, retrieved in, August 2009.

[45] H. Yang and M. Soumekh. Blind-velocity sar/isar imaging of a moving target. *IEEE Transactions on Image Processing*, 2(1), January 1993.

[46] Z. Yang and M. Soumekh. Adaptive along-track multi-channel SAR interferometry for moving target detection and tracking. In *Radar Conference, 2005 IEEE International*, pages 337–342, 9-12 May 2005.